Electron Energy-Loss Spectroscopy: Analytical Theory and Numerical Simulations of Individual Nanoparticles and Nanostructures

Steven C. Quillin

A dissertation
submitted in partial fulfillment of the
requirements for the degree of

Doctor of Philosophy

University of Washington

2018

Reading Committee:

David J. Masiello, Chair

David S. Ginger

Joshua C. Vaughan

Program Authorized to Offer Degree:
Chemistry

University of Washington

Abstract

Electron Energy-Loss Spectroscopy: Analytical Theory and Numerical Simulations of Individual Nanoparticles and Nanostructures

Steven C. Quillin

Chair of the Supervisory Committee:
Associate Professor David J. Masiello
Chemistry

The field of nanotechnology has experienced rapid growth over the past three decades which can largely be attributed to advances in technologies and experimental techniques. One technology in particular, the electron microscope, has been instrumental in nanoscale exploration allowing one to avoid ensemble measurements and investigate single nanoparticles and individual nanostructures. The ability to probe the fundamental behavior of such systems is paramount to the design of nanoscale devices.

This dissertation focuses on spectroscopic methods mediated by the electron microscope, mainly electron energy-loss spectroscopy (EELS), and the capacity of such techniques to explore nanoscale behavior in aggregates of plasmon supporting metal nanoparticles (MNPs) and semiconducting nanoparticles. We present a theoretical framework to describe the EELS experiment in general, as well as for the MNPs in the quasistatic limit that lends itself to the simple treatment of MNP dimers and aggregates by mapping MNPs onto harmonic oscillators.

The spatial dependence of EELS is explored for MNP aggregates, focusing on the ability of the electron to unevenly force a nanostructure. An analytic treatment is presented to describe Fano resonances in MNP dimers driven by the electron beam where the evanescent nature of the electron's electric field is exploited to investigate a broader class of Fano resonances than those available in optical spectroscopies. We further explored the spatial dependence

of EELS to image hybridized normal modes of MNP nanostructures. Analysis of nodal structure in EEL maps is shown to provide a rubric for determining the relative phase of charge oscillations within a nanostructure.

This rubric is further applied to plasmon oligomer dimers effectively mapping magnetic modes using numerical simulations and experimental measurements. We further observe signatures of magnetic field localization in symmetry broken oligomer dimers. This interference effect is shown to occur at two distinct energies that controls the location of magnetic field by the energy of incident far-field radiation.

We move away from the oscillator model when considering phenomena that occur in semiconducting nanoparticles that hold a high index of refraction. Such systems are experimentally shown to exhibit band gap peaks which do no correspond to electron excitations within the material. Through numerical simulations and an EELS Mie theory analysis these unusual peaks are shown to correspond to cavity modes of the nanoparticle and are analogous to geometric scattering.

TABLE OF CONTENTS

LIST OF FIGURES

GLOSSARY

BE: Bright Electric

BM: Bright Magnetic

BEM: Boundary Element Method

CL: Cathodoluminescence

DDA: Discrete Dipole Approximation

DE: Dark Electric

DM: Dark Magnetic

E-DDA: Electron-Driven Discrete Dipole Approximation

EEL: Electron Energy-Loss

EELS: Electron Energy-Loss Spectroscopy

FIB: Focused-Ion-Beam Milling

FWHM: Full Width Half Maximum

HAADF: High-Angle Annular Dark-Field

LSPR: Localized Surface Plasmon Resonance

MNP: Metal Nanoparticle

MNPBEM: Metal Nanoparticle Boundary Element Method

STEM: Scanning Transmission Electron Microscope

TEM: Transmission Electron Microscope

WGM: Whispering Gallery Modes

ZA: Zone Axis

ZLP: Zero-Loss Peak

ACKNOWLEDGMENTS

First and foremost, I would like to thank my advisor Professor David Masiello. All of the work contained in this text was made possible by David, starting with his belief in my ability as a scientist. David invited me into his group early in my graduate career, providing leadership and guidance in a field in which I knew little. David did not dwell on my shortcomings, but assisted me in overcoming them and further challenging me to better myself. I can not thank him enough for all that he has done and provided during my graduate career.

In addition to David, I must thank his research group with whom I have had the pleasure of collaborating: Dr. Charles Cherqui, Dr. Nicholas Bigelow, Dr. Niket Thakkar, Nicholas Montoni, Jake Busche, Harrison Goldwyn, Claire West, Elliot Beutler, and Kevin Smith. Charles acted as an additional advisor and has had a significant impact on my scientific development, providing guidance, challenging me intellectually, and debating nearly daily. I am indebted to him for all of the help he has provided over the years and can not thank him enough for everything that he has done.

It would be foolish to not thank the experimental collaborator with whom I have worked over the years. Professor Jon Camden and Dr. Guoliang Li at the University of Notre Dame have been vital to many of the EELS experiments contained in this text. Professor Philip Rack and Dr. Yueying Wu from the University of Tennessee in Knoxville have been phenomenal to work with, fabricating nanostructures. Professor Peter Crozier and Dr. Qianlang Liu at Arizona State University have been a pleasure to collaborate with, covering topics that were initially out of my wheelhouse and pushing me to gain a more thorough understanding of nanosystems. I would also like to thank collaborators whose work did not appear in this text,

mainly Professor Randall Goldsmith and his research group at the University of Wisconsin in Madison.

My committee, Dr. David Ginger and Dr. Joshua Vaughan, and my Graduate School Representative, Dr. Peter Pauzauskie, have provided useful guidance and feedback for my work and for that I thank them.

I would like to thank my family for their continual support in all of my endeavors in life. From an early age my parents, Rebecca and Timothy Quillin, encouraged my curiosity in the natural world and have been a constant of support through all aspects of my life. I thank my brother, Timothy Quillin Jr., for always being there for me when I needed him.

Finally, I would like to thank my girlfriend, Heidi Nelson, who has managed to tolerate all of my nonsense the last four and a half years of graduate school. It takes a truly special person to commit to a relationship with a PhD student, particularly when working towards their own PhD. I would not have been able to do it without her support.

DEDICATION

to my parents

Chapter 1
INTRODUCTION

1.1 A Brief History of Optics

Historically the understanding of light has been vital to the understanding of the physical world. The field of optics had its advent with the development of lenses in ancient Egypt and Mesopotamia, showing the desire to manipulate light using polished crystal [84]. The quest to control light continued in ancient Greece and Rome where spherical lenses of glass globes filled with water were used for magnification [84] and philosophy surrounding the nature of light and vision started to develop. A critical step in the field of optics emerged in ancient Greece by Euclid when he connected geometry with optics laying the groundwork for the aptly named geometrical optics including reflection and refraction of rays [37].

While Euclid took the ray like nature of light to be an axiom, scholars in the Arabic world in the ninth century, in particular Ishak Al-Kindi, studied shadows cast by opaque materials to to prove such behavior [37]. Al-Kindi additionally theorized that all objects emits rays of light contradicting many early beliefs in which rays of light originated in the eyes and emitted outward [93]. Nearly a century later the study of parabolic and ellipsoidal mirrors and a variety of lenses by Ibn Sahl lead to the development of a mathematical theory for refraction and the focusing of light. Sahl's work resulted in a similar expression to Snell's law nearly seven centuries prior to Willebrord Snellius [127]. Such an understanding of light provided a path forward to using light to observe phenomena on smaller length scales.

The earliest appearance of a microscope using objective lenses was in seventeenth century Europe [109]. The optical microscope made great strides in discovery allowing once unobservable systems to be studied. Microscopes remained a novelty late into the century until Robert

Hooke's Micrographia, which contained illustrations of life on smaller scales, inspired progress in the field of microscopy further developing microscope technologies [77]. The resolving power of light increased with the passage of time allowing for smaller and smaller systems to be examined providing a more thorough understanding of the physical world.

In a purely ray or corpscicle theory of light one would expect to be capable of infinitely resolving objects on small length scales. However, this is not the case. In 1678 Christiaan Huygens proposed the wave nature of light in his work titled *Traité de la Lumiere*. The wave characteristics of light provided a limit to the resolving power in optical microscopes, which is tied to the wavelength of light and properties of the optics of the device. This limit, known as the diffraction limit, was first mathematically described by Ernst Abbe in 1873 [95]

$$r = \frac{\lambda}{2n \sin \theta} \tag{1.1}$$

where the r is the radius of the smallest spot that can be resolved, λ is the wavelength of the light passing through the microscope lens, n is the refractive index of the lens, and θ is the aperture angle. This provided a hard limit on systems that could be observed in a conventional optical microscope using visible light. While this limit is small in comparison to cells it was large relative to the size of molecules, including biological macro-molecules such as proteins.

The inability to resolve systems below the diffraction limit proved to be an obstacle in the scientific world. Attempts to circumvent the diffraction limit were formulated and one method utilizes swift electrons instead of light for the purpose of microscopy. This was expanded from microscopy to spectroscopy and is the focus of this text and will be described in detail in the next chapter.

1.2 Materials on the Nanoscale

Nanoscale materials have been used for millennia in works of art despite the inability to directly observe and study these materials on their length scales. From stained glass [33] to glittering pottery [128], nanoparticles were used to obtain rich colors from the scattering of

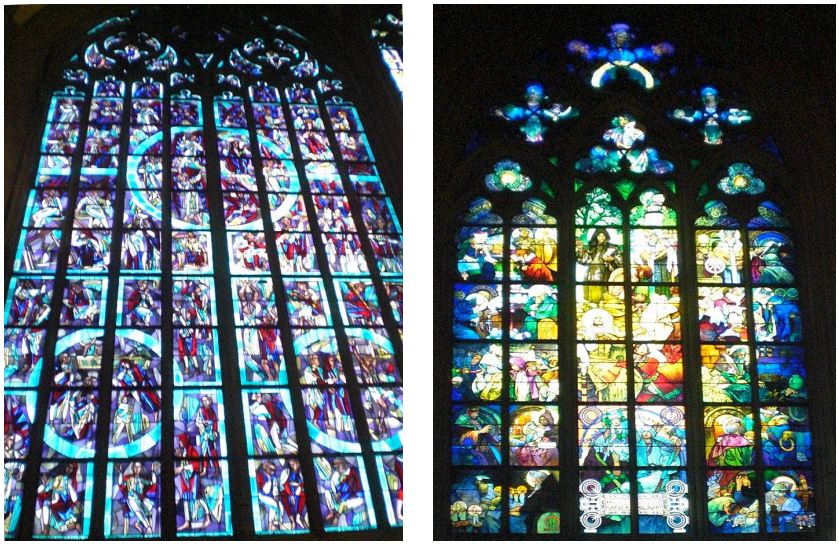

Figure 1.1: Examples of stained glass art from the Aachen cathedral (left) in Aachen, Germany and St. Vitus Cathedral (right) in Prague, Czech Republic. The vibrant colors given off by the illuminated glass is attributed to the presence of nanoparticles in the glass matrix. Photo Credit: Steven C. Quillin

light. The use of nanoparticles in art relied on empirical knowledge of the ensemble properties of nanoparticles without knowledge of the existence of such particles. Properties of the individual nanoparticle were unknown during this time and were only recently capable of being studied due to the development of new technologies and experimental techniques.

This text explores properties of single nanoparticles and individual aggregates of nanoparticles using electron energy-loss spectroscopy (EELS). Later chapters provide a theoretical framework describing the EELS experiment providing insight in the behavior of these systems. Nanoparticles in this text can be divided into two groups, metals and non-metals, each holding very different optical properties.

1.2.1 Metal Nanoparticles

When a metal nanoparticle (MNP) is exposed to an electric field, the conduction band electrons move in response in an attempt to screen the incident field. This displacement of charge inherits a time dependence when exposed to an oscillatory field such as that provided

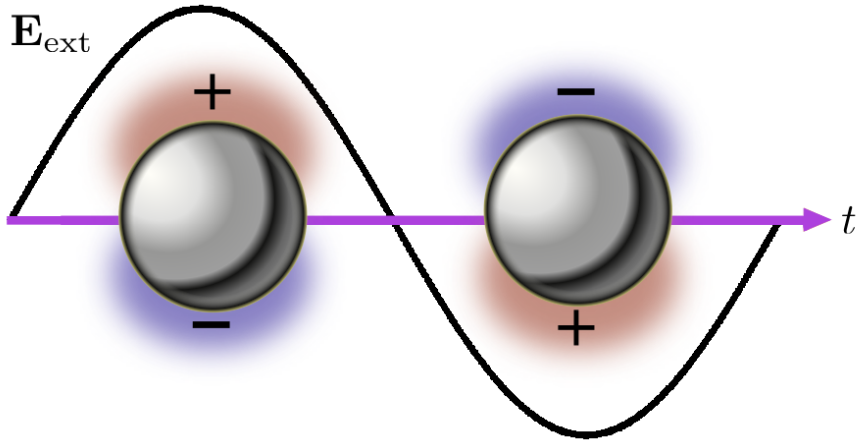

Figure 1.2: When exposed to an oscillating electric field, such as from light, the conduction band electrons inherit oscillatory behavior in the attempt to screen the external electric field. When the oscillation of the electrons in the material is resonant with the incident field, the oscillation is known as a plasmon resonance.

by light. This character is depicted in Figure 1.2. When conditions of the MNP (i.e. material, morphology, environment) are such that the conduction band electrons oscillate resonantly with the applied field, the phenomenon is known as a localized surface plasmon (LSP).

The field of plasmonics has its roots in the study of thin metal films interacting with swift electrons. The results from initial studies [133, 87] were not well explained, and it was Bohm and Pines that developed a theoretical understanding of collective plasma oscillations of conduction band electrons in bulk metals [20, 120, 21]. This was later developed by Ritchie in 1957 [129] into a theory to predict oscillations of surface charge at metal boundaries. This was experimentally verified shortly thereafter with electron energy-loss studies [123]. Experiments extended to light as an excitation source, in which the evanescent field of total internally reflected light in glass prisms was used to excite surface charge oscillations in thin metal films [116, 81]

LSPs have been shown to exhibit sub-diffraction-limited control of light [14, 49, 117], charge [26, 146], and heat [10, 11, 12, 52]. While early experimental work in the field of plasmonics was limited to rather simple systems, advances in synthesis and manufacturing

techniques has led to a high degree of control on particle morphologies and aggregation schemes opening a myriad of possible structures exhibiting exotic behavior. Due to the robust nature and versatility in nanoscale control, plasmons continue to be a promising field of study with applications in a number of fields, including photovoltaics [94, 141], catalysis [90, 108], chemical sensing [44, 71, 78, 111], and medicine [23, 50, 65].

1.2.2 Semiconducting and Insulating Nanoparticles

In contrast to metals, semiconducting and insulating materials have a vacant conduction band and a fully filled valence band. Excitations of the valence band electrons are limited to interband excitations from the valence to conduction band. The absence of electronic states between bands provides a minimum amount of energy required for excitations, known as the band gap. The distinction between semiconductors and insulators arises from the magnitude of the band gap. When the band gap is small, where thermal excitations can result in conductivity at temperatures below the material's melting point, the material is classified as a semiconductor. When the band gap is large such that the material melts before thermal excitations result in an observable conductivity, the material is classified as an insulator. [8]

When an incident electric field is applied to a non-metal with appropriate energy and momentum to excite an electron into the conduction band a hole remains in the valence band creating what is known as an electron-hole pair. The generation and recombination of electron-hole pairs is vital to the function of various optoelectronic devices such as light emitting diodes, photodiodes, and laser diodes. The generation of electron-hole pairs, and their subsequent recombination, can be observed using spectroscopy where a signal is detected at energies above the band gap of the material. As there is an absence of electronic states in the band gap, no spectroscopic character is observed in the band gap of bulk materials.

1.3 Outline

1.3.1 Publications

The author's peer reviewed work in the Masiello group includes five published papers and five more in preparation. An additional publication precedes the author's graduate school work and is not included here. Steven C Quillin's publications in the Masiello group are:

1. ***Imaging Plasmon Hybridization in Metal Nanoparticle Aggregates with Electron Energy-Loss Spectroscopy***
   S.C. Quillin, C. Cherqui, N.P. Montoni, G. Li, J.P. Camden, D.J. Masiello
   Journal of Physical Chemistry C **120**, 20852 (2016).

2. ***STEM/EELS Imaging of Magnetic Hybridization in Symmetric and Symmetry-Broken Plasmon Oligomer Dimers and All-Magnetic Fano Interference***
   C. Cherqui, Y. Wu*, G. Li*, S. C. Quillin*, J. A. Busche, N. Thakkar, C. A. West, N. P. Montoni, P. D. Rack*, J. P. Camden*, and D. J. Masiello
   Nano Letters **16**, 6668 (2016).

3. *Optical Microresonators as Single-Particle Absorption spectrometers*
   K. D. Heylman, N. Thakkar, E. H. Horak, S. C. Quillin, C. Cherqui, K. A. Knapper, D. J. Masiello, and R. H. Goldsmith
   Nature Photonics **10**, 788 (2016).

4. *Noninvasive Cathodoluminescence-Activated Nanoimaging of Dynamic Processes in Liquids*
   C. G. Bischak, R. B. Wai, C. Cherqui, J. A. Busche, S. C. Quillin, C. L. Hetherington, Z. Wang, C. D. Aiello, D. G. Schlom, S. Aloni, D. F. Ogletree, D. J. Masiello, and N. S. Ginsberg
   ACS Nano **11**, 10583 (2017).

5. *Sculpting Fano Resonances to Control Photonic-Plasmonic Hybridization*
   N. Thakkar, M. Rea, K. C. Smith, K. D. Heylman, S. C. Quillin, K. A. Knapper, E. H. Horak, D. J. Masiello, and R. H. Goldsmith
   Nano Letters **17**, 6927 (2017).
6. *Mulipolar Nanocube Plasmon Mode-Mixing in Finite Substrates*
   C. Cherqui, G. Li, J.A. Busche, S.C. Quillin, J.P. Camden, D.J. Masiello
   Journal of Physical Chemistry C **9**, 504 (2018).
7. ***Cavity Modes of Oxide Nanoparticles Probed by Monochromated Electron Energy-Loss Spectroscopy***
   Q. Liu, S.C. Quillin, D.J. Masiello, P.A. Crozier
   This work is currently under review (2018).
8. ***Fano Interferences Observed by Electron Energy-Loss Spectroscopy and Cathodoluminescence***
   S.C. Quillin, Y. Wu, J. Carlos, J.P. Camden, D.J. Masiello
   This work is currently in progress (2018).
9. *Hamiltonian Formalism to Describe Localized Plasmon Resonance Coupling in Asymmetric Environments*
   J.A. Busche, C. Cherqui, S.C. Quillin, D.J. Masiello
   This work is currently in progress (2018).
10. *Tunable Spectral Ordering of Magnetic Plasmons*
    N.P Montoni, S.C. Quillin, C. Cherqui, D.J. Masiello
    This work is currently in progress (2018).

* These authors contributed equally to this work

This dissertation contains two of the six published papers, one paper that is currently under review, and one work in progress indicated with bold titles. The papers included in this text are works in which Steven C. Quillin has contributed significantly. Chapters 4 and 5 are works already published and Chapter 6 is currently under review.

1.3.2 Form of Dissertation

This dissertation provides insight on electron spectroscopies, mainly EELS, performed on nanoparticle systems. First, a theoretical framework for EELS is provided and then applied to various nanoscale systems. This work aims to provide the tools needed to approach and understand larger systems when interrogated with relativistic electrons.

Chapter 2 provides a general theory describing the electromagnetic interaction of a swift electron with matter. The underlying interaction is quantum mechanical (probabilistic) in nature and can be treated statistically. This allows for the solving for a distribution function describing EELS by relating the first moment of this distribution function to the average mechanical work on the passing electron. This expression is dependent on the treatment of matter, requiring a loss of generality, and is expressed in convenient forms of MNPs in the quasistatic limit and arbitrary particles when accounting for retardation effects. In addition to an analytic theory, numerical methods for calculating EELS probabilities that are used in later chapters are described. The theoretical and numerical framework provided in this chapter appears in chapters 3-6.

In chapter 3, we use the general theory provided in chapter 2 to describe coupled MNP dimer systems that exhibit Fano interferences. This system contains plasmonic modes that are "bright" playing the role of the continuum and modes that are "dark" playing the role of discrete states from Ugo Fano's original work on helium. The Fano character of such systems is observed in EELS and Cathodoluminescence, the theory for which is provided in chapter 3. The analytic theory for Fano dimers is shown to qualitatively agree with numerical simulations of "lollipop" systems that are far outside of the quasistaic limit. This chapter aims to provide the backbone of a future manuscript.

In chapter 4, we transform plasmonic dimers into normal mode coordinates and observe how the relativistic electron forces the normal modes of a system. By altering the impact parameter of the electron we are able to image the hybridized modes. We demonstrate that the EEL probability is directly tied to the ability to force a normal mode and in that event

that a mode cannot be forced the spatial signature provides information to the relative phase of dipole moments within the system. By analyzing the nodal structure of EEL maps we are able to image and identify normal modes of MNP aggregates. EELS data collected from our experimental collaborators verify the theory and simulations for this mechanism. The material for this chapter comes from Ref. [126]

In chapter 5, the intuition gained from chapter 4 is applied to MNP oligomer dimer systems to image magnetic normal modes. The oligomer systems in this chapter are altered from those previously studied, replacing spherical nanoparticles arranged in fused ring configurations with elongated rod-like nanoparticles to reduce the number of normal modes energetically near the magnetic modes of the system. In addition to isolating the magnetic modes of such oligomer systems, the symmetry of the dimer was broken leading to Fano-like interferences between two magnetic modes localizing the magnetic field to each ring at a separate energy. The structures were lithographically created and measured using EELS by our experimental collaborators. The material for this chapter comes from Ref. [31]

In chapter 6, we consider behavior that occurs in EELS experiments on high dielectric semiconducting nanoparticles. The ability of EELS to study localized properties of a system allows for its use in studying ligands, surface layers, and other properties that may introduce a non-zero density of states in the band gap of a semiconductor nanoparticle. Experimental results in this chapter demonstrate the effectiveness of this technique for MgO, however, the EEL spectra for TiO_2 and CeO_2 exhibit unusual character in the form of band gap peaks. Analysis of this phenomenon requires retardation effects to be included in the treatment of EELS giving rise to cavity modes for high dielectric nanoparticles. Comparison of Mie coefficients for EELS and optical scattering for real valued dielectrics, which is true for energies in the material band gap, shows that both scattering and EELS hold the same resonance structure. The cavity modes observed in the EEL spectra are analogous to geometric scattering resonance on nanoparticles forming standing waves in the dielectric cavity. The ability of EELS to observe these resonances proves to be a precautionary tale for researchers investigating high index materials. The material for this chapter is a manuscript

in preparation.

Chapter 2

ELECTRON ENERGY-LOSS SPECTROSCOPY: A GENERAL THEORY

The limitation of the resolving power of light, known as the diffraction limit, constrains the length scale of systems that can be observed with conventional optical microscopes as the resolving power is tied to the wavelength of illuminating radiation. One method of bypassing this problem is through the use of shorter wavelengths of light, however this requires expensive optics as typical glasses have band gaps in the UV range. Regardless, these efforts were carried forward by researchers allowing the resolving power to be doubled in comparison to visible light [132]. In parallel to using UV radiation, observations on cathode rays and their behavior in magnetic fields led to the development of measuring devices for electrons. By the 1920's research on this subject culminated in applying the lens maker's equation to electrons. This rapidly developed into the first functional electron microscope at the Technische Universität Berlin [132].

It was not long until a technique involving the measurements of electrons was developed by James Hillier and R.F. Baker in 1944 [60] to perform spectroscopy using an electron microscope. While the technique was proposed during this time it was not widely used for the next half-century until technological advancements allowed electron energy-loss spectroscopy (EELS) to become a more common spectroscopic method. In the proposed EELS technique the change in velocity (kinetic energy) of transmitted electrons was associated with the excitation of electronic states in atoms, laying the groundwork for the electron microscope being used as a probe of electronic states at the nanoscale via electromagnetic interactions. Before delving too deep into how the electron interacts with matter, it is informative to consider the behavior of the relativistic electron.

2.1 Relativistic Electrons

The electron, like all point charges, holds a spherically symmetric potential while at rest. Due to the charge having negative character the electric field of the electron points radially inward towards the electron. The electric field at a location in space, $\mathbf{r}$, due to an electron located at $\mathbf{r}'$ is represented as

$$\mathbf{E}(\mathbf{r}, \mathbf{r}') = -e\frac{\mathbf{r} - \mathbf{r}'}{|\mathbf{r} - \mathbf{r}'|^3}. \tag{2.1}$$

While an electron is at rest there is no time dependence to the nature of the electric field and the field is considered to be static. An electron at rest is useless for the purpose of spectroscopy due to this fact. This changes when the electron moves out of the rest frame by adding a velocity component to the electron's position. For simplicity the moving electron will be described using cylindrical coordinates, where the direction of electron motion is chosen to be along the z-axis, and the radial coordinate, $\mathbf{R}$, will be defined as the distance from the electron in the plane perpendicular to the electron propagation. The electron coordinate will be defined by its velocity, v, multiplied by time, t. This results in an electric field for the moving electron

$$\mathbf{E}(\mathbf{r}, t) = -e\frac{\mathbf{R} + \mathbf{z} - \mathbf{v}t}{\left[R^2 + (z - vt)^2\right]^{3/2}}. \tag{2.2}$$

This expression for the electric field of a moving electron could be used to describe the EELS experiment, however, it would only be accurate at low electron velocities unlike the electrons produced in a transmission electron microscope (TEM). In a TEM electrons are accelerated to velocities near the speed of light requiring treatment with the special theory of relativity. As the velocity of the electron increases a contraction of the electric field occurs in the direction of electron propagation. This effect breaks the spherical symmetry of the electric field "pancaking" the electric field to become more confined into the plane perpendicular to electron motion. This contraction is depicted in figure 2.1.

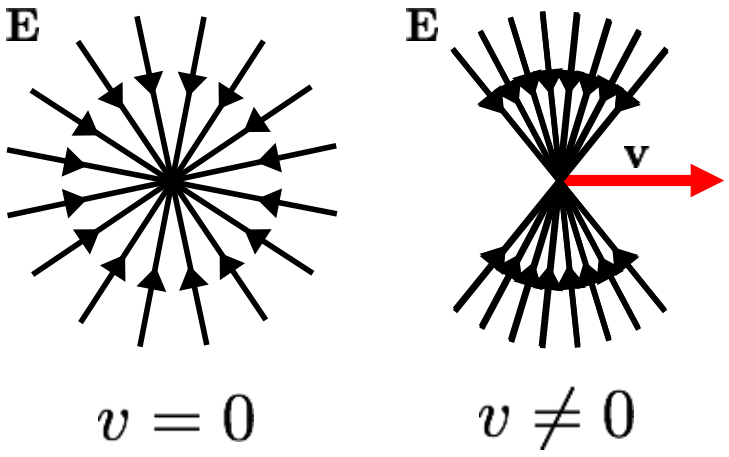

Figure 2.1: Cartoon depicting electric field contraction with increasing electron velocity. As the velocity of the electron approaches the speed of light, the electric field of the electron becomes confined to the plane perpendicular to electron motion.

All of the effects of special relativity can be included by performing a Lorentz transform and describing the electron in a boosted reference frame. The resulting electric field is

$$\mathbf{E}(\mathbf{r},t) = -e\frac{\mathbf{R}+\mathbf{z}-\mathbf{v}t}{\gamma_L^2\left[(R/\gamma_L)^2+(z-vt)^2\right]^{3/2}} \tag{2.3}$$

where $\gamma_L = [1-(v/c)^2]^{-1/2}$ is the Lorentz contraction factor.

The electric field in the time domain provides intuition to the overall character of the electric field, however, for the purpose of spectroscopy the electric field is more useful when expressed in terms of Fourier components. In this picture the electric field of the electron can be observed for each frequency separately. This allows for a more direct relationship between the incident electric field to the response of the material with which the electron interacts. Fourier transforming Eq. 2.3 yields

$$\mathbf{E}(\mathbf{r},\omega) = \frac{2e\omega}{v^2\gamma_L^2}\left[iK_0\left(\frac{\omega R}{v\gamma_L}\right)\hat{\mathbf{z}} - \gamma_L K_1\left(\frac{\omega R}{v\gamma_L}\right)\hat{\mathbf{R}}\right]e^{i\omega z/v} \tag{2.4}$$

where K_0 and K_1 are modified Bessel functions of the second kind. The strength of the electric field decays as a function of distance from the electron, giving the electric field evanescent character. Interestingly, the electric field decays as frequency increases, however, the decay

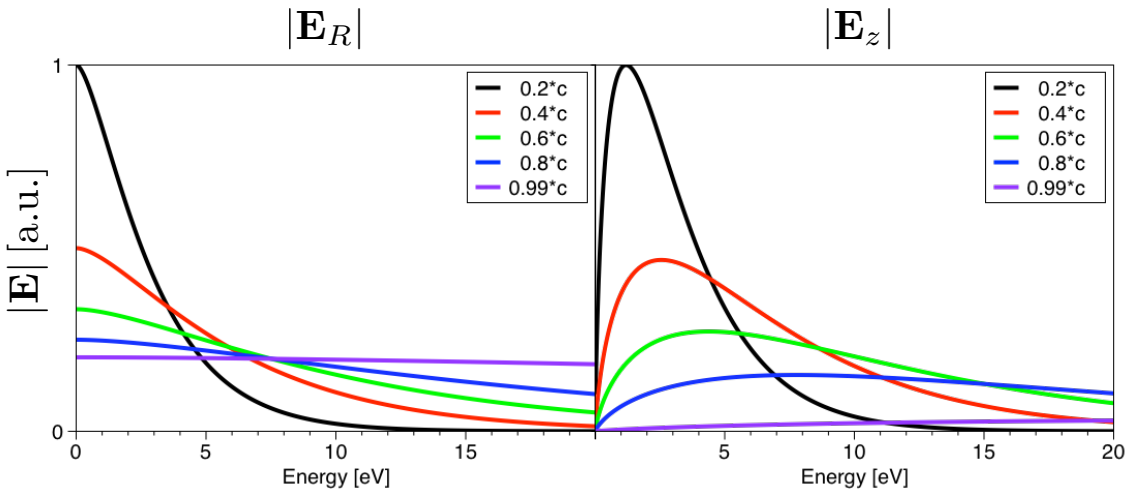

Figure 2.2: The magnitude of the electric field at a point 10 nm from the electron in the plane perpendicular to the electron trajectory as a function of energy for different electron velocities. The radial component of the electric field (left) approaches white light as the velocity approaches the speed of light. The electric field parallel to electron trajectory decreases as the velocity of the electron approaches the speed of light.

is also dependent on the velocity of the electron. This dependence results in a frequency distribution of the electric field that is a function of the electron velocity.

A more thorough investigation to the velocity dependence of the frequency distribution of the electron's electric field is explored in figure 2.2. Here the magnitude of the electric field is shown as a function of frequency for varying velocities. A constant position was selected 10 nm away from the electron in the plane perpendicular to electron motion. The radial component of the field is shown separately from the component parallel to electron motion. Both components of the electric field bias towards lower frequencies when the electron has a low velocity, approaching the static field of the electron at rest. At higher velocities this biasing diminishes resulting in a uniform frequency distribution (approaching white light) for the radial component and vanishing for the component parallel to electron motion. This behavior is consistent with effects due to special relativity and the electric field in the time domain. This distribution of electric field frequencies will manifest in the EEL spectra resulting in a biasing of the relative height of modes interrogated.

2.2 Theoretical Description of Matter

The description of EELS outlined in this dissertation employs a classical, macroscopic treatment of nanoparticles and their response to external fields. A macroscopic description of nanoparticles may sound like an oxymoron, however, the term macroscopic pertains to the form of Maxwell's equations used to describe such a system. Macroscopic fields are defined in terms of averages of time and length scales that are large in comparison to atomic length scales but small in comparison to usual macroscopic intervals [137]. A nanoparticle in a macroscopic sense is defined by a closed boundary where on one side the behavior of macroscopic electromagnetic fields is dictated by the nanoparticle's dielectric function. The dielectric function itself can be considered an average of the microscopic properties of the bulk material which comprises the nanoparticle. External to the nanoparticle boundary, macroscopic electromagnetic fields behave according to the nature of the dielectric function of the environment.

Our treatment of matter will fall into two regimes that either neglect or include effects due to retardation. Effects due to retardation will be neglected for systems of metal nanoparticles (MNPs) as retardation is not needed to observed the physic of interest in these systems. For systems of semiconducting and insulating nanoparticles, the phenomena of interest arise due to retardation and therefore requires a full treatment of matter.

2.2.1 Quasistatic Treatment of Matter

When information is taken to propagate instantaneously it is known as the quasistatic approximation. In the quasistatic limit, effects due to retardation are neglected and Gauss's law in frequency space contains all information about the response of nanoparticles. We solve for the general response of a spherical nanoparticle using a Green's function approach which can be found in [137] and outlined in Appendix A,

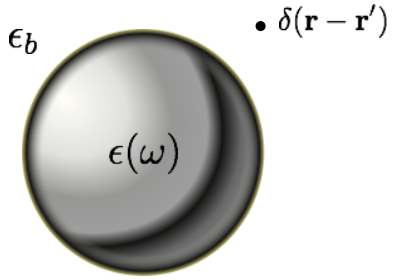

Figure 2.3: Cartoon depicting a spherical dielectric boundary with an external delta function source.

$$\begin{aligned} r > a: \quad -\epsilon_b \nabla^2 G(\mathbf{r},\mathbf{r}';\omega) &= 4\pi\delta(\mathbf{r}-\mathbf{r}') \\ r < a: -\epsilon(\omega)\nabla^2 G(\mathbf{r},\mathbf{r}';\omega) &= 0 \end{aligned} \tag{2.5}$$

where a is the radius of the sphere and the Green's function, $G(\mathbf{r},\mathbf{r}';\omega)$, is the fundamental solution to the Poisson equation with an external charge distribution. A cartoon representing this treatment is provided in figure 2.3. The boundary conditions for the Green's function follow the boundary conditions of the electrostatic potential

At the surface ($r = a$)

1) G is continuous

2) $\left[-\epsilon_b \frac{\partial}{\partial r} G(\mathbf{r},\mathbf{r}';\omega)\right]_{r=a+} = \left[-\epsilon(\omega)\frac{\partial}{\partial r} G(\mathbf{r},\mathbf{r}';\omega)\right]_{r=a-}$

At the point charge ($r = r'$)

1) G is continuous

2) $\left[-\epsilon_b r^2 \frac{\partial}{\partial r} G(\mathbf{r},\mathbf{r}';\omega)\right]_{r=r'-}^{r=r'+} = 4\pi \sum_{\ell=0}^{\infty}\sum_{m=-\ell}^{\ell} Y_{\ell m}(\theta,\phi) Y^*_{\ell m}(\theta',\phi')$.

which results in an external Green's function

$$G_{\text{ext}}(\mathbf{r},\mathbf{r}';\omega) = \frac{1}{\epsilon_b\,|\mathbf{r}-\mathbf{r}'|} - \frac{1}{\epsilon_b}\sum_{\ell=0}^{\infty}\sum_{m=-\ell}^{\ell} \frac{4\pi}{2\ell+1}\frac{\ell(\epsilon(\omega)-\epsilon_b)}{\ell(\epsilon(\omega)+\epsilon_b)+\epsilon_b}\frac{a^{2\ell+1}}{r^{\ell+1}r'^{\ell+1}} Y_{\ell m}(\theta,\phi) Y^*_{\ell m}(\theta',\phi'). \tag{2.6}$$

The first term of this expression corresponds to the free space Green's function and the second term the induced Green's function. The induced Green's function is the kernel for the

potential attributed to the polarization of the nanoparticle and can be used to determine the force acting on the passing electron

$$\mathbf{F}(\mathbf{r},\omega) = -e^2\nabla\left[\frac{1}{\epsilon_b}\sum_{\ell=0}^{\infty}\sum_{m=-\ell}^{\ell}\frac{4\pi}{2\ell+1}\frac{\ell(\epsilon(\omega)-\epsilon_b)}{\ell(\epsilon(\omega)+\epsilon_b)+\epsilon_b}\frac{a^{2\ell+1}}{r^{\ell+1}r'^{\ell+1}}Y_{\ell m}(\theta,\phi)Y^*_{\ell m}(\theta',\phi')\right] \tag{2.7}$$

While carrying forward with this approach to describe EELS is valid it is not the most convenient treatment for the systems under consideration in later chapters.

An alternative approach can be used for MNPs where the dynamics of the nanoparticle coordinate is mapped onto a harmonic oscillator. MNPs are of great interest for nanoscale applications due to their ability to support collective surface resonances known as localized surface plasmon resonances (LSPRs), which hold the ability to induce anomalously large, nano-localized electric fields. This mapping is rigorously performed by considering the surface response function contained in the induced Green's function

$$\tilde{g}_\ell(\omega) = \frac{1}{\epsilon_b}\frac{\ell(\epsilon(\omega)-\epsilon_b)}{\ell(\epsilon(\omega)+\epsilon_b)\ +\epsilon_b} \tag{2.8}$$

which is trivially related to the polarizability of the nanoparticle. An explicit form of the dielectric function can be inserted into this expression and inverse Fourier transformed into time space. The dielectric response of metals is well described with the Drude model (discussed in more detail in Appendix B). The Drude model has the form

$$\epsilon(\omega) = \epsilon_\infty - \frac{\omega_p^2}{\omega^2 + i\gamma\omega} \tag{2.9}$$

where ϵ_∞ accounts for core excitations, ω_p is the plasma frequency, and γ is the damping coefficient for friction. This results in

$$\begin{aligned}\tilde{g}_\ell(t-t') =& \frac{2\ell+1}{\ell(\epsilon_\infty+\epsilon_b)+\epsilon_b}\frac{\omega_\ell^2}{\sqrt{\omega_\ell^2-\gamma^2/4}}\sin\left[\sqrt{\omega_\ell^2-\gamma^2/4}\ (t-t')\right]e^{-\gamma(t-t')} \\ =& \frac{2\ell+1}{\ell(\epsilon_\infty+\epsilon_b)+\epsilon_b}\omega_\ell^2 g_{HO}(t-t').\end{aligned} \tag{2.10}$$

Here the time dependence of the MNP coordinate is shown to explicitly contain the dynamics of a harmonic oscillator. The mass of the harmonic oscillator is determined through further considering the nanoparticle's generalized coordinate

$$\mathbf{x}(t) = \frac{V\omega_\ell^2}{4\pi e^2}\frac{2\ell+1}{\ell(\epsilon_\infty+\epsilon_b)+\epsilon_b}\int_\infty^t \mathrm{d}t' \frac{\sin\left[\sqrt{\omega_\ell^2-\gamma^2/4}\ (t-t')\right]}{\sqrt{\omega_\ell^2-\gamma^2/4}} e^{-\gamma(t-t')}\mathbf{F}(t') \tag{2.11}$$

and comparing it to the expression for the coordinate of a harmonic oscillator

$$\mathbf{x}(t) = \int_\infty^t \mathrm{d}t' g_{HO}(t-t')\frac{\mathbf{F}(t')}{m} \tag{2.12}$$

yielding an effective mass of the sphere

$$m_\ell = \frac{4\pi e^2[\ell(\epsilon_\infty+\epsilon_b)+\epsilon_b]}{(2\ell+1)V\omega_\ell^2}. \tag{2.13}$$

A similar treatment could be performed for non-spherical nanoparticle geometries as well. This treatment requires the nanoparticle boundary to be described in coordinate systems that are separable for the Laplace equation.

2.2.2 Retarded Treatment of Matter

In the previous section effects that arise due to the finite propagation of information were neglected, allowing for a simple treatment of the response of nanoparticles and allowed for the mapping of MNPs onto harmonic oscillators. This luxury is not afforded to us when including these retardation effects and the electric field must be treated generally

$$\mathbf{E}(\mathbf{r},\omega) = -i4\pi\omega\int_{-\infty}^{\infty}\mathrm{d}\mathbf{r}'\ \overline{\mathbf{G}}(\mathbf{r},\mathbf{r}',\omega)\cdot\mathbf{j}(\mathbf{r}',\omega) \tag{2.14}$$

where $\overline{\mathbf{G}}(\mathbf{r},\mathbf{r'},\omega)$ is the dyadic Green's function resulting from a delta function source at $\mathbf{r}'$ and $\mathbf{j}(\mathbf{r}',\omega)$ is an arbitrary current density that induces the electric field. The dyadic Green's function is obtained from solving the vector Helmholtz equation for a delta function source

$$\nabla \times \left(\nabla \times \overline{\mathbf{G}}(\mathbf{r}, \mathbf{r}', \omega)\right) - k^2 \overline{\mathbf{G}}(\mathbf{r}, \mathbf{r}', \omega) = \mathbb{1}\delta(\mathbf{r} - \mathbf{r}') \tag{2.15}$$

and is outlined in depth in Appendix A. The induced Green's function describing the electric field external to the sphere for an external current distribution is

$$\overline{\mathbf{G}}^{\text{ind}}_{\text{ext}}(\mathbf{r}, \mathbf{r}') = \frac{ik}{4\pi} \sum_{\ell=0}^{\infty} \sum_{m=0}^{\ell} \lambda_{\ell m} \left[A_\ell \mathbf{M}^{(1)}_{\substack{e \\ o}\ell m}(k) \mathbf{M}'^{(1)}_{\substack{e \\ o}\ell m}(k) + B_\ell \mathbf{N}^{(1)}_{\substack{e \\ o}\ell m}(k) \mathbf{N}'^{(1)}_{\substack{e \\ o}\ell m}(k) \right] \tag{2.16}$$

where A_ℓ and B_ℓ are EELS Mie coefficients, $\lambda_{\ell m}$ is a numerical prefactor, and $\mathbf{M}^{(1)}_{\substack{e \\ o}\ell m}$ and $\mathbf{N}^{(1)}_{\substack{e \\ o}\ell m}(k)$ are vector spherical harmonics containing spherical Hankel functions. This form of the Green's function will be used for determining an EELS expression that includes retardation effects, which is necessary for chapter 6.

2.3 Interaction of the Relativistic Electron with Matter

EELS is a technique used to interrogate the electric and optical properties of systems on the nanoscale. In this experiment electrons are accelerated to relativistic speeds in a TEM and directed to pass by a system. During the transit of the electron by some dielectric object, the electric field of the electron interacts with the charged particles in the dielectric body polarizing the material. The polarization field of the dielectric system in turn acts back onto the electron reducing the overall kinetic energy of the electron. When this "slowed" electron passes to the detector the final kinetic energy is used to determine the amount of energy imparted from the electron into the dielectric system. This interaction is quantum mechanical in nature, however, through a large number of individual "experiments" the EELS observable is measured.

Since the interaction between relativistic electron and nanostructure is statistical in nature, a classical treatment is sufficient for determining the EELS observable. This approach is not unique to this dissertation and has been used previously to model EELS [46]. Consider the frame of the electron and the change in energy it experiences. The average change in energy can be equated to the first energy moment of an energy distribution function

$$\langle \Delta\mathcal{E} \rangle = \int_0^\infty \mathrm{d}(\hbar\omega)\ \hbar\omega\ \Gamma_{\mathrm{EELS}}(\omega), \tag{2.17}$$

where $\Gamma_{\mathrm{EELS}}(\omega)$ is the distribution function describing the EELS observable. This statistical definition of the expected energy loss is useless on its own as it does not contain any information pertaining to the system. We gain more utility by considering the expected change in kinetic energy of the electron by considering the time averaged power absorbed due to mechanical work

$$\langle \Delta\mathcal{E} \rangle = \int_{-\infty}^\infty \mathrm{d}t\ \mathbf{F}(\mathbf{x}, t) \cdot \dot{\mathbf{x}}(t). \tag{2.18}$$

Combining Eq. 2.17 and 2.18 allows for a more useful expression of the EELS observable

$$\int_0^\infty \mathrm{d}(\hbar\omega)\ \hbar\omega\ \Gamma_{\mathrm{EELS}}(\omega) = \int_{-\infty}^\infty \mathrm{d}t\ \mathbf{F}(\mathbf{x}, t) \cdot \dot{\mathbf{x}}(t). \tag{2.19}$$

There is some freedom in how these quantities for force and velocity are defined. The force can be the force acting on the electron's velocity due to the induced electric field from the nanoparticle. Alternatively, the force could be attributed the electric field of the electron acting on the velocity term, which represents a generalized coordinate of the nanoparticle. While both treatments yield the same results the system under interrogation and any approximations made dictate which approach is more useful.

2.3.1 Quasistatic Treatment of Electron Energy-Loss Spectroscopy

A quasistatic treatment of EELS uses a theory of matter that is in the quasistatic limit, more specifically a Green's function approach for Gauss's law is used to determine the form of the force or velocity in the EELS expression given earlier in this section. In this limit we shall only concern ourselves with metal nanoparticles, the dynamics of which can be mapped onto a harmonic oscillator as previously shown.

With this in mind, our quasistatic treatment begins with rewriting the right hand side of Eq. 2.19. Currently this equation is unwieldy as each side of the equation are being integrated

over different variables with different bounds. The goal is equate integrands on both sides of the equation, requiring the integrals to be over the same domain. This becomes more convenient by considering the nanoparticle dynamics in the Fourier domain by expressing the time dependent dynamics in terms of its inverse Fourier transform

$$\int_{-\infty}^{\infty} \mathrm{d}t\ \mathbf{F}(\mathbf{x},t)\cdot\dot{\mathbf{x}}(t) = \frac{1}{2\pi}\int_{-\infty}^{\infty} \mathrm{d}t\ \mathbf{F}(\mathbf{x},t)\cdot \mathrm{Re}\left\{\int_{-\infty}^{\infty} \mathrm{d}\omega\ (-i\omega)\tilde{\mathbf{x}}(\omega)e^{-i\omega t}\right\} \tag{2.20}$$

where the time derivative was trivially evaluated on the exponential term. The force in the time domain is an observable and therefore real valued. This allows the force expression to be moved into the real evaluation. Additionally, a factor of i can be removed from this expression resulting in evaluating the imaginary part rather than the real part of the expression. Next, evaluating the time integral Fourier transforms the force. However, due to the incorrect sign for the argument of the exponential, the force in the Fourier domain will be evaluated at negative frequency

$$-\frac{1}{2\pi}\int_{-\infty}^{\infty} \mathrm{d}t\ \mathrm{Im}\left\{\int_{-\infty}^{\infty} \mathrm{d}\omega\ \omega\mathbf{F}(\mathbf{x},t)\cdot\tilde{\mathbf{x}}(\omega)e^{-i\omega t}\right\} = -\frac{1}{2\pi}\ \int_{-\infty}^{\infty} \mathrm{d}\omega\ \omega\mathrm{Im}\{\tilde{\mathbf{F}}^{*}(\mathbf{x},\omega)\cdot\tilde{\mathbf{x}}(\omega)\} \tag{2.21}$$

where the negative argument of the force is replaced with the complex conjugate of the force with positive argument. Now the integration variable is the same for this expression and the expression relating the EELS observable, however, the bounds still differ. The integral can now be broken into regions of $(-\infty \to 0)$ and $(0 \to \infty)$, where the first integral will be substituted for positive bounds. This yields the difference of a function with its complex conjugate, which is twice the imaginary component resulting in

$$\int_{0}^{\infty} \mathrm{d}(\hbar\omega)\ \hbar\omega\ \Gamma_{\mathrm{EELS}}(\omega) = -\frac{1}{\pi}\int_{0}^{\infty} \mathrm{d}\omega\ \omega\mathrm{Im}\{\tilde{\mathbf{F}}^{*}(\mathbf{x},\omega)\cdot\tilde{\mathbf{x}}(\omega)\} \tag{2.22}$$

and solving for Γ_{EELS}

$$\Gamma_{\mathrm{EELS}}(\omega) = -\frac{1}{\pi\hbar^{2}}\mathrm{Im}\{\tilde{\mathbf{F}}^{*}(\mathbf{x},\omega)\cdot\tilde{\mathbf{x}}(\omega)\}. \tag{2.23}$$

Here it is important to note that no assumptions were made about the particle with which the electron is interacting. This expression is general and can be used for any system in which the force and nanoparticle coordinate is well defined.

Single Metal Nanosphere

First, we shall consider the case of a single MNP, the dynamics of which were shown previously to map onto a harmonic oscillator. The equation of motion for a dampened-driven harmonic oscillator is of the form

$$\ddot{\mathbf{x}}_{\ell m} + \gamma_{\ell m}\dot{\mathbf{x}}_{\ell m} + \omega_{\ell m}^2 \mathbf{x}_{\ell m} = \mathbf{F}(\mathbf{x}, t)/m_{\ell m} \tag{2.24}$$

where $\gamma_{\ell m}$ represents the various decay pathways that result in friction on the oscillator and $m_{\ell m}$ is the effective mass of the oscillator. While this is rather complicated to deal with in its current form, the equation of motion is readily solved via a Fourier transform, where the frequency dependent motion has the form

$$\tilde{\mathbf{x}}_{\ell m}(\omega) = \frac{\tilde{\mathbf{F}}(\mathbf{x}, \omega)}{m_{\ell m}(\omega_{\ell m}^2 - \omega^2 - i\gamma_{\ell m}\omega)}. \tag{2.25}$$

For simplicity $Z_{\ell m} = (\omega_{\ell m}^2 - \omega^2 - i\gamma_{\ell m}\omega)$ defines the resonant structure of the ℓmth mode.

Now that the dynamics of the driven harmonic oscillator have been determined, we can finally write an expression for EELS. Inserting this into Eq. 2.23 and summing over all of our ℓ modes and m orientations we obtain

$$\Gamma_{\mathrm{EELS}}(\omega) = -\frac{\left|\tilde{\mathbf{F}}(\mathbf{x}, \omega)\right|^2}{\pi\hbar} \sum_{\ell=0}^{\infty} \sum_{m=-\ell}^{\ell} \mathrm{Im}\left\{\frac{1}{m_{\ell m} Z_{\ell m}}\right\}. \tag{2.26}$$

This can be rewritten in terms of the polarizability

$$\Gamma_{\mathrm{EELS}}(\omega) = \frac{\left|\tilde{\mathbf{F}}(\mathbf{x}, \omega)\right|^2}{e^2\pi\hbar} \mathrm{Im}\{\alpha(\omega)\}. \tag{2.27}$$

Dimer of Metal Nanospheres

The approach of mapping the plasmon coordinate onto a harmonic oscillator lends itself to a simple treatment of aggregates. The general expression for EELS for an aggregate of nanoparticles is simply the sum of mechanical work associated with each particle

$$\Gamma_{\mathrm{EELS}}(\omega) = -\frac{1}{\pi\hbar^2}\sum_i \mathrm{Im}\{\tilde{\mathbf{F}}^*(\mathbf{x}_i,\omega)\cdot\tilde{\mathbf{x}}_i(\omega)\}. \tag{2.28}$$

While this expression can be evaluated in a few ways, the most straightforward method absorbs the interaction of particles in the nanoparticle dynamics. For the case of two metal nanospheres that are electromagnetically coupled, the equations of motion are

$$\begin{aligned}\ddot{\mathbf{x}}_1 + \gamma_1\dot{\mathbf{x}}_1 + \omega_1^2\mathbf{x}_1 - g\mathbf{x}_2/m_1 &= \mathbf{F}(\mathbf{x}_1,t)/m_1\\ \ddot{\mathbf{x}}_2 + \gamma_2\dot{\mathbf{x}}_2 + \omega_2^2\mathbf{x}_2 - g\mathbf{x}_1/m_2 &= \mathbf{F}(\mathbf{x}_2,t)/m_2\end{aligned} \tag{2.29}$$

where coupling between arbitrary modes is represented by g, and alters the dynamics of both nanoparticles. Using the same method of Fourier transforming both equations of motion and solving for each variable yields

$$\tilde{\mathbf{x}}_i = \frac{\tilde{\mathbf{F}}(\mathbf{x}_i,\omega)Z_j}{m_i[Z_iZ_j - g^2/m_im_j]} + \frac{g\tilde{\mathbf{F}}(\mathbf{x}_j,\omega)}{[m_im_jZ_iZ_j - g^2]} \tag{2.30}$$

where $Z_i = (\omega_i^2 - \omega^2 - i\gamma_i\omega)$ defines the resonance structure for the mode on the ith particle. This leads to an EELS expression

$$\begin{aligned}\Gamma_{\mathrm{EELS}}(\omega) = -\frac{1}{\pi\hbar}\mathrm{Im}\Big\{&\tilde{\mathbf{F}}^*(\mathbf{x}_1,\omega)\cdot\left(\frac{\tilde{\mathbf{F}}(\mathbf{x}_1,\omega)Z_2}{m_1[Z_1Z_2 - g^2/m_1m_2]} + \frac{g\tilde{\mathbf{F}}(\mathbf{x}_2,\omega)}{[m_1m_2Z_1Z_2 - g^2]}\right)\\ &+ \tilde{\mathbf{F}}^*(\mathbf{x}_2,\omega)\cdot\left(\frac{\tilde{\mathbf{F}}(\mathbf{x}_2,\omega)Z_1}{m_2[Z_1Z_2 - g^2/m_1m_2]} + \frac{g\tilde{\mathbf{F}}(\mathbf{x}_1,\omega)}{[m_1m_2Z_1Z_2 - g^2]}\right)\Big\}.\end{aligned} \tag{2.31}$$

This expression is considerably more complicated than the single particle case or even the sum to two uncoupled particles ($g = 0$), however, these terms can be considered individually.

2.3.2 Retarded Treatment of Electron Energy-Loss Spectroscopy

Previously the derivation of an EELS expression included approximations regarding the speed in which information can travel. In the quasistatic limit this is taken to be instantaneous, neglecting the effects of retardation due to information propagating at a finite speed. Including effects due to retardation will influence the form of our electric field, however, the same methodology can be used as given in Eq. 2.18. Our treatment here begins with rewriting this expression in terms of a current and an electric field

$$\langle \Delta\mathcal{E} \rangle = \int_{-\infty}^{\infty} \mathrm{d}t \; \mathbf{E}(\mathbf{r},t) \cdot \mathbf{J}(\mathbf{r},t). \tag{2.32}$$

Previously for metals we were able to map a polarizable coordinate onto a harmonic oscillator due to the nature of the induced Green's function. This luxury does not exist when including retardation and the electric field must be treated generally as the induced electric field from a current associated with the passing electron. The general electric field is defined

$$\mathbf{E}(\mathbf{r},\omega) = -i4\pi\omega \int_{-\infty}^{\infty} \mathrm{d}\mathbf{r}' \; \overline{\mathbf{G}}(\mathbf{r},\mathbf{r}',\omega) \cdot \mathbf{j}(\mathbf{r}',\omega) \tag{2.33}$$

where $\overline{\mathbf{G}}(\mathbf{r},\mathbf{r'},\omega)$ is the dyadic Green's function resulting from a delta function source at $\mathbf{r}'$ and $\mathbf{j}(\mathbf{r}',\omega)$ is an arbitrary current density that induces the electric field. The dyadic Green's function is obtained from a vector Helmholtz equation

$$\nabla \times \big(\nabla \times \overline{\mathbf{G}}(\mathbf{r},\mathbf{r}',\omega)\big) - k^2 \overline{\mathbf{G}}(\mathbf{r},\mathbf{r}',\omega) = \mathbb{1}\delta(\mathbf{r}-\mathbf{r}'). \tag{2.34}$$

The EELS expression can be re-expressed using the dyadic Green's function and the current density of the excitation source

$$\Gamma_{\mathrm{EELS}}(\omega) = -\frac{4}{\hbar^2} \int_{-\infty}^{\infty} \mathrm{d}\mathbf{r}\mathrm{d}\mathbf{r}' \mathrm{Im}\{\mathbf{j}(\mathbf{r}',\omega) \cdot \overline{\mathbf{G}}(\mathbf{r},\mathbf{r}',\omega) \cdot \mathbf{j}^*(\mathbf{r},\omega)\}. \tag{2.35}$$

The current densities in this expression represent the current density of the passing electron which can be described rather simply as delta function with charge, e, moving with

a velocity, v, in the z-direction. We can further select the location in the xy-plane in which which the electron is located. Choosing a displacement from the origin in the x direction we arrive at a current density

$$\begin{aligned}\mathbf{j}(\mathbf{r},t) =& ev\delta(x-b)\delta(y)\delta(z-vt)\hat{z}\\ \mathbf{j}(\mathbf{r},\omega) =& e\delta(x-b)\delta(y)e^{-i\omega z/v}\hat{z}.\end{aligned} \tag{2.36}$$

This current density allows for the trivial evaluation of four of the six spatial integrals, resulting in an EELS expression that is only dependence on the z and z' coordinate

$$\Gamma_{\mathrm{EELS}}(\omega) = -\frac{4e^2}{\hbar^2}\int_{-\infty}^{\infty}\mathrm{d}z\mathrm{d}z'\mathrm{Im}\{\hat{z}\cdot\overline{\mathbf{G}}(b,z,z',\omega)\cdot\hat{z}e^{i\omega(z-z')/v}\}. \tag{2.37}$$

Here, the zz element of Green's dyad is the only contributor to the EEL probability. This expression is general for any nanoparticle geometry in which an analytic form of the dyadic Green's function exists. We will consider the case of a spherical geometry with a homogeneous dielectric. The dyadic Green's function expressed in the appropriate basis of vector spherical harmonics is

$$\overline{\mathbf{G}}(\mathbf{r},\mathbf{r}',\omega) = \frac{\omega}{c}\sum_{\ell=0}^{\infty}\sum_{m=0}^{\ell}\lambda_{\ell m}\left[A_\ell\mathbf{M}_{\substack{e\\o}\ell m}(\mathbf{r},\omega)\mathbf{M}_{\substack{e\\o}\ell m}(\mathbf{r}',\omega)+B_\ell\mathbf{N}_{\substack{e\\o}\ell m}(\mathbf{r},\omega)\mathbf{N}_{\substack{e\\o}\ell m}(\mathbf{r}',\omega)\right] \tag{2.38}$$

where a prefactor of numerical coefficients, $\lambda_{\ell m}$ is defined as

$$\lambda_{\ell m} = \frac{(2-\delta_{m0})(2\ell+1)(\ell-m)!}{4\pi\ell(\ell+1)(\ell+m)!}, \tag{2.39}$$

and A_ℓ and B_ℓ are currently unknown and represent the EELS Mie coefficients. These coefficients will contain all of the resonance information for the nanoparticle, while the degree to which the ℓmth mode is forced is contained in the vector spherical harmonics weighted by $\lambda_{\ell m}$. The Mie coefficients are determined by solving for the appropriate boundary conditions

$$\begin{aligned}\left[\hat{r}\times\overline{\mathbf{G}}(\mathbf{r},\mathbf{r}',\omega)\right]_{r=a-} &= \left[\hat{r}\times\overline{\mathbf{G}}(\mathbf{r},\mathbf{r}',\omega)\right]_{r=a+}\\ \left[\hat{r}\times(\nabla\times\overline{\mathbf{G}}(\mathbf{r},\mathbf{r}',\omega))\right]_{r=a-} &= \left[\hat{r}\times(\nabla\times\overline{\mathbf{G}}(\mathbf{r},\mathbf{r}',\omega))\right]_{r=a+}\end{aligned} \tag{2.40}$$

which follow the same boundary conditions as the electric field at a dielectric interface. This results in EELS Mie coefficients of the form

$$\begin{aligned} A_\ell =& -i\frac{j_\ell(\rho_1)[\rho_2 j_\ell(\rho_2)]' - j_\ell(\rho_2)[\rho_1 j_\ell(\rho_1)]'}{h_\ell^{(1)}(\rho_1)[\rho_2 j_\ell(\rho_2)]' - j_\ell(\rho_2)[\rho_1 h_\ell^{(1)}(\rho_1)]'} \\ B_\ell =& -i\frac{N^2 j_\ell(\rho_2)[\rho_1 j_\ell(\rho_1)]' - j_\ell(\rho_1)[\rho_2 j_\ell(\rho_2)]'}{N^2 j_\ell(\rho_2)[\rho_1 h_\ell^{(1)}(\rho_1)]' - h_\ell^{(1)}(\rho_1)[\rho_2 j_\ell(\rho_2)]'} \end{aligned} \tag{2.41}$$

where A_ℓ describes the transverse magnetic modes and B_ℓ describes the transverse electric modes of the sphere. Inserting this result into the form of the dyadic Green's function and evaluating the integrals in Eq. 2.35 yields

$$\Gamma_{\text{EELS}}(\omega) = \frac{e^2}{\hbar^2 c\omega}\sum_{\ell=0}^{\infty}\sum_{m=-\ell}^{\ell} K_m^2\left(\frac{\omega b}{v\gamma_L}\right)\left[C_{\ell m}^A \text{Im}\left\{A_\ell\right\} + C_{\ell m}^B \text{Im}\left\{B_\ell\right\}\right] \tag{2.42}$$

where $C_{\ell m}^A$ and $C_{\ell m}^B$ are velocity dependent coefficients which hold the same form as those provided by García de Abajo [47, 46]

$$\begin{aligned} C_{\ell m}^A =& \frac{|2mN_{\ell m}|^2}{\ell(\ell+1)} \\ C_{\ell m}^B =& \frac{c^2|M_{\ell m}|^2}{v^2\gamma_L^2\ell(\ell+1)} \end{aligned} \tag{2.43}$$

where

$$\begin{aligned} N_{\ell m} =& \sqrt{\frac{(2\ell+1)(\ell-|m|)!}{\pi(\ell+|m|)!}}\sum_{\alpha=0}^{\left[\frac{\ell-|m|}{2}\right]}\frac{(-2)^{-\alpha}}{\gamma_L^{|m|}}\frac{(2\ell-2\alpha-1)!!}{\alpha!(\ell-|m|-2\alpha)!}\left(\frac{c}{v}\right)^{\ell-2\alpha} \\ M_{\ell m} =& N_{\ell m+1}\sqrt{(\ell+m+1)(\ell-m)} + N_{\ell m-1}\sqrt{(\ell-m+1)(\ell+m)}. \end{aligned} \tag{2.44}$$

2.4 Simulation and Numerical Methods for Electron Energy-Loss Spectroscopy

Prior to era of computers, theory was only capable of accurately predicting simple systems in which analytic solutions exist. For EELS, the full solution for the "simple" case of a sphere

is in itself a challenging problem. This limitation on the systems that could be accurately described by theory loosened as technology progressed and computational resources became ubiquitous. This allowed for the use of theory with numerical approximations to approach more complex problems. Systems in later chapters were explored with a combination of simulation and analytic theory to provide as much insight as possible. The numerical methods used to solve Maxwell's equations were the **Discrete Dipole Approximation** and the **Boundary Element Method**.

2.4.1 Discrete Dipole Approximation

The discrete-dipole approximation (DDA) was first proposed by DeVoe in 1964 [38], and modified to include effects due to retardation by Purcell and Pennypacker in 1973 [124]. The DDA numerically represents arbitrarily shaped dielectric particles by a collection of polarizable volume elements. These volume elements are modelled as a dipole holding a Clausius-Mossotti polarizability

$$\mathbf{p}_i = \alpha_i \mathbf{E}(\mathbf{x}_i). \tag{2.45}$$

where $\alpha_i = a^3(\epsilon_i(\omega) - \epsilon_b)/(\epsilon_i(\omega) + 2\epsilon_b)$ (Here for simplicity lattice dispersion is not being included in the definition for the polarizability), and $\mathbf{E}(\mathbf{x}_i)$ is the total electric field at dipole i. This is trivial for a single dipole as the total electric field is the incident electric field. For multiple dipoles, the form of $\mathbf{E}(\mathbf{x}_i)$ is non-trivial. The total electric field at dipole i is given by

$$\mathbf{E}(\mathbf{x}_i, \omega) = \mathbf{E}_0(\mathbf{x}_i, \omega) + \sum_{j \neq i} \overline{\mathbf{\Lambda}}_{ij} \cdot \mathbf{p}_j \tag{2.46}$$

where

$$\overline{\mathbf{\Lambda}}_{ij} = \frac{e^{ikr_{ij}}}{\epsilon_b} \left[\left(\frac{1}{r_{ij}^3} - \frac{ik}{r_{ij}^2} \right) (3\hat{n}_{ij}\hat{n}_{ij} - \mathbb{1}) + \frac{k^2}{r_{ij}} (\mathbb{1} - \hat{n}_{ij}\hat{n}_{ij}) \right] \tag{2.47}$$

is the dipole relay tensor. The unit vector $\hat{n}_{ij}$ points from dipole i to j and r_{ij} is the separation distance between dipoles. Since the ith dipole has dependence on the jth dipole, which is also dependent on the ith dipole, the equation must be iteratively solved until all of the dipoles reach self consistency. Once the dipole configurations are obtained, observables such as field quantities and cross sections can be readily obtained.

The DDA framework used in later chapters is based on DDSCAT developed by Bruce Draine's group [39]. This framework was modified to use an incident electric field as given in Eq. 2.4, allowing for the calculation of EELS and Cathodoluminescence probabilities. This is made possible by modifying Eq. 2.23 to be expressed in terms of dipole moments

$$\Gamma_{\mathrm{EELS}}(\omega) = -\frac{1}{\pi\hbar^2}\sum_{i}^{N}\mathrm{Im}\{\tilde{\mathbf{E}}^{*}_{inc}(\mathbf{x},\omega)\cdot\tilde{\mathbf{p}}(\omega)\}. \tag{2.48}$$

This method of determining EEL probabilities is very accurate for systems that are discretized such that individual volume elements are much smaller than other length scales within the system.

2.4.2 Boundary Element Method

For systems containing particles represented by a homogeneous, isotropic dielectric function, a technique known as the boundary element method (BEM) can be used. The BEM uses an integral formulation of Maxwell's equations in the Fourier domain where only the behavior at the particle boundaries must be considered. The groundwork for the use of BEM for EELS was laid out by Fuchs [45] and further developed by García de Abajo [48]. The description of BEM in this section follows the treatment by García de Abajo [48].

The general premise of BEM involves the consideration of interfaces separating two media holding different dielectric properties. The scalar and vector potentials satisfy the wave equation

$$\begin{aligned}(\nabla^2 + k^2\epsilon\mu)\phi =& -4\pi\left(\frac{\rho}{\epsilon} + \sigma_s\right)\\ (\nabla^2 + k^2\epsilon\mu)\mathbf{A} =& -\frac{4\pi}{c}(\mu\mathbf{j} + \mathbf{h})\end{aligned} \tag{2.49}$$

where σ_s and $\mathbf{h}$ represent charges and currents that arise due to the dielectric interface. These have the form

$$\begin{aligned}\sigma_s =& \frac{1}{4\pi}\mathbf{D}\cdot\nabla\frac{1}{\epsilon}\\ \mathbf{h} =& -\frac{1}{4\pi}[i\omega\phi\nabla(\epsilon\mu) + c\mathbf{H}\times\nabla\mu].\end{aligned} \tag{2.50}$$

These quantities hold a non-zero value at dielectric interfaces and act as an additional source generating potentials. While the current, $\mathbf{h}$, does not represent a physical current, the surface charge, σ_s, is connected to the polarization charges at the interface and both quantities can be solved for using the appropriate boundary conditions

$$\begin{aligned}G_1\sigma_1 - G_2\sigma_2 =& \phi_2^{ext} - \phi_1^{ext}\\ G_1\mathbf{h}_1 - G_2\mathbf{h}_2 =& \mathbf{A}_2^{ext} - \mathbf{A}_1^{ext}\end{aligned} \tag{2.51}$$

where the Green's function in these expressions is for the wave equation in a medium denoted by the subscript, and the potentials on the right hand side of the equations are those attributed to an external source. This is the case for a single planar boundary, however, in BEM arbitrary geometries are discretized into a series of surface elements which interact through induced potentials attributed to the surface charges and currents on each element

$$\begin{aligned}\phi^{ind}(\mathbf{r}) &= \int_S \mathrm{d}\mathbf{s}G_i(|\mathbf{r}-\mathbf{s}|)\sigma_i(\mathbf{s})\\ \mathbf{A}^{ind}(\mathbf{r}) &= \int_S \mathrm{d}\mathbf{s}G_i(|\mathbf{r}-\mathbf{s}|)\mathbf{h}_i(\mathbf{s}).\end{aligned} \tag{2.52}$$

Since each surface charge and current depends on all of the other surface elements, the values for these quantities must be self consistently solved. The final quantities of σ_s and $\mathbf{h}$ are then

used for determining observables. The specific implementation used in later chapters is the Metal Nanoparticle Boundary Element Method (MNPBEM) [61].

Chapter 3

FANO INTERFERENCES OBSERVED BY ELECTRON ENERGY-LOSS SPECTROSCOPY AND CATHODOLUMINESCENCE

3.1 Introduction

The concept of interference transcends the somewhat arbitrary boundaries between fields and is observed in many instances in nature, spanning the fields of acoustics, fluid dynamics, optics, and in general anything with wave-like properties. In 1961 the interference of discrete auto-ionization states with a continuum was used to explain the asymmetric line shape observed in helium excitations by Ugo Fano [43]. This class of constructive and destructive interferences between a narrow discrete state and a broad continuum gives rise to an asymmetric line shape and has been deemed a Fano interference or Fano resonance.

Typically Fano interferences have been associated with quantum mechanical systems [72, 79, 102] due to the narrow discrete energy levels in such systems, however, this phenomenon has been observed in classical systems as well [58, 59, 89, 135]. This behavior in classical systems was shown to agree with the interference observed by Fano [43], and over time this character was observed in a variety of systems including plasmonic particles and aggregates [98, 106, 107, 149].

The sharp spectral features attributed to Fano interferences allow for detection of changes in the local environment with a high degree of sensitivity. The ability to track shifts and alterations of these features allows for potential use in chemical sensing, measuring temperature, and measuring pressure [102].

3.2 Methodology

Asymmetric, non-Lorentzian line shapes similar to those observed by Ugo Fano have been observed in optical spectra for metal nanoparticle aggregates. In such systems a "bright" plasmonic mode plays the role of the continuum of states which is coupled to a "dark" plasmonic mode which plays the role of a discrete state. Bright modes for these systems are those with a net dipole moment allowing for excitation by far-field radiation, while dark modes are inaccessible, or weakly accessible, via far-field sources.

When interrogating such systems using an electron from a TEM the role of "bright" and "dark" become less intuitive as the excitations by the electron obey different selection rules than those by far-field radiation. All of the modes of a nanoparticle are accessible by the electron with an appropriate selection of electron impact parameter. Consequently, modes can be "bright" or "dark" to the electron by selecting the impact parameter. This allows for a higher degree of tunability for Fano interferences than compared to far-field excitation sources. Signatures of Fano interferences, which were once thought to be inaccessible via the electron [88], are shown for EELS and CL in the following sections through an analytic treatment of electron-nanoparticle interactions.

3.2.1 Electron Energy-Loss Spectroscopy

The treatment of Fano interferences for EELS will begin with a general expression for two coupled plasmonic modes. This general expression was derived in the introductory chapter of this dissertation, where the form for two coupled oscillators is given as

$$\begin{aligned}\Gamma_{\mathrm{EELS}}(\omega) = -\frac{1}{\pi\hbar}\mathrm{Im}\Big\{\tilde{\mathbf{F}}^{*}(\mathbf{x}_1,\omega)\cdot\left(\frac{\tilde{\mathbf{F}}(\mathbf{x}_1,\omega)Z_2}{m_1[Z_1Z_2-g^2/m_1m_2]}+\frac{g\tilde{\mathbf{F}}(\mathbf{x}_2,\omega)}{[m_1m_2Z_1Z_2-g^2]}\right)\\ +\tilde{\mathbf{F}}^{*}(\mathbf{x}_2,\omega)\cdot\left(\frac{\tilde{\mathbf{F}}(\mathbf{x}_2,\omega)Z_1}{m_2[Z_1Z_2-g^2/m_1m_2]}+\frac{g\tilde{\mathbf{F}}(\mathbf{x}_1,\omega)}{[m_1m_2Z_1Z_2-g^2]}\right)\Big\}.\end{aligned} \tag{3.1}$$

where $\tilde{\mathbf{F}}^{*}(\mathbf{x}_i,\omega)$ is the electromagnetic force driving the plasmonic mode for particle i,

$Z_i = (\omega_i^2 - \omega^2 - i\gamma\omega)$ is the resonance conditions with ω_i representing the mode frequency, m_i represents the effective mass of the plasmonic mode mapped onto an oscillator, and g describes the coupling of the two oscillators, the form of which is determined by the identity of the two coupled modes.

Without a loss of generality for a Fano system, the mode of the second particle can be chosen to be dark. This correlates to placing the electron beam far from the second particle, resulting in a negligible forcing on this mode due to the evanescent nature of the electron's electric field. This simplifies the EELS expression for the Fano system, reducing to

$$\Gamma_{\mathrm{EELS}}(\omega) = -\frac{|\tilde{\mathbf{F}}(\mathbf{x}_1, \omega)|^2}{\pi\hbar}\mathrm{Im}\left\{\frac{Z_2}{m_1[Z_1Z_2 - g^2/m_1m_2]}\right\}. \tag{3.2}$$

The asymmetry that arises in the EELS spectrum can be further analyzed by considering the ratio of the EEL probability of the "bright" plasmonic mode that is perturbed via coupling to the "dark" plasmonic mode with the unperturbed "bright" mode. Dividing by this single particle EELS probability results in

$$\frac{\Gamma_{\mathrm{EELS}}(\omega)}{\Gamma^0_{\mathrm{EELS}}(\omega)} = \mathrm{Im}\left\{\frac{|Z_1|^2}{\gamma_1\omega}\frac{Z_2}{[Z_1Z_2 - g^2/m_1m_2]}\right\}. \tag{3.3}$$

Following the prescription provided by [148] moves this expression closer to the Fano's original work by defining the following quantities

$$\begin{aligned}
\Upsilon =& \gamma_2 + \frac{g^2\gamma_1}{m_1m_2[(\omega_1^2 - \omega^2)^2 + (\gamma_1\omega)^2]} \\
\Omega^2 =& \omega_2^2 - \frac{g^2\ (\omega_1^2 - \omega^2)}{m_1m_2[(\omega_1^2 - \omega^2)^2 + (\gamma_1\omega)^2]} \\
q_F =& \frac{\Omega^2 - \omega_2^2}{\omega(\Upsilon + \gamma_2)} + i\frac{\gamma_2}{\Upsilon + \gamma_2} \\
\epsilon =& \frac{(\omega^2 - \Omega^2)}{\omega(\Upsilon + \gamma_2)}.
\end{aligned} \tag{3.4}$$

Inserting these definitions and some algebra yields

$$\frac{\Gamma_{\mathrm{EELS}}(\omega)}{\Gamma^0_{\mathrm{EELS}}(\omega)} = \left|\frac{q_F+\epsilon}{\epsilon+i}\right|^2 + \frac{\mathrm{Im}\{q_F\}}{1-\mathrm{Im}\{q_F\}}\left|\frac{q_F-i}{\epsilon+1}\right|^2. \tag{3.5}$$

In the limit in which the second mode has zero friction this expression is identical in form to Fano's result and complete destructive interference would be observed when $\omega = \omega_1$ resulting in a dip in the EEL probability to zero. However, this is not observed as the dark mode is not truly a discrete state and has a finite width due to material friction. The second term in this expression corrects for this imperfection, resulting in interferences that dip to non-zero values.

3.2.2 Cathodoluminescence

In EELS an electron passes by a nanostructure imparting energy into electronic modes of the system. This change in energy experienced by the electron is blind to the path the energy transferred to the nanostructure takes beyond the initial interaction. In this sense the EELS experiment is an analog to optical extinction. An analog to optical scattering can be measured by detecting radiation emitted from the nanostructure. When an electron excites an electronic mode in a system, and the system radiatively decays the process is known as cathodoluminescence (CL). This technique can provide additional insight into the nature of the nanostructures under interrogation.

The analytic approach to modelling CL is less general than that of EELS, as a functional form of the electric and magnetic far-field must be chosen as will be seen in the derivation of the CL probability. First, we can consider the energy flowing through a spherical boundary infinitely far from the nanostructure

$$\Delta E = \int \mathrm{d}t \int \mathrm{d}\Omega \; r^2 \hat{r} \cdot \mathbf{S}(\mathbf{r}, t) \tag{3.6}$$

where $\mathbf{S}(\mathbf{r}, t)$ is the Poynting vector, a measure of electromagnetic energy flux. Putting this expression in explicitly for an arbitrary number of particles and transforming to the Fourier domain yields

$$\Delta E = \frac{c}{4\pi^2}\int_0^\infty \mathrm{d}\omega \int \mathrm{d}\Omega\ r^2 \sum_i \hat{r}\cdot \mathrm{Re}\left\{\mathbf{E}_i(\mathbf{r},\omega)\times\mathbf{B}_i^*(\mathbf{r},\omega)\right\} \tag{3.7}$$

where the interference terms $(\mathbf{E}_i(\mathbf{r},\omega)\times\mathbf{B}_j^*(\mathbf{r},\omega))$ are neglected, as conservation of energy requires an equal amount of constructive and destructive interference over the surface of the sphere.

The energy radiated can be treated statistically, similar to the treatment for EELS provided in chapter 1, by considering the first energy moment of a distribution function describing CL. This gives an additional expression for the energy radiated

$$\Delta E = \int_0^\infty \mathrm{d}(\hbar\omega)\ \hbar\omega\Gamma_{\mathrm{CL}}(\omega). \tag{3.8}$$

Equating 3.7 and 3.8 results in

$$\Gamma_{\mathrm{CL}}(\omega) = \frac{c}{4\pi^2\hbar^2\omega}\int \mathrm{d}\Omega\ r^2 \sum_i \hat{r}\cdot \mathrm{Re}\left\{\tilde{\mathbf{E}}_i(\mathbf{r},\omega)\times\tilde{\mathbf{B}}_i^*(\mathbf{r},\omega)\right\}. \tag{3.9}$$

Further evaluation of this expression requires a functional form of the electric and magnetic far-fields and therefore loses generality. Two case will be considered: dipole-dipole and dipole-quadrupole expressions for CL.

Dipole-Dipole Interaction

First the case is considered in which dipolar modes on each nanoparticle electromagnetically couple altering their dynamics. All of the effects of coupling can be absorbed into the expression for the dipole moment, $\tilde{\mathbf{p}}_i$, of each particle and the far-field expression for these dipoles can be written generally as

$$\begin{aligned} r\tilde{\mathbf{E}}_i(\mathbf{r}_i,\omega) =& k^2\left[(\hat{r}\times\tilde{\mathbf{p}}_i)\times\hat{r}\right]e^{ikr_i} \\ r\tilde{\mathbf{B}}_i^*(\mathbf{r}_i,\omega) =& k^2[\hat{r}\times\tilde{\mathbf{p}}_i^*]e^{-ikr_i} \end{aligned} \tag{3.10}$$

where we have absorbed factors of distance from the Jacobian factor in the integral for CL. The near and intermediate fields do not contribute to the CL as these fields decay too rapidly as a function of distance. The dipole fields can be inserted directly into the CL expression,

$$\Gamma_{\mathrm{CL}}^{d-d}(\omega) = \frac{\omega^3}{4\pi^2\hbar^2c^3}\int \mathrm{d}\Omega\; r^2 \sum_i \hat{r}\cdot \mathrm{Re}\left\{[(\hat{r}\times\tilde{\mathbf{p}}_i)\times\hat{r}]\times[\hat{r}\times\tilde{\mathbf{p}}_i^*]\right\} \tag{3.11}$$

where after some algebra a simplified CL expression is obtained

$$\Gamma_{\mathrm{CL}}^{d-d}(\omega) = \frac{2e^2\omega^3}{3\pi\hbar^2c^3}\sum_i |\tilde{\mathbf{x}}_i|^2 \tag{3.12}$$

where the integral over the spherical surface can been taken and the dipole moment has been expressed for a generalized coordinate describing the dipole plasmon.

Next, we must focus our attention on the dynamics of the coupled modes to obtain a more useful expression describing the CL of the dimer system. The general expression for the dynamics of a coupled dimer is

$$\tilde{\mathbf{x}}_i = \frac{\tilde{\mathbf{F}}(\mathbf{x}_i,\omega)Z_j}{m_i[Z_iZ_j - g^2/m_im_j]} + \frac{g\tilde{\mathbf{F}}(\mathbf{x}_j,\omega)}{[m_im_jZ_iZ_j - g^2]}. \tag{3.13}$$

Approximations can be made at the level of the dynamics that transform this expression into a Fano system, namely that the force acting on the second nanoparticle is zero due to the choice in electron beam position. This results in the following dynamics

$$\begin{aligned}\tilde{\mathbf{x}}_1 =& \frac{m_2Z_2\tilde{\mathbf{F}}(\mathbf{x}_1,\omega)}{[m_1m_2Z_1Z_2 - g^2]}\\ \tilde{\mathbf{x}}_2 =& \frac{g\tilde{\mathbf{F}}(\mathbf{x}_1,\omega)}{[m_1m_2Z_1Z_2 - g^2]} = \tilde{\mathbf{x}}_1\frac{g}{m_2Z_2}.\end{aligned} \tag{3.14}$$

The CL can be re-expressed using these forms of the dynamics. Normalizing by the uncoupled "bright" particle yields

$$\frac{\Gamma_{\mathrm{CL}}^{d-d}(\omega)}{\Gamma_{\mathrm{CL}}^{0}(\omega)} = \left|\frac{m_1m_2Z_1Z_2}{[m_1m_2Z_1Z_2 - g^2]}\right|^2\left[1 + \frac{g^2}{m_2^2|Z_2|^2}\right] \tag{3.15}$$

which can be further evaluated using the definitions in Eq. 3.4

$$\frac{\Gamma_{\mathrm{CL}}^{d-d}(\omega)}{\Gamma_{\mathrm{CL}}^{0}(\omega)} = \left|\frac{\epsilon + q_F}{\epsilon + i}\right|^2 \left[1 + \frac{g^2}{m_2^2 |Z_2|^2}\right]. \tag{3.16}$$

This expression has a form similar to the first term seen in EELS. It is identical to this term weighted by the magnitude of oscillator of the "dark mode". It is important to note that q_F is complex valued and will not completely interfere, however, interference in CL will be more pronounced than the interference observed in EELS.

Dipole-Quadrupole Interaction

The expression for Fano systems in EELS was much more general than that of CL. Any difference between treating the "dark" mode as a dipole or quadrupole was wrapped up in the coupling coefficient, g, and would not alter the form of the equations being used. In CL the form of the electric and magnetic far-fields are

$$\begin{aligned} r\tilde{\mathbf{E}}_q(\mathbf{r},\omega) &= i\frac{k^3}{6}\left[\hat{r}\times(\hat{r}\times\tilde{\mathbf{Q}})\right]e^{ikr} \\ r\tilde{\mathbf{B}}_q^*(\mathbf{r},\omega) &= i\frac{k^3}{6}\left[\hat{r}\times\tilde{\mathbf{Q}}\right]e^{-ikr}. \end{aligned} \tag{3.17}$$

where $\tilde{\mathbf{Q}}$ is the quadrupole moment, evaluated in a vector form (i.e. $\mathbf{Q} = \sum_\beta Q_{\alpha\beta} r_\beta$). This is identical to the method used by Jackson [69] to evaluate quadrupole radiation.

In the treatment of the dipole-dipole interaction, it was stated that the interference terms over the entire sphere evaluate to zero. The same holds true for the case of dipole-quadrupole interactions. Once again the CL expression can be described as the sum of the individual contributions for the dipole and the quadrupole

$$\Gamma_{\mathrm{CL}}^{d-q}(\omega) = \Gamma_{\mathrm{CL}}^{dip}(\omega) + \Gamma_{\mathrm{CL}}^{quad}(\omega) \tag{3.18}$$

where the dynamics of each mode are altered due to the coupling of the nanoparticles. The CL expression for dipolar radiation can be used in this case, as the difference between system

lies in the form of coupling which is in the underlying dynamics. The dipole contribution is therefore

$$\Gamma_{\mathrm{CL}}^{dip}(\omega) = \frac{2\omega^4}{3\pi\hbar^2 c^3}|\tilde{\mathbf{p}}|^2. \tag{3.19}$$

The contribution to CL from the quadrupole is more complicated than the case of the dipole as each element in the quadrupole "vector" contains information describing a vector. This complicates vector operations performed, specifically

$$\begin{aligned} \mathbf{Q}^* \cdot \mathbf{Q} =& \sum_{\alpha\beta\gamma} Q^*_{\alpha\beta} Q_{\alpha\gamma} r_\beta r_\gamma \\ |\hat{n} \cdot \mathbf{Q}|^2 =& \sum_{\alpha\beta\gamma\delta} Q^*_{\alpha\beta} Q_{\gamma\delta} r_\alpha r_\beta r_\gamma r_\delta. \end{aligned} \tag{3.20}$$

Conveniently, the only spatial dependence on these operations involves the rectangular components of the unit vector describing a point in space in the far field. These integrals are readily evaluated [69]

$$\begin{aligned} \int \mathrm{d}\Omega r_\beta r_\gamma =& \frac{4\pi}{3}\delta_{\beta\gamma} \\ \int \mathrm{d}\Omega r_\alpha r_\beta r_\gamma r_\delta =& \frac{4\pi}{15}(\delta_{\alpha\beta}\delta_{\gamma\delta} + \delta_{\alpha\gamma}\delta_{\beta\delta} + \delta_{\alpha\delta}\delta_{\beta\gamma}). \end{aligned} \tag{3.21}$$

From these identities, the traceless nature of the quadrupole tensor, and some algebra, we obtain the quadrupole contribution to CL

$$\Gamma_{\mathrm{CL}}^{quad}(\omega) = \frac{\omega^6}{180\pi\hbar^2 c^5} \sum_{\alpha\beta} |\tilde{Q}_{\alpha\beta}|^2, \tag{3.22}$$

where α and β are indices for the quadrupole tensor. In general not all of the elements of the quadrupole tensor will contribute to radiation for this system as not all quadrupole modes will be driven from the dipole.

The dynamics of the quadrupole are similar to those of the dipole in the sense that the generalized coordinate will undergo damped harmonic motion, that is

$$\tilde{Q}_{\alpha\beta} = \frac{\tilde{F}_{\alpha\beta}(\mathbf{x}_{\alpha\beta},\omega)Z_{dip}}{m_{\alpha\beta}[Z_{\alpha\beta}Z_{dip} - g_{\alpha\beta}^2/m_{\alpha\beta}m_{dip}]} + \frac{g_{\alpha\beta}\tilde{F}_{\beta}(\mathbf{x}_{dip},\omega)}{[m_{\alpha\beta}m_{dip}Z_{\alpha\beta}Z_{dip} - g_{\alpha\beta}^2]}. \tag{3.23}$$

for the case of a quadrupole coupled to a dipole. Here $Z_{\alpha\beta} = (\omega_{\alpha\beta}^2 - \omega^2 - i\gamma_{\alpha\beta}\omega)$, $m_{\alpha\beta}$ is the mass of the quadrupole which can differ for each $\alpha\beta$ mode for arbitrary geometries, and $\tilde{\mathbf{F}}(\mathbf{x}_{\alpha\beta},\omega)$ is the force driving the quadrupole. In contrast to dipoles, quadrupoles are not forced by the electric field, but by the curvature of the electric field, i.e. $\tilde{\mathbf{F}}(\mathbf{x}_{\alpha\beta},\omega) \propto (e\nabla\tilde{\mathbf{E}}(\mathbf{x}_{\alpha\beta},\omega)$ [69], where an outer product is taken resulting in a tensor, the elements of which force the quadrupole modes corresponding the that element. Additionally, due to the difference in the manner the quadrupole is driven, the coupling coefficient g holds a different form that takes into account the curvature of the dipole electric field, i.e. $g \propto e\nabla(\overline{\mathbf{\Lambda}}_{ij} \cdot \mathbf{x}_{dip})$, which is also a tensor quantity.

When considering a Fano system in which the quadrupole is not directly forced, the dynamics simplify to

$$\tilde{Q}_{\alpha\beta} = \frac{g_{\alpha\beta}\tilde{F}_{\beta}(\mathbf{x}_{dip},\omega)}{[m_{\alpha\beta}m_{dip}Z_{\alpha\beta}Z_{dip} - g_{\alpha\beta}^2]} = \tilde{x}_{dip,\beta}\frac{g_{\alpha\beta}}{m_{\alpha\beta}Z_{\alpha\beta}}. \tag{3.24}$$

This form allows a similar expression to the dipole-dipole CL for the case of a single quadrupole coupled to a single dipole mode with an additional weighting due to the difference in prefactor for dipolar vs quadrupolar radiation. Ultimately, we obtain

$$\frac{\Gamma_{\mathrm{CL}}^{d-q}(\omega)}{\Gamma_{\mathrm{CL}}^{d}(\omega)} = \left|\frac{m_\beta m_{\alpha\beta} Z_\beta Z_{\alpha\beta}}{[m_\beta m_{\alpha\beta} Z_\beta Z_{\alpha\beta} - g_{\alpha\beta}^2]}\right|^2 \left[1 + \frac{\omega^2}{120c^2}\frac{g_{\alpha\beta}^2}{m_{\alpha\beta}^2|Z_{\alpha\beta}|^2}\right] \tag{3.25}$$

which can be further evaluated using the definitions in Eq. 3.4

$$\frac{\Gamma_{\mathrm{CL}}^{d-q}(\omega)}{\Gamma_{\mathrm{CL}}^{d}(\omega)} = \left|\frac{\epsilon + q_F}{\epsilon + i}\right|^2 \left[1 + \frac{\omega^2}{120c^2}\frac{g_{\alpha\beta}^2}{m_{\alpha\beta}^2|Z_{\alpha\beta}|^2}\right]. \tag{3.26}$$

For the case of a dipole-quadrupole system, some regimes allow for the radiation attributed to the quadrupole to be neglected. This is a safe assumption in most cases as the quadrupole radiates at a significantly lower rate than the dipole and the driving force of the quadrupole

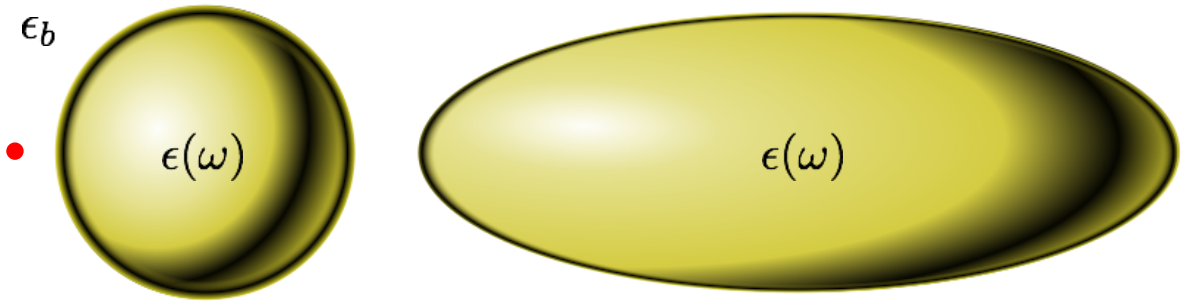

Figure 3.1: Schematic of Au Fano Dimer. The red dot represents the impact parameter of the electron beam which is selected to drive only the nanosphere directly.

is due to the curvature of the dipole field, which rapidly decays as a function of distance. In this regime the term yet again simplifies to

$$\frac{\Gamma_{\mathrm{CL}}^{d-q}(\omega)}{\Gamma_{\mathrm{CL}}^{d}(\omega)} = \left| \frac{\epsilon + q_F}{\epsilon + i} \right|^2 \tag{3.27}$$

which is identical to the form observed by Fano, with the exception of q_F holding complex character. Due to the fact that ϵ is real valued, total destructive interference can not be observed in this system.

3.3 Results and Discussion

This section considers plasmonic dimers studied with the theoretical framework presented in the previous section and with numerical simulations. First, the analytic case of a gold nanosphere coupled to a gold prolate spheroidal nanoparticle where the nanosphere hosts the "bright," dipolar mode and the prolate spheroid hosts the "dark," "quadrupolar" mode. The use of a prolate spheroid is ideal due to tunability of the quadrupole mode along the major axis, energetically isolating it from the remaining quadrupole modes. This allows for a simple analytic treatment of the dimer. This system is schematically displayed in Figure 3.1 including the selection of the impact parameter of the electron which is chosen to directly force the nanosphere's dipole mode.

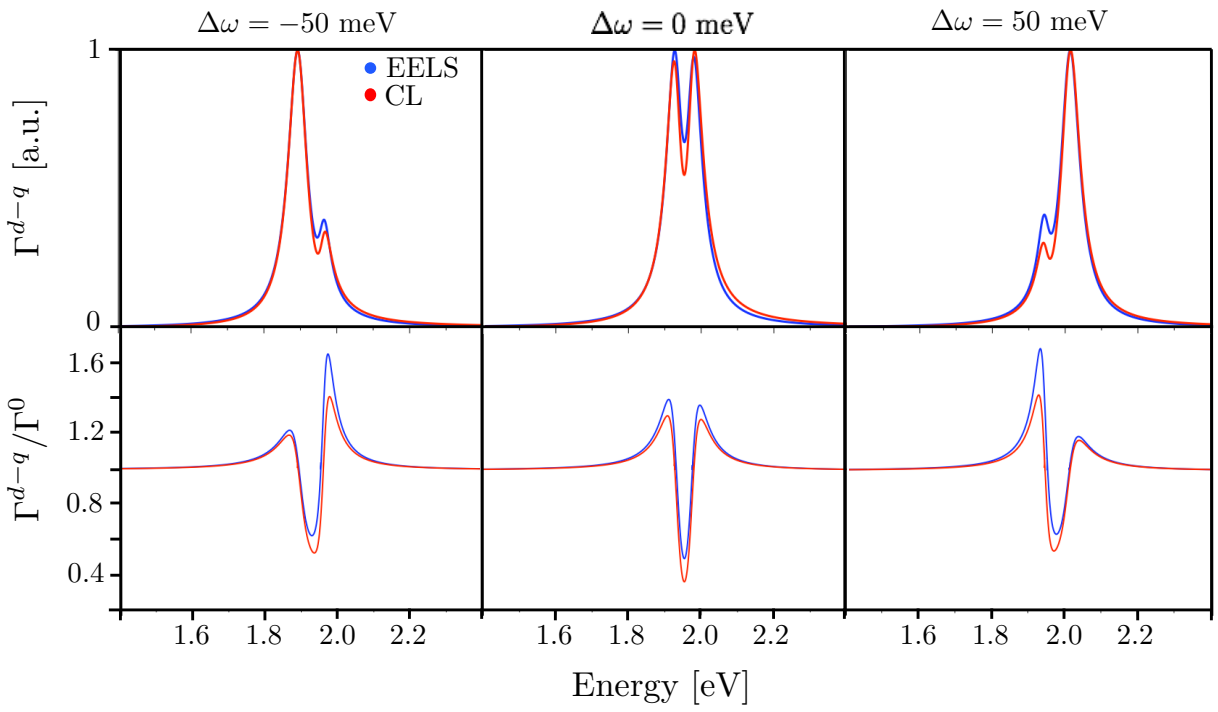

Figure 3.2: Top: Normalized EELS and CL spectra for a nanoparticle dimer. The dimer consists of a nanosphere (r=15 nm) and a prolate spheroid (200 nm x 30 nm) separated by 6 nm. The prolate spheroid has a quadrupole mode along the major axis with a resonance energy of 1.95 eV and the nanosphere has a dipole mode with a resonance energy detuned from the spheroidal mode by -50 meV, 0 meV, and +50 meV. Bottom: EELS and CL spectra normalized by the single nanoparticle dipole spectra. This measure of the Fano line shape demonstrates that a larger amount of interference is observed in CL compared to EELS. The change in phase of the Fano line shape is readily observed in both EELS and CL for the range of detunings.

The current model for EELS and CL neglects retardation effects resulting in a resonance frequency for the sphere that is independent of particle size. The resonance frequency (and the effective mass) of the prolate spheroid takes into account the aspect ratio of the particle resulting in a red-shift of the major axis modes. In order to prevent these modes from becoming too detuned from one another, the resonance frequency of the dipole mode of the sphere is set to arbitrary values near the spheroidal quadrupole mode. This can be justified by adjusting the nanosphere radius, which when accounting for retardation would result in a red-shift for larger radii.

Figure 3.2 displays the EELS and CL spectra for the coupled system with an energetic

detuning of -50 meV, 0 meV, and 50 meV between the dipole and quadrupole mode. Additionally, the Fano line shape is displayed in the bottom portion of the figure where the EELS and CL spectra have been normalized by the uncoupled nanosphere spectrum. Here, a change in phase is observed as the dipole mode changes in detuning from red of the quadrupole mode to blue of the quadrupole mode. The difference in the magnitude of the interference in the EEL and CL observables is consistent at all detuning values with CL exhibiting more interference than EELS.

It is important to reiterate that the analytic model derived for this example was in the quasistatic limit which is only valid for the case of small particles. The resonance frequency of the nanosphere dipole was artificially altered to allow for an adequate coupling which physically requires retardation effects to be included. While the approximations in this model may break down with increasing particle size affecting resonance energies and line widths, the intuition that is gained regarding the underlying physics of this dimer system can be applied for "real" systems in the retarded limit.

We move to numerical simulations allowing for a more complete treatment of nanoparticle dimers that includes retardation effects. Interactions beyond those of dipole-quadrupole are considered for these systems, however, the underlying principles still hold for these higher order interactions. Additionally, the geometry of the following dimers differs from the analytic case. The dimer is composed of a large gold nanodisk coupled to long nanorod. These "lollipop" systems explore a robust range of nanoparticle sizes, demonstrating that Fano interferences are capable of being experimentally measured with EELS and CL in a single metal dimer system. All simulations were performed using MNPBEM [61] using dielectric data from Johnson and Christy [73].

The first lollipop system consist of a gold disk (height of 30 nm and diameter of 245 nm) and a nanorod (length of 420 nm and diameter of 35 nm) separated by a junction of 25 nm as displayed in figure 3.3D. The disk plays the role of the bright mode/continuum while the nanorod holds various dark modes/discrete states. Two of these dark modes of the nanorod spectrally overlap with the dipole mode of the nanodisk, as shown in EEL spectrum in figure

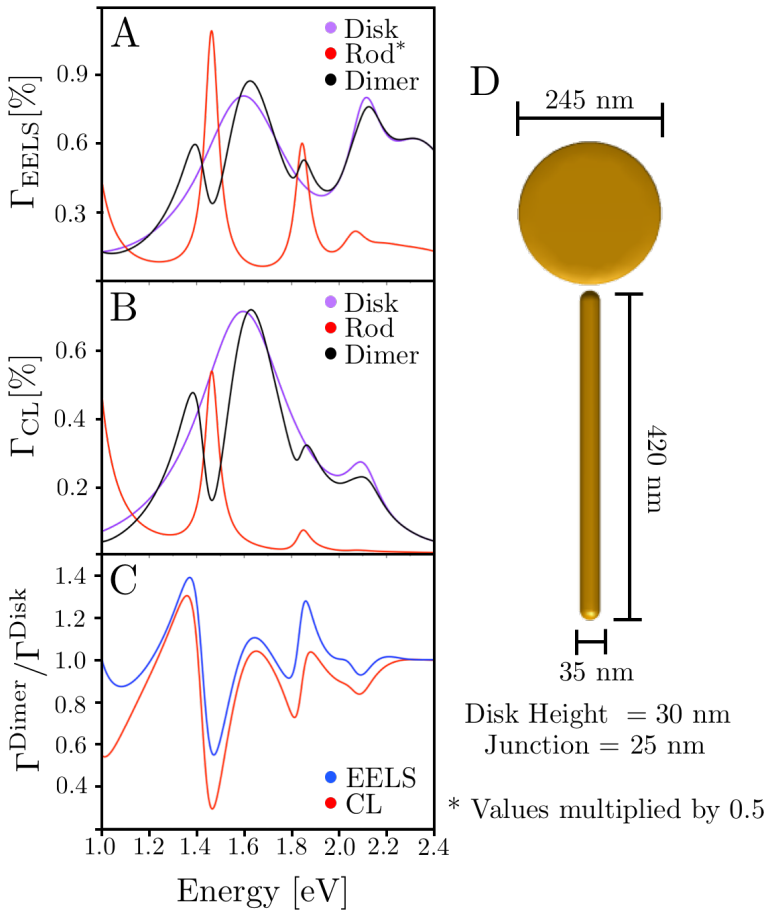

Figure 3.3: EEL Spectra (A) and CL (B) for the Au nanodisk (purple), Au nanorod (red), and dimer (black). The overlap between the dipole mode of the nanodisk and higher order modes of the nanorod are clearly displayed. C: Fano factor for EELS and CL. D: Schematic of system under interrogation. The electron beam is placed external to the disk on the side opposite of the nanorod.

3.3A. This overlap allows for the modes to appreciably couple and the resulting EEL and CL spectra display a line shape with multiple asymmetries.

Of the two dark modes coupling to the nanodisk's dipole, one is red of the dipole resonance and the other blue. This results in an asymmetric line shape with the opposite phase which is particularly noticeable when considering the Fano factor in panel C. Here the dimer EEL and CL spectra are normalized by the respective nanodisk spectra. Similar to the results obtained from the quasistatic analytic model, CL for the lollipop system exhibits a stronger interference than EELS which can be seen in the sharper dips in the CL Fano factor.

The second lollipop system is similar in nature to the first, with a slightly larger diameter (246 nm) nanodisk and a nanorod that is considerably longer (720 nm) and slightly wider (40 nm) as shown in figure 3.4. The change in the nanorod results in a more polarizable particle, where all of the modes are red shifted compared to the previous nanorod. This results in higher order modes coupling to the dipole of the nanodisk than the first lollipop dimer. The asymmetries observed in EELS and CL are qualitatively similar to the smaller lollipop system, demonstrating the robust nature of this interaction. However, in the larger lollipop system, the asymmetries observed in EELS and CL are sharper than the smaller system. This character is once again prominent in the Fano Factor for both EELS and CL, where the both factors dip nearly to zero.

3.4 Conclusions

A simple quasistatic model has been developed to describe Fano interferences in nanoparticle dimers, a phenomenon once thought to be unobservable by the electron [88], by selection of electron beam location. The Fano factor for EELS is identical to that found in optical absorption [148] with the definition of "bright" and "dark" holding a different, more flexible definition for electron excitations. The asymmetric line shape that arises due to Fano interferences from the analytic model is shown to exist in systems that include retardation effects through numerical simulations. The robust nature of this phenomenon is shown in two single-metal "lollipop" dimers.

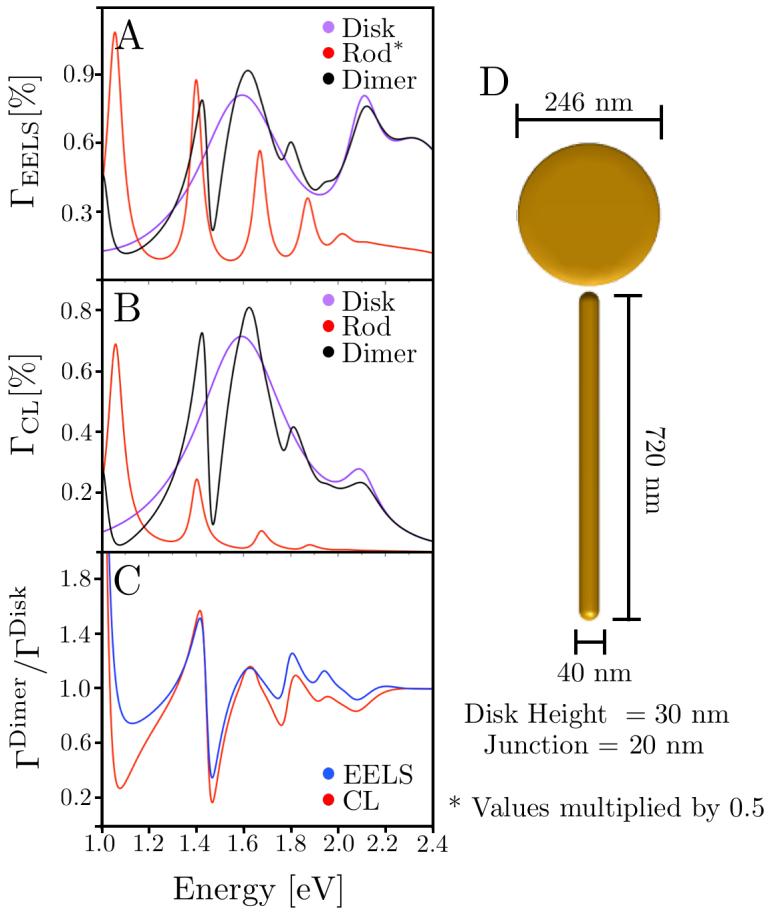

Figure 3.4: EEL Spectra (A) and CL (B) for the Au nanodisk (purple), Au nanorod (red), and dimer (black). The overlap between the dipole mode of the nanodisk and higher order modes of the nanorod are clearly displayed. C: Fano factor for EELS and CL. D: Schematic of system under interrogation. The electron beam is placed external to the disk on the side opposite of the nanorod.

In addition to EELS, the characteristic asymmetric line shape of a Fano interference emerges in the far-field measurement of CL, which is the electron-drive analog to optical scattering. The interferences observed in CL are shown in the analytic model to exhibit a higher degree of interference than in EELS, a result that is confirmed by full-wave numerical simulations. These results demonstrate the ability of electron based spectroscopies to measure a broader class of Fano interferences in comparison to conventional optical spectroscopies.

Chapter 4

IMAGING PLASMON HYBRIDIZATION IN METAL NANOPARTICLE AGGREGATES WITH ELECTRON ENERGY-LOSS SPECTROSCOPY

S.C. Quillin, C. Cherqui, N.P. Montoni, G. Li, J.P. Camden

The Journal of Physical Chemistry C, **2016**, 120 (37), pp 20852-20859

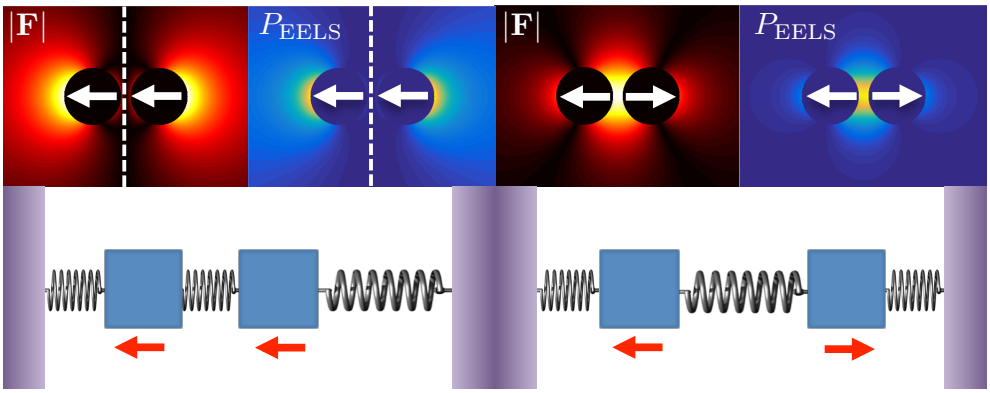

Figure 4.1: Abstract Figure

4.1 Abstract

Recent interest has been placed on understanding the behavior of plasmon-supporting metal nanoparticles in complicated aggregates. Because of its high spatial and spectral resolution, a powerful tool for this pursuit is electron energy loss spectroscopy (EELS) in a scanning tunneling electron microscope (STEM). EELS is useful because it yields information on both the spectral distribution of plasmon modes and the spatial distribution of energy around

the nanoparticle. Here we show that EELS tracks the force between a STEM electron and a plasmon through the use of an oscillator model. We demonstrate the emergence of nodal structure in EELS maps for hybridized systems in the context of this model and confirm this behavior with experiment and simulations. This characteristic of hybridized systems allows us to put forth a rubric for determining the relative phase of dipole plasmons. Further, we explain how asymmetries and spatially co-located degeneracies in nanoparticle aggregates impact EELS maps.

4.2 Introduction

Optical-frequency electromagnetic fields penetrate metal surfaces on the order of tens of nanometers as determined by the skin depth [80]. Metal nanoparticles are unique in that applied fields can penetrate them entirely, facilitating the efficiency of their coupling to the radiation field. The largest amplitude optical excitations in metal nanoparticles are due to the collective displacements of their conduction-band electrons known as localized surface plasmon resonances (LSPRs). LSPRs have a number of interesting and unexpected optical properties, such as the ability to focus light below the diffraction limit. Such is useful in a variety of applications, including solar energy conversion [94, 141], catalysis [108, 90], enhanced molecular spectroscopy [44, 71, 3, 111, 78], and nanoscale heating [12, 2].

The specific characteristics of LSPRs are determined both by the composition and morphology of the nanostructure. They are labeled bright if they efficiently couple to the radiation field and dark if they do not. A variety of near-field optical methods have been used to probe the plasmonic properties of nanoparticles but the spatial resolution of these methods is on the order of tens of nanometers [16, 55], limiting their effectiveness. In contrast, electron energy-loss spectroscopy (EELS) in a scanning transmission electron microscope (STEM) has emerged as one of the leading techniques used in characterizing the plasmonic properties of individual and aggregate systems of nanoparticles, due in part to the few-nanometer-scale spatial resolution readily achieved in practice.

The observables produced by STEM/EELS are dependent upon: i) the spectral behavior

of the STEM electron, which provides a near-continuum source of light with which to excite LSPR modes, and ii) the location of the beam relative to the target. Fixing the beam position produces an EEL probability spectrum over all possible loss energies from 0 eV (no loss) up to the kinetic energy of the STEM electron (typically ∼100 keV), while filtering a set of EEL spectra acquired at many beam positions at a specific loss-energy value produces an energy-filtered EEL map. The latter shows those regions in space where it is more or less probable for the STEM electron to lose energy and can be used to infer detailed information about the nanoscopic spatial profile of the particular LSPR excited at that loss-energy value.

In this paper we review a procedure for mapping LSPRs onto a collection of coupled mechanical oscillators and, within this context, derive an exact expression for the EEL probability in hybridized nanoparticle systems. We then use this expression to develop a rubric for determining the relative phases between the monomer LSPRs within a hybridized multiparticle assembly. For clarity and simplicity, our analysis is restricted to the dipole LSPR on each particle; however, extension to higher-order LSPRs is straighforward from model presented. The analytical results are validated by both EELS simulations and experiment on equivalent nanoparticle systems.

4.3 Oscillator Model of LSPRs

In 1978, Lucas and co-workers [9, 30] established a method for mapping the dipole response of a set of interacting spherical nanoparticles onto a set of fictituous coupled mechanical oscillators with an effective mass $m = e^2/\alpha_{\rm sp}\omega_{\rm sp}^2$. Here, $\alpha_{\rm sp} = 3a^3/(\epsilon_\infty + 2)$, a is the sphere radius, $\omega_{\rm sp}$ is the dipole LSPR frequency, and ε_∞ is the static dielectric response of the metal's core electrons; for simplicity, the background environment is chosen to be vacuum. The plasmon's effective mass is inversely proportional to the nanoparticle's volume and is a measure of its polarizability: the smaller the mass the more polarizable, the larger the mass the less polarizable.

Within the quasi-static limit, an assembly of coupled plasmonic nanoparticles located at

positions $\mathbf{r}_i$ and driven by the force $\mathbf{F}(\mathbf{r}_i, t)$ can be described by the effective Hamiltonian,

$$H = \sum_{i=1}^{N} \frac{\mathbf{P}_i^2}{2m_i} + \frac{1}{2} m_i \omega_i^2 \mathbf{Q}_i^2 - \sum_{i \neq j} \frac{e^2}{2} \mathbf{Q}_i \cdot \mathbf{\Lambda}_{ij}^{\mathrm{NF}} \cdot \mathbf{Q}_j - \sum_{i=1}^{N} \mathbf{F}(\mathbf{r}_i, t) \cdot \mathbf{Q}_i, \tag{4.1}$$

where $\mathbf{Q}_i = \hat{\mathbf{n}}_i Q_i$ and $\mathbf{P}_i = \hat{\mathbf{n}}_i P_i$ represent the displacement coordinate and conjugate momentum, m_i the effective mass, and ω_i the resonance frequency of the ith dipole plasmon. LSPRs interact with each other pairwise via the near-field dipole-dipole coupling tensor $\mathbf{\Lambda}_{ij}^{\mathrm{NF}} = (3\hat{\mathbf{n}}_i\hat{\mathbf{n}}_j - 1_{ij})/|\mathbf{r}_i - \mathbf{r}_j|^3$. The first two terms in Eq. 1 represent the internal energy of the LSPR, the third term accounts for the interparticle coupling, and the fourth term accounts for the application of an external force. From Eq. 1 a set of coupled equations of motion can be determined.

Before moving on to examining the dynamics of coupled LSPRs, we first examine the dynamics of a single particle by setting $N = 1$ in Eq. 1. This yields

$$\ddot{\mathbf{Q}} + \gamma \dot{\mathbf{Q}} + \omega_{\mathrm{sp}}^2 \mathbf{Q} = \frac{\mathbf{F}(t)}{m}, \tag{4.2}$$

where an empirical friction term proportional to $\dot{\mathbf{Q}}$ has been added with damping rate γ to account for losses intrinsic to the metal. The formal solution is

$$\begin{aligned} \mathbf{Q}(t) &= \int_{-\infty}^{t} \mathrm{d}t' \frac{\mathrm{e}^{-\gamma(t-t')/2}}{\sqrt{\omega_{\mathrm{sp}}^2 - (\gamma/2)^2}} \sin\left[\sqrt{\omega_{\mathrm{sp}}^2 - (\gamma/2)^2}(t-t')\right] \frac{\mathbf{F}(t')}{m} \\ &= \int_{-\infty}^{t} \mathrm{d}t' g(t-t') \frac{\mathbf{F}(t')}{m}, \end{aligned} \tag{4.3}$$

where $g(t - t')$ is the causal harmonic oscillator Green function. Its Fourier transform is proportional to the polarizability of the sphere via $\mathrm{Im}\{g(\omega)\} = (4\pi/a^3\omega_{\mathrm{sp}}^2)\mathrm{Im}\{\alpha(\omega)\}$.

Light Excitation: The time evolution of a sphere's dipole plasmon under the influence of a plane wave light field of force $\mathbf{F}(t) = -e\mathbf{E}_0 \cos(\omega t)$ is

$$\mathbf{Q}(t) = \frac{-e\mathbf{E}_0 \cos(\omega t - \delta)}{m\sqrt{(\omega_{\mathrm{sp}}^2 - \omega^2)^2 + (\gamma\omega)^2}}, \tag{4.4}$$

where $\delta = \tan^{-1}(\omega\gamma/[\omega_{\mathrm{sp}}^2 - \omega^2])$ determines the relative phase between the force and the plasmon. From this expression it is clear that the dynamics of the plasmon are determined

by the applied force. However, the amplitude of its dynamics is determined by whether or not the force is resonant with the LSPR frequency.

The optical absorption can be calculated by considering the average power absorbed by a plasmon over the cycle of oscillation of the driving field,

$$\begin{aligned}\langle P_{\text{abs}}(t)\rangle_T &= \frac{1}{T}\int_{-T/2}^{T/2} \mathrm{d}t\ \mathbf{F}(t)\cdot\dot{\mathbf{Q}}(t) \\ &= \sigma_{\text{abs}}(\omega)I,\end{aligned} \tag{4.5}$$

where σ_{abs} is the absorption cross section and I is the intensity of the light source. The cross section has the form

$$\sigma_{\text{abs}}(\omega) = \frac{4\pi\omega}{c}\text{Im}\{\alpha(\omega)\} \tag{4.6}$$

and is a function of frequency alone, as the spatial dependence encoded in the force is lost due to the delocalized nature of the plane wave at the nanoscale.

STEM Electron-Beam Excitation: The force excerted by a uniformly moving relativistic electron within a STEM is dictated by the evanescent field

$$\mathbf{E}_{\text{el}}(\mathbf{r},t) = \frac{-e(\mathbf{R}+\mathbf{z}-\mathbf{v}t)}{\gamma_L^2[(z-vt)^2+(R/\gamma_L)^2]^{3/2}}. \tag{4.7}$$

that it carries. In this expression $\mathbf{v} = v\hat{\mathbf{z}}$ is the electron's velocity, γ_L is the Lorentz contraction factor, R is the distance in the impact plane from the plasmonic dipole to the electron beam. The EEL probability is related to the absorbed power in the following manner,

$$\langle P_{\text{abs}}(t)\rangle_T = \frac{1}{T}\int_{-\infty}^{\infty}\mathrm{d}tP_{\text{abs}}(t) = \frac{1}{T}\int_0^{\infty}\mathrm{d}\omega\hbar\omega\Gamma_{\text{EELS}}(\omega), \tag{4.8}$$

where Γ_{EELS} is a distribution function describing the probability per unit of transferred frequency for the electron to lose energy to the target and decelerate [46]. Γ_{EELS} is expressable in terms of the Fourier transform of the electron's electric field

$$\mathbf{E}_{\text{el}}(\mathbf{r},\omega) = \frac{2e\omega}{v^2\gamma_L^2}\left[iK_0\left(\frac{\omega R}{v\gamma_L}\right)\hat{\mathbf{z}} - \gamma_L K_1\left(\frac{\omega R}{v\gamma_L}\right)\hat{\mathbf{R}}\right]e^{i\omega z/v} \tag{4.9}$$

where K_0 and K_1 are modified Bessel functions of the second kind. All together

$$\begin{aligned}\Gamma_{\text{EELS}}(\omega) &= \frac{\mathbf{F}(\mathbf{R},\omega)\cdot\mathbf{F}(\mathbf{R},-\omega)}{e^2\hbar\pi}\ \text{Im}\{\alpha(\omega)\} \\ &= \frac{4e^2\omega^2}{\hbar\pi v^4\gamma_L^2}\left[K_1^2\left(\frac{\omega R}{v\gamma_L}\right)+\frac{1}{\gamma_L^2}K_0^2\left(\frac{\omega R}{v\gamma_L}\right)\right]\text{Im}\{\alpha(\omega)\}.\end{aligned} \tag{4.10}$$

Comparing the expressions for Γ_{EELS} to σ_{abs} in the case of plane wave excitation, we see that σ_{abs} depends on a single parameter, the frequency of the incoming light, while Γ_{EELS} depends on three: frequency (corresponding to the energy loss), velocity, and beam location. The velocity of the electron is determined by the technical specifications of the STEM and can be considered a fixed parameter, typically about half the speed of light. At a fixed beam position, Γ_{EELS} is a function of frequency alone, and Eq. 10 gives the probability that an electron will lose one quantum of energy to the LSPR, which, due to the resonance structure of $\alpha(\omega)$, peaks at the LSPR frequency. Filtering a set of EEL spectra acquired over a region of interest at a specific loss energy value produces an EEL map, which will be important in the following in determining plasmon hybridization in nanoparticle assemblies. Note that the loss probability is proportional to the magnitude of the force exerted by the electron on the plasmon or, via Newton's second law, the self-induced backforce exerted by the plasmon on the electron. Quantization of H is straighforward and can be used to compute the EEL probabilities for higher quanta losses [30].

Both ways of visualizing EELS data are displayed in Figure 1 for the case of a 30 nm diameter silver sphere in vacuum. Figure 1A shows the EEL spectrum corresponding to a 5 nm impact parameter outside of the particle, based upon the model (dashed) and Mie theory [61] (solid) for both the dipole and higher-order multipolar plasmons; dielectric data for silver is taken from Ref. [73]. The low energy peak (shaded in red) is due to the excitation of the dipole LSPR, while the high-energy shoulder is attributed to a collection of higher-order multipoles. EELS maps are displayed in Figures 1B, 1C, and 1E. Figures 1B and 1C show contour plots of the magnitude of the force felt by the electron and P_{EELS}, as determined from the Hamiltonian model, at the resonant frequency of the plasmon. Both are displayed in the plane perpendicular to the trajectory of the electron, called the impact plane. Figure 1E shows the experimentally measured EEL probability map for a silver sphere of 165 nm diameter (TEM image shown in Figure 1D), which has the same qualitative features. Because of the spherical symmetry of the nanoparticle, the induced dipole moment tracks the position of the electron beam, leading to a ring of equal EEL probability around its perimeter. The

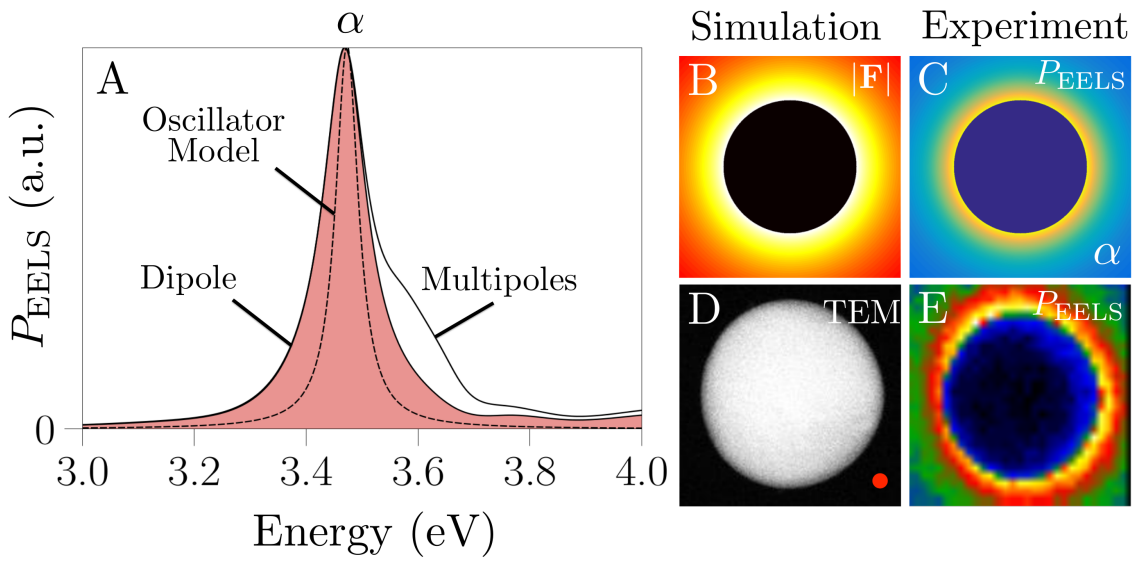

Figure 4.2: **A:** EEL spectrum determined using Mie theory for a single silver nanosphere with a 30 nm diameter and the electron beam placed 5 nm from the surface of the sphere, indicated by the rod dot. The low energy peak, red, corresponds to the dipole plasmon while the high energy shoulder is a result of higher order, multipolar modes. The peak represented by the dashed line is the result from the oscillator model. **B:** Forcing map corresponding to the dipole mode from the oscillator model. The ring of equal forcing is a result of the spherical symmetry of the system. **C:** EELS maps corresponding to the dipole mode. The ring of equal EEL probability is due to the particle's symmetry. **D:** TEM image of the experimentally measured sphere. **E:** EELS maps for the dipole mode of an experimentally measured silver sphere of 165 nm. This holds the same qualitative properties as the map created using the oscillator model as it contains rings of equal EEL probability.

EEL probability drops to zero towards the center of the sphere because there the STEM electron polarizes the conduction electrons radially, which is incompatible with the dipole LSPR. This demonstrates the connection between the force applied on the electron due to the plasmon and the EEL probability.

4.4 Sphere Dimers

The behavior of nanoparticle aggregates becomes more complicated as a result of hybridization of individual LSPRs into collective modes. In contrast to a single sphere, the addition of a second spherical particle breaks the radial symmetry in the impact plane. To model the hybridization of two dipole LSPRs, we consider the Hamiltonian in Eq. 1 for $N = 2$. Ignoring the forcing for the moment, the sub-system of two coupled LSPRs can be diagonalized by introducing normal mode coordinates $\mathbf{Q}_\pm = \sum_\lambda \hat{\mathbf{n}}_\pm^\lambda Q_\pm^\lambda$ with amplitudes

$$\begin{aligned} Q_+^\lambda &= \cos\theta_\lambda Q_1^\lambda + \sin\theta_\lambda Q_2^\lambda \\ Q_-^\lambda &= -\sin\theta_\lambda Q_1^\lambda + \cos\theta_\lambda Q_2^\lambda, \end{aligned} \tag{4.11}$$

where $\lambda = x, y, z$ indicates directionality in space and $\theta_\lambda = (1/2)\tan^{-1}(2g_{12}^\lambda/\mu[\omega_1^2 - \omega_2^2])$ is the decoupling or mixing angle [147]. Here $\mu = \sqrt{m_1 m_2}$ is the geometric average of the effective masses of the particles and $g_{12}^\lambda = e^2 \hat{\mathbf{n}}_1^\lambda \cdot \mathbf{\Lambda}_{12}^{\mathrm{NF}} \cdot \hat{\mathbf{n}}_2^\lambda$ is the interparticle coupling strength, where $\hat{\mathbf{n}}_i^\lambda$ is the projection of the direction of the ith LSPR onto the direction λ. For the sake of generality, the LSPR effective masses and resonant frequencies are chosen to be different. The subscripts $+$ and $-$ refer to the in-phase and out-of-phase hybridized plasmon modes respectively. There are analogous expressions for the conjugate momenta P_+^λ and P_-^λ. Applying the coordinate transformation of Eq. 11 yields

$$H_0 = \frac{\mathbf{P}_+^2}{2\mu} + \frac{1}{2}\mu\omega_+^2\mathbf{Q}_+^2 + \frac{\mathbf{P}_-^2}{2\mu} + \frac{1}{2}\mu\omega_-^2\mathbf{Q}_-^2, \tag{4.12}$$

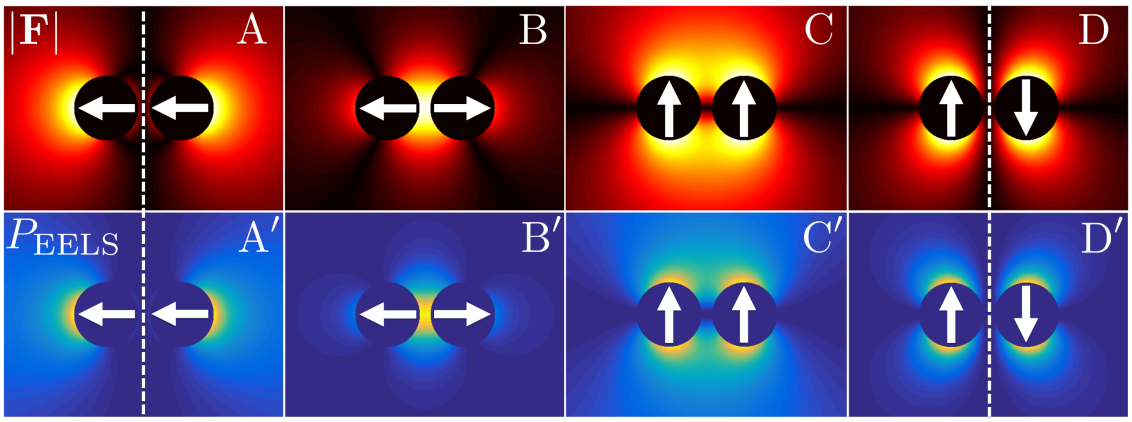

Figure 4.3: **A-D:** Forcing maps displaying the forcing of the collinear (A), anti-collinear (B), parallel (C), and anti-parallel (D) modes for two identical particles. Each point in space corresponds to the force exerted by the electron beam located at that position. A nodal line appears between the two particles equidistant from the surface, displaying zero net force, on the collinear and anti-parallel modes. This location of zero forcing translates directly into nodal structure in the EELS maps. **A′-D′** EELS maps for the collinear (A′), anti-collinear (B′), parallel (C′), and anti-parallel (D′) modes obtained through the Hamiltonian model describing the hybridized dimer system. Nodal structure appears for the collinear and anti-parallel modes co-located with the zero forcing node shown in A and D.

where the resonant frequencies for the hybridized modes are

$$\begin{aligned}\omega_+^\lambda &= \sqrt{\omega_1^2\cos^2\theta_\lambda + \omega_2^2\sin^2\theta_\lambda - \frac{2g_{12}^\lambda}{\mu}\cos\theta_\lambda\sin\theta_\lambda} \\ \omega_-^\lambda &= \sqrt{\omega_1^2\sin^2\theta_\lambda + \omega_2^2\cos^2\theta_\lambda + \frac{2g_{12}^\lambda}{\mu}\cos\theta_\lambda\sin\theta_\lambda}.\end{aligned} \tag{4.13}$$

The new normal modes can be aligned along the axis of displacement resulting in an in-phase, collinear mode and an out-of-phase, anti-collinear mode or they can be aligned perpendicular to the axis of displacement resulting in an in-phase, parallel mode and an out-of-phase, anti-parallel mode in the impact plane. An additional pair of degenerate parallel and anti-parallel modes are oriented normal to the impact plane but will not be discussed as they are weakly excited due to the form of the eletron's electric field in that direction.

In the basis of normal modes the interaction between the electron and the LSPRs becomes

$$\begin{aligned} H_{\text{ext}} &= -\sum_{\lambda}(-e)\left[\cos\theta_\lambda\left(\frac{m_2}{m_1}\right)^{1/4}E_\lambda(\mathbf{r}_1,t)+\sin\theta_\lambda\left(\frac{m_1}{m_2}\right)^{1/4}E_\lambda(\mathbf{r}_2,t)\right]Q_+^\lambda \\ &\quad+(-e)\left[-\sin\theta_\lambda\left(\frac{m_2}{m_1}\right)^{1/4}E_\lambda(\mathbf{r}_1,t)+\cos\theta_\lambda\left(\frac{m_1}{m_2}\right)^{1/4}E_\lambda(\mathbf{r}_2,t)\right]Q_-^\lambda \\ &= -[\mathbf{F}_+(t)\cdot\mathbf{Q}_+ + \mathbf{F}_-(t)\cdot\mathbf{Q}_-], \end{aligned} \tag{4.14}$$

where the new mixed forces $\mathbf{F}_+$ and $\mathbf{F}_-$, which arise from the fact that normal mode coordinates are linear combinations of the uncoupled coordinates, are implicitly defined. In analogy to the previous section, the associated Γ_{EELS} for the hybridized system is

$$\Gamma_{\text{EELS}}(\omega)=\sum_{\lambda}\frac{F_+^\lambda(\omega)F_+^\lambda(-\omega)}{e^2\hbar\pi}\,\text{Im}\{\alpha_+^\lambda(\omega)\}+\frac{F_-^\lambda(\omega)F_-^\lambda(-\omega)}{e^2\hbar\pi}\,\text{Im}\{\alpha_-^\lambda(\omega)\}, \tag{4.15}$$

where $\alpha_+^\lambda(\omega)$ and $\alpha_-^\lambda(\omega)$ are the effective polarizabilities of the normal modes oriented in the λ direction. From Eq. 14 it is evident that $\mathbf{F}_+$ and $\mathbf{F}_-$ are superpositions of the forces acting on the individual uncoupled LSPRs, now weighted by factors proportional to the effective mass and mixing angle. For identical particles these simplify to $F_+^\lambda=-e(E_\lambda(\mathbf{r}_1,\omega)+E_\lambda(\mathbf{r}_2,\omega))/\sqrt{2}$ and $F_-^\lambda=-e(-E_\lambda(\mathbf{r}_1,\omega)+E_\lambda(\mathbf{r}_2,\omega))/\sqrt{2}$, resulting in a net zero force when $E_\lambda(\mathbf{r}_1,\omega)=-E_\lambda(\mathbf{r}_2,\omega)$ for F_+^λ and $E_\lambda(\mathbf{r}_1,\omega)=E_\lambda(\mathbf{r}_2,\omega)$ for F_-^λ. Interestingly, when the electric field is due to a plane wave, each nanoparticle experiences the same spatially constant force, enforcing $E_\lambda(\mathbf{r}_1,\omega)=E_\lambda(\mathbf{r}_2,\omega)$. This is in contrast to the electric field of a STEM electron, which has a high degree of spatial variation on the nanoscale, such that every point in space experiences a different force. This means that the electron beam imposes different selection rules depending upon its location in the impact plane. For example, it is impossible to drive the in-phase mode from the center of the dimer junction.

Sphere Homodimer: This concept is further explored in Figure 2, where both force and EELS maps are depicted for the four hybridized modes of interest of the sphere homodimer based upon the above Hamiltonian model. Nodes are spatially co-located in both the forcing and EELS maps for the in-phase, collinear and the out-of-phase, anti-parallel modes of the

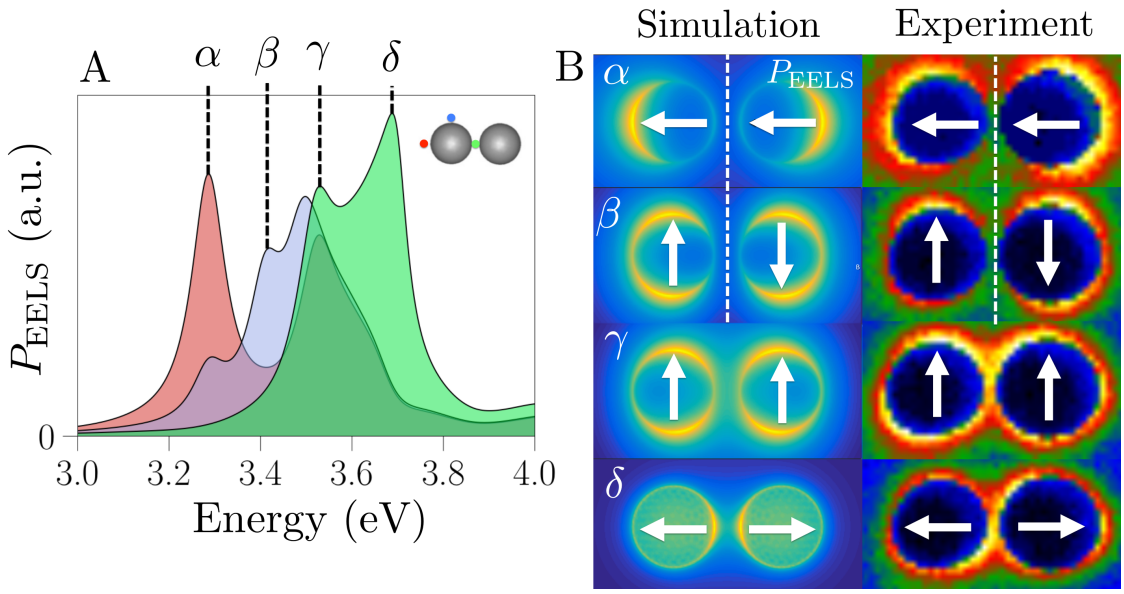

Figure 4.4: **A:** Simulated EEL spectra for a dimer of identical spherical nanoparticles with a diameter of 30 nm and a separation distance of 5 nm. The EEL spectra result from three impact parameters for the electron beam, corresponding to the colored dots on the inset. **B:** EELS maps for the hybridized dipole modes of the simulated and representative experimentally measured dimer systems. The collinear mode, α, and the anti-parallel mode, β, display nodal structure in the junction for both simulated and experimentally measured EELS maps. The parallel mode, γ, and the anti-collinear mode, δ, do not contain nodal structure.

system. The node bisecting the junction of the dimer is a result of the force on the mode netting zero, leaving the mode undriven for impact parameters along this line.

Experimental validation of the presented dimer model can be found in Figure 3 together with MNPBEM simulations. While the experimental data is taken from a pair of spherical particles each of 165 nm diameter, the qualitative nature of the modes does not change from those considered in the model. A high degree of correlation is evident between the model, simulation, and experiment. In order to observe all four relevant hybridized modes, three impact parameters are considered for the simulated EEL spectra shown in Figure 3A. The first beam location, labeled by the red bullet, is oriented along the axis of displacement of the two spheres on the exterior side and excites two of the dimer modes: mode α and mode γ. The second beam location, labeled by the blue bullet, is oriented to the side of one of the spheres in the dimer, off of the axis of displacement, and excites three modes: mode α, mode β, and mode γ. The final beam position, labeled by the green bullet, is oriented directly between and equidistant from the two spheres and excites two modes: mode γ and mode δ.

Each hybridized mode in this system can be identified by considering the nodal structure observed in the EELS maps and areas of higher EEL probability. Two modes, α and β, contain nodal structure in the junction, a feature that only occurs for the collinear and anti-parallel modes. Mode α shows regions of higher EEL probability near the exterior of the spheres along the axis of displacement. Mode β shows regions of higher EEL probability along the sides of the nanospheres off of the axis of displacement. The two modes lacking nodal structure, γ and δ, can likewise be identified by observing the location of higher EEL probability, as they must either be anti-collinear or parallel modes. Mode γ displays higher EEL probability along the sides of the nanospheres off of the axis of displacement identifying it as the parallel mode. Mode δ displays higher EEL probability in the junction around the axis of displacement identifying it as the anti-collinear mode. Based upon this nodal structure, the four hybridized modes of the sphere dimer can be identified and categorized. Extending these ideas, the effects of asymmetry in the dimer system may now be analyzed.

Sphere Heterodimer: Further examination of the forcing term described by Eq. 14

shows that in addition to the spectral and spatial behavior of the field of the electron beam, parameters inherent to the dimer, such as effective mass, resonance frequency, and interparticle coupling act as weighting factors for the force applied on each nanosphere, thereby affecting Γ_{EELS}. In this section, the effect of breaking the symmetry of the dimer is examined in two ways: i) demanding that both LSPR frequencies are the same, i.e., $\omega_1 = \omega_2$, while varying the effective mass of one particle, and ii) varying the LSPR frequency of one particle while fixing their effective masses to be the same, i.e., $m_1 = m_2$.

These cases are explored in Figure 4 for the parallel and anti-parallel modes (upper panels) and the collinear and anti-collinear modes (lower panels). The central column corresponds to a system of identical nanoparticles ($m_1 = m_2$ and $\omega_1 = \omega_2$). Moving right from this column displays the effects of increasing the effective mass of the left particle, leading to localization of the EEL probability on the particle with a lower effective mass, regardless of which mode is excited. This effect is a consequence of the fact that the particle with the lower effective mass has a higher polarizability, leading to a stronger induced electric field than the particle of effective greater mass.

How the system behaves for equal effective masses but different resonance frequencies is explored by moving left from the center column. This also leads to localization but for a different reason. This localization is entirely due to the mixing of modes and is instead a signature of Fano-like interferences[54, 42, 17]. This can be verified by building EELS maps for each set of ω_+ and ω_- modes and looking for a flip in plasmon localization. This is in contrast to the case of degenerate plasmom resonances and differing effective masses which is entirely determined by the polarizability of each individual nanoparticle and therefore shows no change in localization.

4.5 Nanorod Systems

As polarizability depends on the geometry of a nanoparticle, and the effective mass depends on the polarizability, introducing anisotropy into the geometry of a nanoparticle will change the effective masses of the LSPRs. Such is the case for the nanorod[110, 53, 18]. Along its

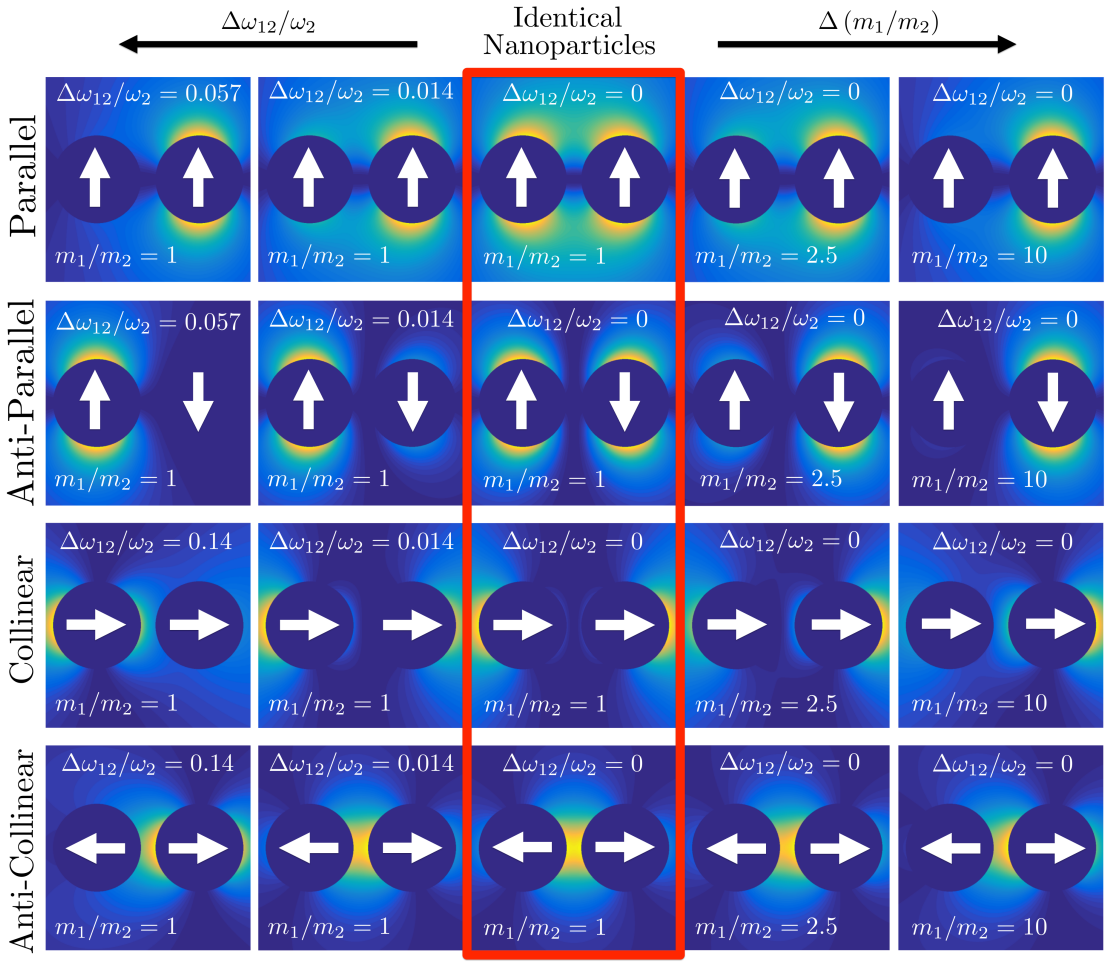

Figure 4.5: EELS maps representing the effect of changing the effective mass or resonance frequency for one particle in the dimer for the parallel, anti-parallel, collinear and anti-collinear modes. The central panels, outlined in red, represent identical particles, while panels to the left of this are the result of detuning the resonance by lowering the left particle's resonance frequency, and panels to the right are the result of changing the effective mass ratio by increasing the effective mass of the left particle. Localization is observed in both modes with the introduction of heterogeneity, but localize on the same particles for varying of effective mass and separate particles for altering the resonance frequency.

longitudinal axis, the nanorod is more polarizable and has a smaller effective mass, while along its short axes it is less polarizable and has a larger effective mass. Depending upon its aspect ratio, the longitudinal and transverse plasmons can be energetically split to not overlap, with the longitudinal plasmon lying lower in energy than the transverse. For these reasons EEL maps of nanospheres and nanorods show a stark difference. While the nanosphere has circular rings of equal probability in its EEL maps, the nanorod has lobes of high EEL probability at its tips and a node at its center.

Aligning two rods along their longitudinal axes results in a system with hybridized plasmon modes analogous to the collinear modes of the sphere dimer and exhibits the same nodal structure or lack thereof. Conversely, separating the two rods in parallel results in hybridized plasmon modes analogous to the parallel modes of the sphere dimer. While the presented Hamiltonian model can be extended to descibe prolate spheroids which approximate the nanorod, we have chosen only to interpret simulations based upon the MNPBEM method, the results of which are displayed in Figure 5.

Rod Trimers: Rod systems become more interesting when a third rod is added. By arranging the rods in the appropriate geometry, it is evident that EELS maps not only measure relative phase, but also show signatures of the excitation of degenerate modes. Two rod trimers are considered in the following: one in which the rods are arranged in a zig-zag pattern and one where they are arranged on the sides of a triangle.

Figure 6 displays the case of three rods arranged in a zig-zag pattern. Figure 6A shows the EEL spectrum for such a trimer, and has three distinct peaks. Figure 6B shows the EEL maps corresponding to each peak. Mode α displays nodes in the junctions that extend towards the middle of the outer particles, signifying that it is the net dipole mode. In mode β, rather than seeing nodal structure resulting from pairs of collinear dipoles, the EEL probability is more localized to the outer particles in both junctions. This is because the peak in the spectrum corresponds to two possible orientations of the dipole plasmon on the central particle. Because both are equally polarizable, the EEL map encodes the superposition of these two modes. Mode γ does not contain nodal structure or asymmetry in the EEL probability, and is the

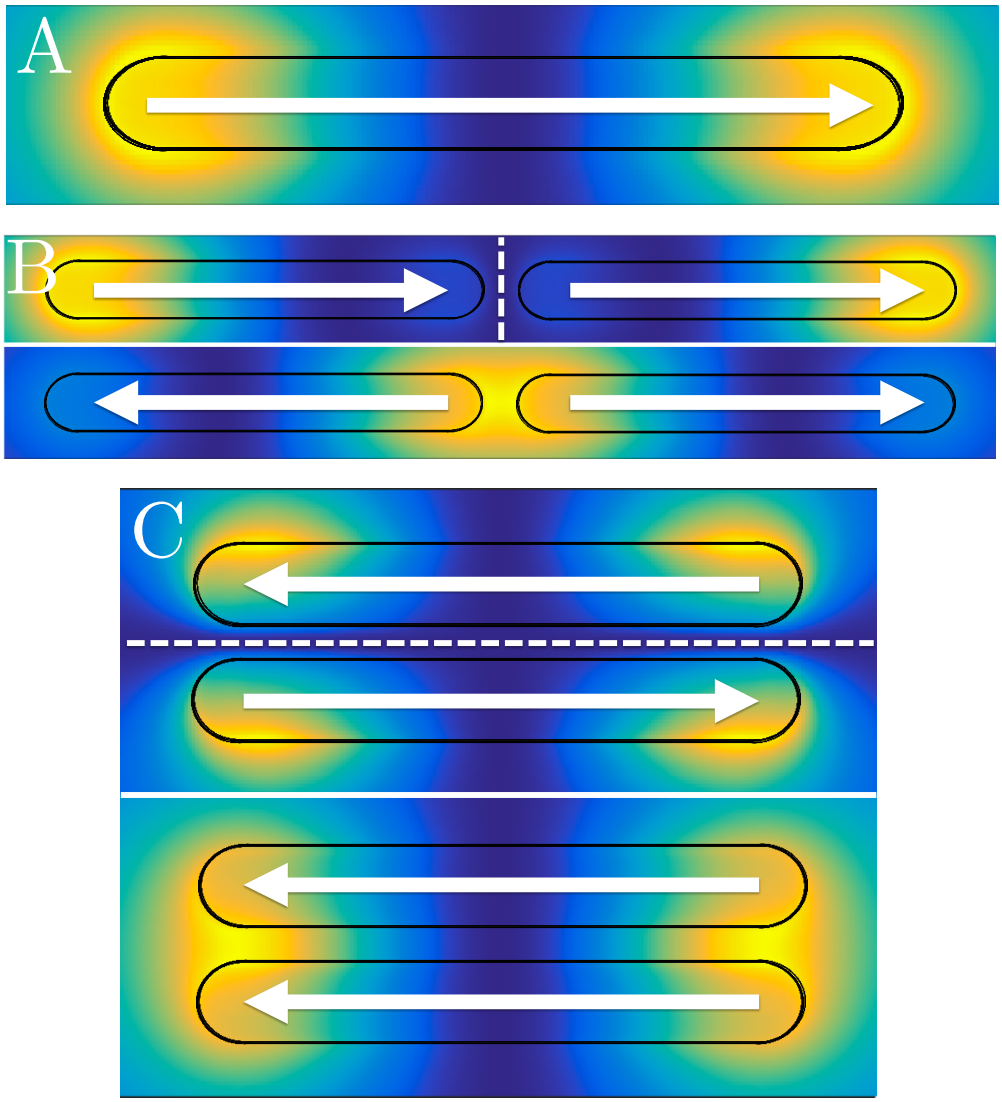

Figure 4.6: EELS maps of nanorod systems. **A:** The EELS map of a single nanorod displays lobes of high loss probability at the ends of the rod and a node going through the center. **B:** The collinear (top) mode of the longitudinal rod dimer has lobes of high loss probability on the outer tips and a nodal line in the particle junction. In contrast, the anti-collinear (bottom) mode has a lobe of high loss probability in the junction. **C:** The anti-parallel (top) mode of the transverse rod dimer has lobes of high probability on the tips with a nodal line in the junction between particles. The parallel (top) mode shows behavior but does not have a nodal line in the junction.

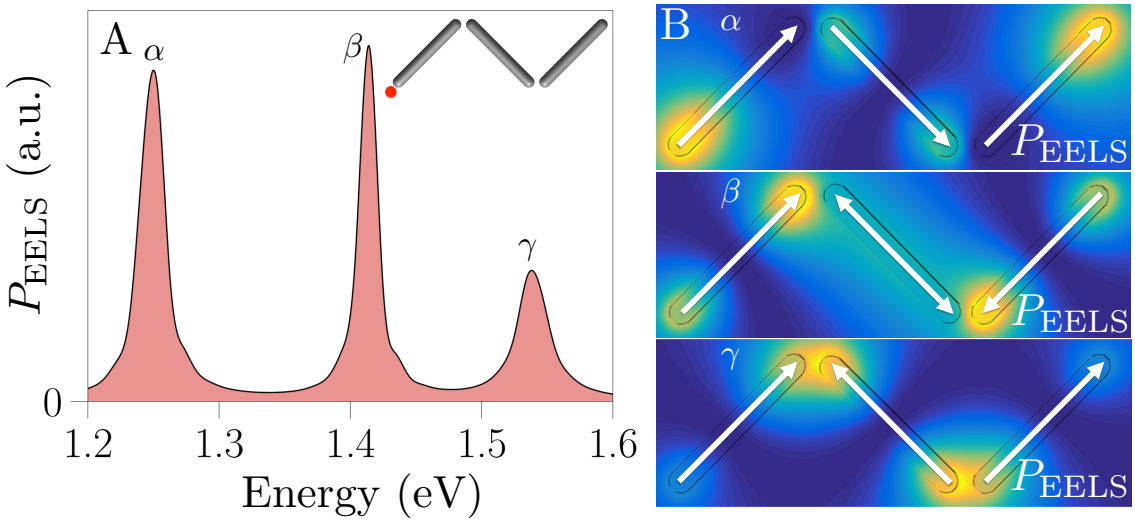

Figure 4.7: **A:** The EEL spectrum for a trimer of silver nanorods with lengths of 80 nm and diameters of 10 nm. The rods are arranged in a zig-zag configuration, where right angles are formed between one another as illustrated in the inset. **B:** Simulated EELS maps for peaks α, β, and γ. Mode α corresponds to the net dipole, where each dipole is head-to-tail. This is characterized in the EELS map by an enhanced nodal structure at the junctions. Mode β corresponds to one junction holding a head-to-tail configuration and the other a head-to-head configuration. Due to the electron forcing degenerate modes a node is not observed for this mode, but an asymmetry in EEL probability. The double sided arrow displayed represents the dipole orientation for each degenerate mode. Mode γ displays all head-to-head configurations in the junctions.

maximally out of phase dipolar plasmon mode.

The EEL spectrum and corresponding maps of the triangular nanorod trimer system are shown in Figure 7. The spectrum, shown in Figure 7A, contains two distinct peaks with the corresponding maps shown in Figure 7B. For the mode labelled α', nodes appear in all three junctions, corresponding to a head-to-tail configuration. Such head-to-tail configurations in sphere trimer systems have been known to exhibit magnetic plasmon behavior [42, 5, 140, 154, 136, 62, 138]. The mode labelled β' does not display any nodal structure in the junctions. This is counterintuitive, as it is impossible for every dipole to be oriented in a head-to-head configuration. This, once again, is a result of the electron beam driving two degenerate modes simultaneously. The double sided arrow displayed represents the dipole orientation for each degenerate mode.

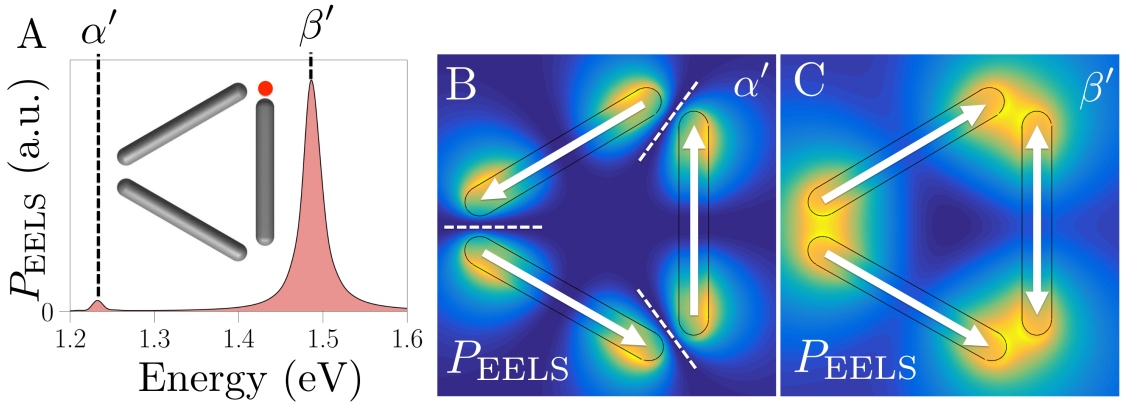

Figure 4.8: **A:** The EEL spectrum for a trimer of silver nanorods with lengths of 80 nm and diameters of 10 nm forming an equilateral triangle. **B:** Simulated EELS maps for peaks α' and β'. Mode α' contains nodes in every junction, meaning that each junction contains a head-to-tail orientation of dipoles. Mode β' does not contain any nodal structure in the junction. While it is impossible for every junction to have a head-to-head the electron beam forcing degenerate modes leads to a superposition of the EELS maps for these modes. The double sided arrow displayed represents the dipole orientation for each degenerate mode.

4.6 Methods

EELS experiments. EELS experiments are carried out in a monochromated Carl Zeiss LIBRA® 200MC (S)TEM operated at 200 kV. All EELS maps are acquired with a convergence semi-angle of 9 mrad, a collection semi-angle of 12 mrad, a dispersion of 29 meV per channel. The measured energy resolution (defined as the full width at half-maximum of the zero-loss peak) is 150 meV with the electron beam penetrating the Si_3N_4 substrate only. For the single particle EELS map acquisition, a region of interest with 30 $\times$ 29 pixel spectrums (1 pixel $\sim$ 8.1 nm $\times$ 8.1 nm) is defined over the whole Ag nanoparticle; While for the dimer EELS map acquisition, an ROI with 45 x 23 pixel spectrums (1 pixel $\sim$ 9.9 nm x 9.9 nm) is created. To generate the plasmon mode maps, the background of all pixel spectra are removed through the reflected-tail model routine using the Gatan Digital Micrograph software, and then normalize pixel by pixel by the zero-loss intensity. Finally, by plotting the EELS probability in designated energy slices, EELS maps are generated.

4.7 Conclusions

EEL maps can be interpreted as a measure of the self-induced backforce on the electron due to the excitation of LSPRs. In this paper we show that not only can the relative phase between coupled LSPRs be inferred through the emergence of nodal structure in EEL maps, but also EEL maps yield information about superpositions of degenerate modes. To support these claims, we have develop a Hamiltonian formalism to model STEM/EELS measurements on hybridized plasmonic nanoparticle assemblies and compare it to experiment and numerical electrodynamics simulations. A variety of monomer, dimer, and trimer systems are discussed. Particular emphasis is placed on comparing heterodimers of mixed polarizability to those of differing resonant frequencies, showing that care must be taken when interpreting plasmon localization in EELS maps. In particular, we show that degenerate systems of mixed polarizability also show localization but it is not related to the mixing of modes usually associated with plasmon localization in Fano-like systems. We apply this reasoning to the numerical study of dimer and trimer hybridized nanorod systems and find character attributed to the superposition of both modes in the case of degenerate trimer plasmons. This work provides a rubric for assigning the relative phases of each monomer within hybridized nanoparticle aggregates, thereby determining the character of the modes under study.

4.8 Acknowledgements

This work was supported by the U.S. Department of Energy, Basic Energy Sciences, under award number DE-SC0010536 (J.P.C., G.L.). G.L. also acknowledges support from a Notre Dame Energy postdoctoral fellowship. This work was supported by the National Science Foundation's CAREER program under award number CHE-1253775 (D.J.M.), NSF XSEDE resources under award number PHY-130045 (D.J.M.), and the University of Washington Clean Energy Institute fellowship (S.C.Q.).

Chapter 5

STEM/EELS IMAGING OF MAGNETIC HYBRIDIZATION IN SYMMETRIC AND SYMMETRY-BROKEN PLASMON OLIGOMER DIMERS AND ALL-MAGNETIC FANO INTERFERENCE

Reproduced with permission from:

C. Cherqui, Y. Wu, G. Li, S.C Quillin, J.A Busche, N. Thakkar, C.A. West, N.P. Montoni, P.D. Rack, J.P. Camden, and D.J. Masiello

Nano Letters, **2016**, 16 (10), pp 6668-6676

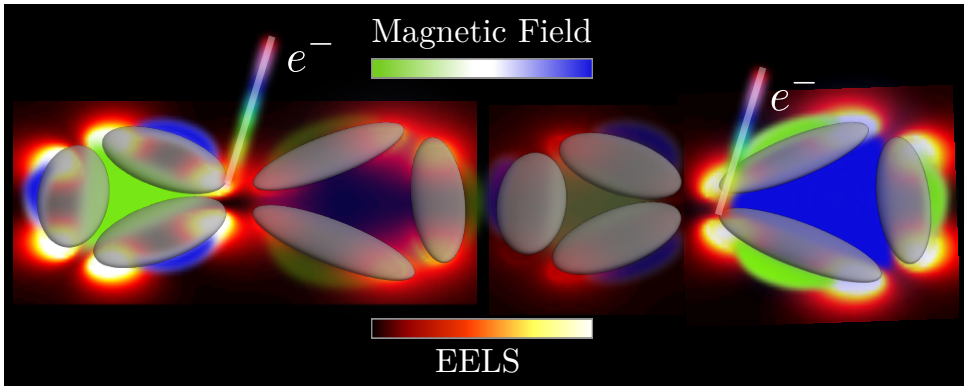

Figure 5.1: Abstract figure

5.1 Abstract

Negative-index metamaterials composed of magnetic plasmon oligomers are actively being investigated for their potential role in optical cloaking, superlensing, and nanolithography applications. A significant improvement to their practicality lies in the ability to function at multiple distinct wavelengths in the visible part of spectrum. Here we utilize the nanometer

spatial-resolving power of electron energy-loss spectroscopy to conclusively demonstrate hybridization of magnetic plasmons in oligomer dimers that can achieve this goal. We also show that breaking the dimer's symmetry can induce all-magnetic Fano interferences based solely on the interplay of bright and dark magnetic modes, allowing us to further tailor the system's optical responses. These features are engineered through the design of the oligomer's underlying nanoparticle elements as elongated Ag nanodisks with spectrally isolated long-axis plasmon resonances. The resulting magnetic plasmon oligomers and their hybridized assemblies establish a new design paradigm for optical metamaterials with rich functionality.

5.2 Article

The plasmon resonances of cyclic formations of metal nanoparticles, known as metamolecules[5, 6] or plasmon oligomers[57], produce more than the well-known strong local electric fields expected of surface plasmons; they also generate sizable magnetic fields at optical frequency[56, 25, 42]. Theoretical and experimental evidence suggests that when multiple oligomers are brought together to form extended nanostructures, magnetic plasmons hybridize in the same way as electric plasmons[29, 99, 100, 97, 96]. Akin to the bright and dark electric modes of hybridized nanoparticles, hybridized oligomers possess normal modes with bright and dark magnetic character[30]. The strongest evidence of magnetic hybridization has been reported in the extinction measurements of coupled chains of oligomers[99, 100, 97], metallo-dielectric nanoclusters[125, 151], and Au split ring hexamer nanostructures[13]. However, due to the limitations of far-field optical microscopy, the near-field character of this effect has never been directly observed. More problematic is the presence of many other spectrally overlapping non-magnetic features, which conspire to make the magnetic modes of interest difficult to isolate and identify.

Herein we experimentally demonstrate the existence of magnetic plasmon hybridization and all-magnetic Fano interferences in symmetric and symmetry-broken plasmon oligomer dimers. This is accomplished by performing electron energy-loss spectroscopy (EELS) in a scanning transmission electron microscope (STEM), providing the first near-field imaging of

these effects. We show, specifically, that a two-ring system composed of identical plasmon oligomers forms a magnetic homodimer with two hybridized magnetic modes: one with a cumulative magnetic moment and one without. We then extend the hybridization concept to create magnetic heterodimers and introduce a never-before-considered type of plasmonic Fano resonance built entirely upon the interplay of bright and dark magnetic modes, analogous to the all-electric Fano resonances present in nanoparticle heterodimers[144, 119]. This magnetic Fano effect serves as a platform to design nanosystems with plane-wave accessible magnetic character at multiple frequencies. The latter is achieved by exploiting the spectral isolation of the long-axis dipole of an elongated Ag nanodisk and using it as the underlying plasmonic element of a new kind of magnetically active oligomer that inherits this spectral isolation in its collective magnetic responses. These rationally-designed nanostructures could be used to optically control nanoscale etching[158], plasmonically enhance magnetically-active transitions in rare-earth ion-doped nanocrystals[74, 75, 114, 76], or create multi-color negative-index metamaterials[139, 28].

As described in the Methods Section, all oligomer nanostructures are fabricated using focused-ion-beam processing. All simulated EEL spectra, probability maps, and optical scattering spectra are based upon the boundary element method using the MNPBEM toolkit[61]. The simulated oligomers are parameterized according to the schematic presented in Figure 5.2a by an interparticle distance (d), and an individual nanoparticle length (L), width (w), and height (h). Simulations compared directly to experiments have values of d, L, and w determined from the high-angle annular dark-field (HAADF) image of the system under study. The height of each individual nanoparticle is left as a fitting parameter as it cannot be inferred from the HAADF image. All optical scattering simulations that are not compared to an experiment are calculated for L = 215 nm, w = 60 nm, d = 35 nm, and h = 20 nm unless otherwise noted. Substrate effects are subtracted from all experimental EEL spectra and the experimental dark-field scattering spectrum of the single-ring oligomer in in Figure 5.2f is an average of the spectra from five individual oligomers of nearly identical dimensions. We do no further post-processing of the optical or EELS data.

The proposed plasmon oligomer is composed of three elongated Ag nanodisks arranged equidistant from each other into the shape of an equilateral triangle and is presented schematically in Figure 5.2a. When composed of nanospheres, this is the well-known trimer metamolecule oligomer studied previously by others.[140, 115, 15] Many properties are common between the nanosphere and elongated nanodisk oligomer; therefore, we begin by introducing some common language and highlighting their differences.

To model the oligomers, we treat their underlying long-axis dipoles as a set of coupled mechanical oscillators. The normal modes of the system are calculated by diagonalizing the Hamiltonian

$$H = \sum_i \frac{\mathbf{P}_i^2}{2m_i} + \frac{1}{2} m_i \omega_i^2 \mathbf{Q}_i^2 - \frac{e^2}{2} \sum_{i \neq j} \mathbf{Q}_i \cdot \mathbf{\Lambda}_{ij}^{\mathrm{NF}} \cdot \mathbf{Q}_j, \tag{5.1}$$

where $\mathbf{Q}_i$ is the displacement coordinate of the ith dipole plasmon, $\mathbf{P}_i$ is its conjugate momentum, and $\mathbf{\Lambda}_{ij}^{\mathrm{NF}}$ is the standard near-field dipole-dipole interaction tensor. The model is parameterized by an effective mass m_i which is proportional to the inverse of the nanoparticle's polarizability and dipole surface plasmon frequency ω_i[30, 29]. The first of the two lowest energy modes predicted by this model is shown in Figure 5.2b and is denoted as the magnetic mode, M^0. Made up of a superposition of three dipoles oriented in a head-to-tail configuration, it has an effective magnetic moment induced by the underlying plasmonic nanodisks' oscillating electric field. However, due to the orientation of the dipoles and the symmetry of the system, its cumulative electric dipole moment is zero. The second lowest energy mode, denoted as the electric mode, E^0, is doubly degenerate and is made up of two in- and one out-of-phase dipoles. This configuration results in a net electric dipole moment but no appreciable magnetic moment. Consequently, the light emitted by the M^0 mode differs from that emitted by the E^0 mode, as it does so through a magnetic and not electric dipole moment. As will be shown below, this binary interplay of magnetic and electric modes with varying brightness and darkness extends to more complicated nanostructures; to distinguish between the nature of the light radiated by these modes, they are characterized as being either bright magnetic and dark electric (BM, DE) or dark magnetic and bright electric (DM, BE).

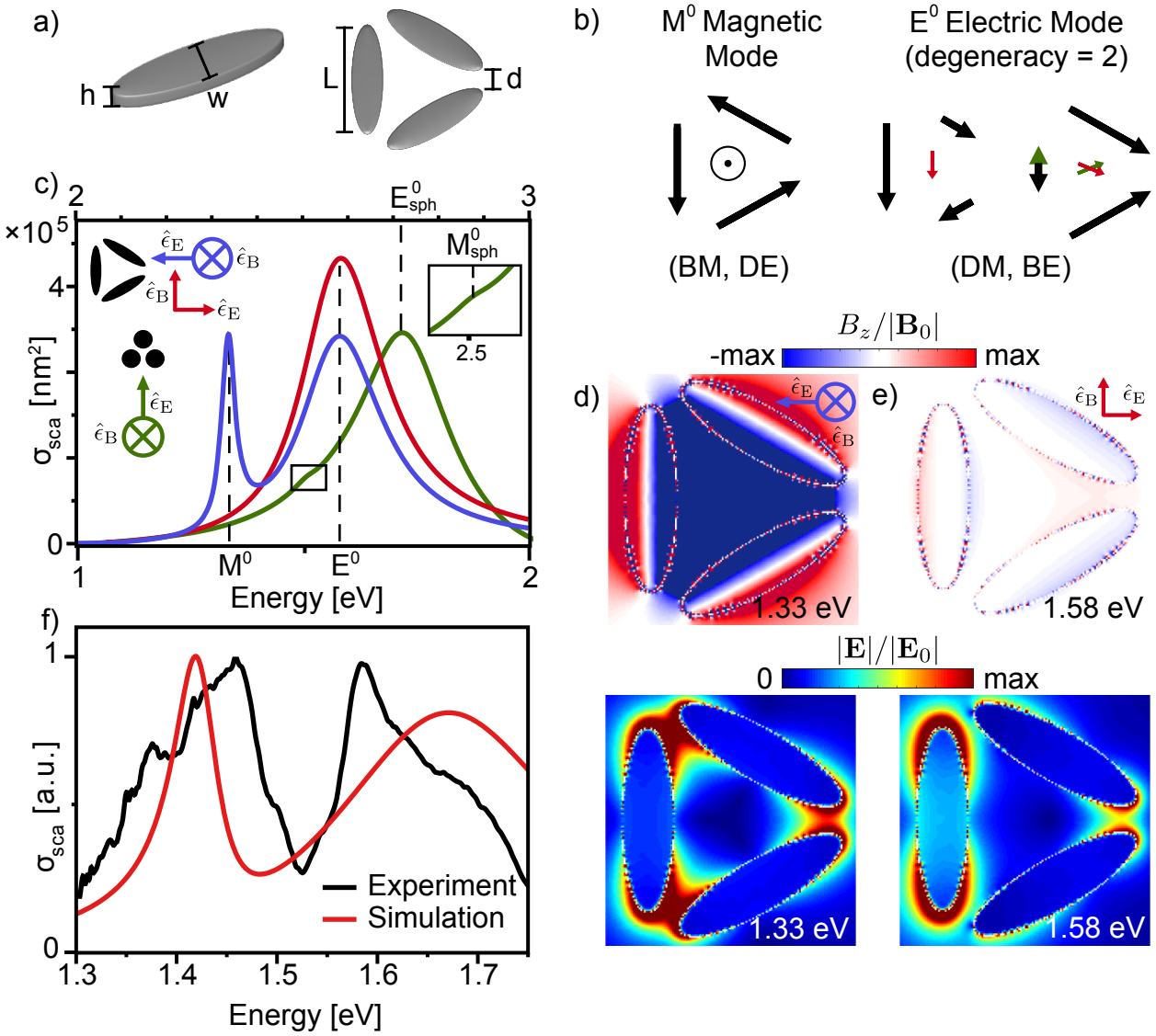

Figure 5.2: Simulated and experimental optical scattering of a single-ring plasmon oligomer. (a) Top-down and tilted views of the proposed Ag nanodisk plasmon oligomer parameterized by a nanoparticle length (L), width (w), height (h), and interparticle distance (d). (b) Eigenvector plots of the two lowest energy normal modes. The lowest is labeled the magnetic M^0 mode as it is (BM, DE) and the other is labeled the electric E^0 mode as it is (DM, BE) and is doubly degenerate. (c) Simulated total optical scattering cross-sections for a single-ring plasmon oligomer (red, blue). Also shown is the spectrum of the analogous nanosphere-based metamolecule (green) that has its electric and magnetic modes denoted as M^0_{sph} and E^0_{sph}, respectively. The inset magnifies the part of the spectrum that exhibits the M^0_{sph} peak. Each cross-section is based on the specific light polarization parameters shown schematically. (d,e) In-plane components of the magnetic and electric field magnitudes of the magnetic M^0 and electric E^0 modes. Both observables are normalized to the magnitude of the incident light. (f) Simulated (red) and experimental (black) forward scattering spectrum of a single-ring oligomer with dimensions of L = 210 nm, w = 80 nm, h = 15 nm, and d = 50 nm.

To better understand the nature of these modes, the simulated scattering cross-section of the proposed oligomer metamolecule is presented in Figure 5.2c. The spectrum computed using incident light with a magnetic field polarized perpendicular to the ring plane (blue) exhibits a narrow peak at 1.33 eV and a broad peak at 1.58 eV. The magnetic and electric near-fields corresponding to these resonances are plotted in Figures 5.2d and e, respectively. At 1.33 eV, the structure of the magnetic field indicates that the system has a magnetic moment oriented normal to the oligomer plane, while the strong local electric field in the junction between the nanodisks indicates that all of the dipoles are oriented in a head-to-tail configuration, characteristic of the (BM, DE) M^0 mode. Most notably, the M^0 mode has significant plasmon-enhancement capabilities, with a relative magnetic field strength of $|B_z|/|\mathbf{B}_0| = 18$ near the nanoparticle surface and 8 at the center of the ring. The relative electric field strength is highest near the nanoparticle surface, where $|\mathbf{E}|/|\mathbf{E}_0| = 20$ and is zero at the ring center. The magnetic field being non-zero in a region of space with no electric field is a system property that could be exploited to isolate and enhance optical-frequency magnetic transitions in ion-doped nanoparticles.[76] If the area enclosed by the nanoparticles could be made smaller, these enhancements could be further improved upon. This will be explored in the near future *via* electron-beam lithography and focused-ion-beam processing with a He^+/Ne^+ gas field ion source; advances in bottom-up synthetic methods of nanoparticle self-assembly[92, 131, 118] may provide a route for creating smaller nanorod oligomer systems with even higher magnetic field enhancements.

When the system is excited by light propagating perpendicular to the oligomer plane, the spectrum is dominated solely by a peak at 1.58 eV. Analyzing the structure of the simulated electric and magnetic near-fields plotted in Figure 5.2e allows us to correlate this 1.58 eV feature with the (DM, BE) E^0 mode, which can be excited with either polarization. Note that the cross-sections of the M^0 and E^0 modes have approximately the same magnitude, but differ significantly in line width, indicating that the magnetic resonance is longer-lived. Differences in lifetime are a result of the comparatively weak coupling between the magnetic moment and the radiation field. The magnetic mode could be useful, e.g., as a platform

for surface-enhanced Raman spectroscopy, as it provides a mode with a quality factor of 32 and the desired capacitive electric fields in each junction, the advantage being that these electromagnetic hot spots would all be simultaneously induced by a single incident polarization.

The conclusions drawn from the simulated spectra and field plots is supported by the dark-field scattering experiment presented in Figure 5.2f. Here, the simulated (red) and experimental (black) forward scattering spectrum of a single-ring oligomer with dimensions L = 210 nm, w = 80 nm, h = 15 nm, and d = 50 nm are in good agreement. Though the properties of the proposed oligomer and those of the analogous nanosphere-based metamolecule are qualitatively the same, comparing the simulated spectrum of the nanosphere-based system (Figure 5.2c, green) to that of the nanodisk-based system (Figure 5.2c, blue) shows that the oligomer proposed in this Letter has a sharper and more easily accessible magnetic response.

While the simulated EEL spectra and mode maps shown in Figure 5.3a and b (upper panels) support the conclusions drawn above, the experimental realization of the system studied using STEM/EELS (lower panel of Figure 5.3a) slightly deviates from the proposed oligomer design. The experimental isosceles, rather than equilateral, arrangement of nanoparticles must be accounted for as its broken symmetry lifts the degeneracy of the E^0 modes and leads to noticeable differences in the structure of the mode maps. However, as it is the equilateral system that is used as the base element of the dimers presented later, simulations for it are included in the upper panels of Figure 5.3. To differentiate between the modes of both systems, we remove the superscript and denote the relevant magnetic and electric modes of the isosceles system as M and E, respectively.

The simulated (middle) and experimental (lower) EEL spectra for the isosceles system are shown in Figure 5.3 and show excellent agreement by both exhibiting resonances at 1.39 and 1.59 eV. The simulated (middle) and experimental (lower) EEL probability maps are compared in panels b and c of Figure 5.3. At 1.39 eV (middle and lower, b), the EEL probability falls to zero in the junction between nanodisks, exhibiting the signature of the cyclic head-to-tail configuration of the M mode's electric dipoles[126]. The simulated and

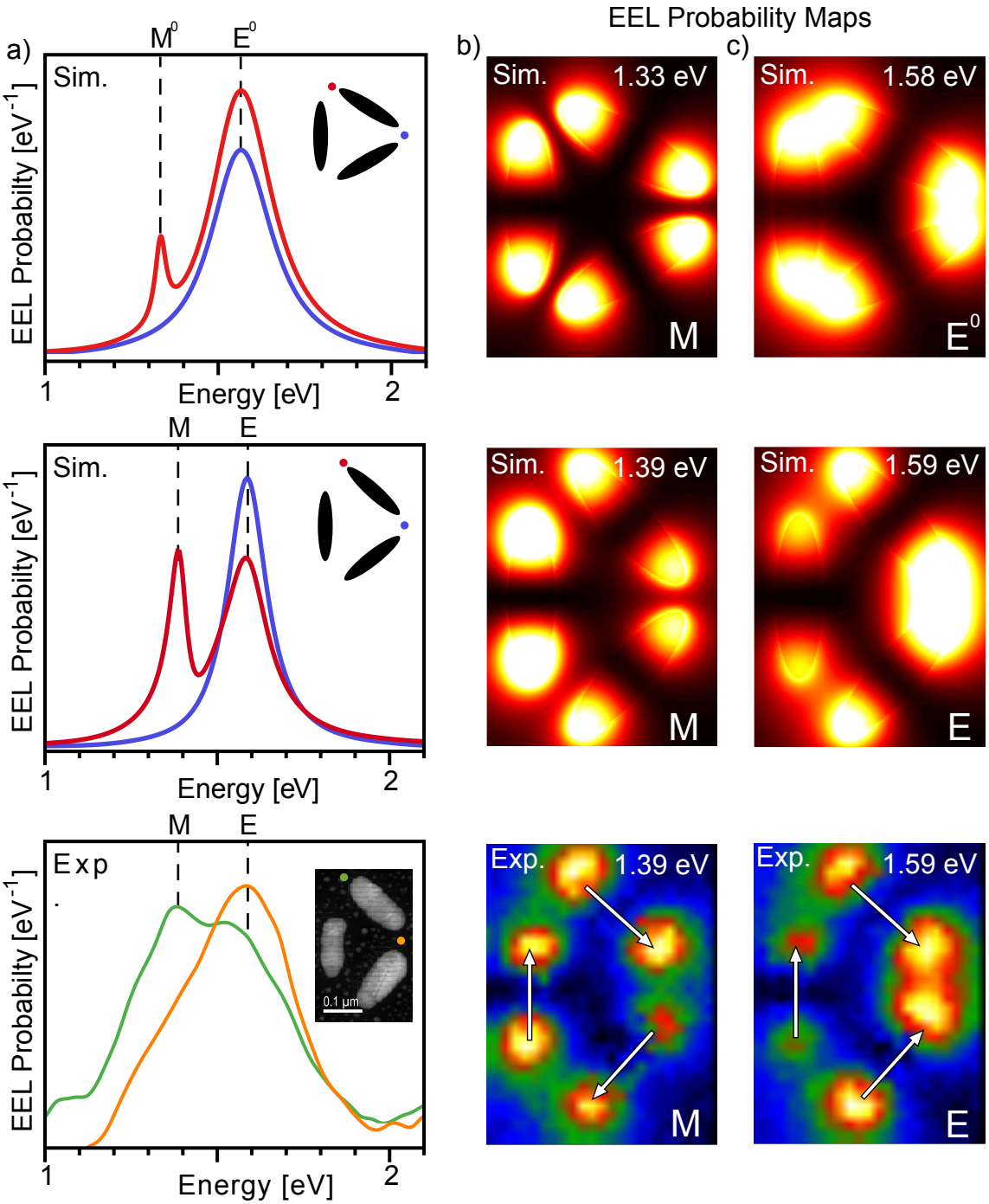

Figure 5.3: EELS of the symmetry-broken single-ring oligomer. (a) Simulated EEL spectra of the equilateral (upper panel, red, blue), isosceles (middle panel, red, blue), and experimental (lower panel, green, orange) single-ring oligomers. The ring geometry is specified in Figure 5.2 for the equilateral system; the isosceles system has an interparticle separation of 45 nm and 80 nm, with all other dimensions the same. Electron beam positions corresponding to each spectrum are schematically represented in each panel for the simulated spectra. The experimental beam positions are indicated on the HAADF image in the lower panel. (b) Simulated EEL probability maps for the equilateral (upper, 1.33 eV), isosceles (middle, 1.39 eV), and experimental (lower, 1.39 eV) oligomer's magnetic mode. (c) Simulated EEL probability maps for the equilateral (upper, 1.58 eV), isosceles (middle, 1.59 eV), and experimental (lower, 1.59 eV) oligomer's electric mode. In both (b) and (c), better agreement between simulation and experiment is found for the case of the isosceles system.

experimental maps at 1.59 eV (middle and lower, c) are also in excellent agreement, showing a structure indicative of the two-in-phase and one out-of-phase electric dipoles expected of the E mode. Interestingly, when we compare the simulated EEL spectra of equilateral- and isosceles-based oligomers (upper and middle panels of a, red), we observe the appearance of an asymmetric line shape with a dip that lines up with the one found in the corresponding experimental spectrum (lower panel of a, green). This implies that breaking the equilateral symmetry to an isosceles formation induces a Fano interference between the narrow (BM, DE) M mode and the broad (DM, BE) E mode, as described previously in other symmetry-broken metamolecules[140, 63, 115, 144, 119, 138].

Just as a pair of identical nanoparticles placed in close proximity form a plasmon homodimer with bonding in-phase bright and antibonding out-of-phase dark modes, two single-ring oligomers in close proximity form an oligomer homodimer that supports both bright and dark magnetic modes. Eigenvector plots of the homodimer's two lowest energy modes predicted by Eq. 5.1 are shown in Figure 5.4a. The lowest energy mode, denoted as north-north (NN), aligns the magnetic moment of each oligomer in-phase. The next higher energy mode, north-south (NS), has anti-parallel and out-of-phase magnetic moments[29].

The simulated optical scattering cross-section of this magnetic homodimer is plotted in Figure 5.4b using incident light appropriately polarized to excite the NN (blue) and NS (red) modes. The narrowest peaks the spectra are located at 1.3 eV and 1.35 eV. Assignment of the 1.3 eV resonance to the NN mode is confirmed by the structure of the simulated magnetic near-field plotted in Figure 5.4c. Here, the magnetic near-field shows a single polarization inside the rings, indicating that the system has the head-to-tail configuration of electric dipoles required of the NN mode. As observed previously for the single-ring oligomer, the global head-to-tail configuration of the underlying electric dipoles results in a cumulative magnetic moment and a net-zero electric dipole moment, giving the NN mode (BM, DE) optical properties. The plasmon-enhancement capabilities of the NN mode are weaker than those of the M^0 mode, with a relative magnetic field strength of $|B_z|/|\mathbf{B}_0| = 5$ close to the nanoparticle, and only $|B_z|/|\mathbf{B}_0| = 1$ at the left and right ring centers. The enhancement

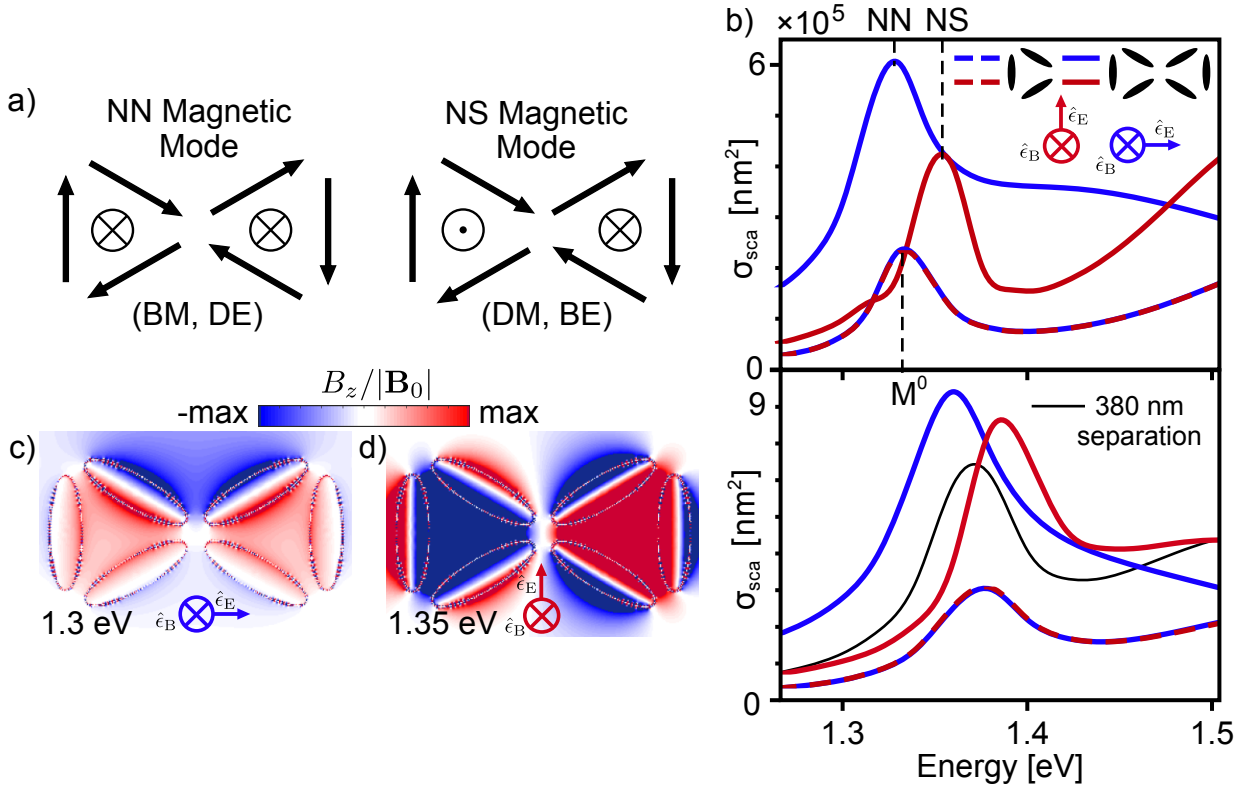

Figure 5.4: Simulated optical scattering properties of the magnetic homodimer. (a) Eigenvector plots of the two lowest energy homodimer normal modes. The lowest energy mode is a superposition of two in-phase single-ring magnetic modes and is labeled the NN mode. The second lowest energy mode is a superposition of two out-of-phase single-ring magnetic modes and is labeled the NS mode. (b) Optical scattering cross-sections for the magnetic homodimer simulated using light polarized according to the insets (upper, lower). The lower panel contains the spectra for a homodimer with dimensions of L = 225 nm, w = 70 nm, h = 20 nm, and d = 50 nm. Scattering cross-sections for the corresponding single-ring oligomers are also included (red dashed, blue dashed) for both sizes. The lower panel also includes the spectrum of two single-ring oligomers separated by a distance of 380 nm. (c,d) Magnetic near-fields of the NN and NS modes corresponding to the peaks in the spectrum of the upper panel of c). Asymmetries in the fields are due to retardation effects.

properties of the NN electric near-field are substantially higher with $|\mathbf{E}|/|\mathbf{E}_0| = 50$. The large reduction in magnetic field enhancement when compared to the enhancement produced by M^0 is due to the larger area enclosed by the NN mode[29, 5].

The NS mode is identified by examining the near-field plotted in Figure 5.4d at 1.35 eV. Here, the magnetic near-field shows opposite polarization in each individual ring, and can be identified as a superposition of two out-of-phase single-ring oligomer magnetic modes[29]. This further indicates that while the dipoles of each ring are in-phase with each other, they are oscillating 90 degrees out-of-phase with respect to those of the other ring. The NS mode is unique because it has a local magnetic response in the near-field without a global magnetic moment with which to radiate. From the point of view of the electric field, even though the dipoles of each individual oligomer sum to zero, the global symmetry of the mode means that the two outer-most dipoles are in phase, giving the NS mode a net electric dipole moment. This not only leads to the interesting discovery that the NS mode is (DM, BE), but also that the NN mode emits light in the direction orthogonal to the electric dipole-mediated light emitted by the NS mode, as can be seen by the polarization dependence of the spectra plotted in Figure 5.4b. The relative magnetic field strength of the NS mode is much higher than that of the NN with $|B_z|/|\mathbf{B}_0| = 18$ near the surface of the nanoparticles and $|B_z|/|\mathbf{B}_0| = 9$ at the center of the rings. The relative electric field strength is lower than the 50-fold enhancement found in the NN mode, with $|\mathbf{E}|/|\mathbf{E}_0| = 30$.

In the following, EELS experiments are conducted on a homodimer with dimensions of L = 225 nm, w = 70 nm, h = 20 nm, and d = 50 nm. To show that magnetic hybridization persists at this larger size and interparticle separation distance, the same set of optical scattering simulations presented in the upper panel of Figure 5.4b are repeated for the larger system in the lower panel. The spectra of the corresponding single-ring oligomers for both sizes are also included (red and blue dashed), illustrating that the requisite polarization-dependent energy splitting that is the optical signature of magnetic mode hybridization appears in both systems. The lower panel also features the spectra of two single-ring oligomers separated by a distance of 380 nm (solid black), showing that when the system is uncoupled the spectrum is

simply twice that of the single-ring oligomer, indicating that all oligomer dimers considered in this Letter are truly hybridized.

Even though the properties of the magnetic homodimer might at first glance seem similar to those of the single-ring oligomer, there are several important distinctions to draw. First, the near-field properties of the lowest energy modes differ greatly between the two systems despite the preservation of their energy ordering and far-field optical properties: (BM, DE), (DM, BE). Further, the M^0 mode is the only normal mode of the single-ring system that has magnetic character, while both the NN and NS modes have significant local magnetic responses. From a geometric point of view, the systems do not share the same symmetry; the oligomer homodimer has two-fold symmetry and the single-ring oligomer has three-fold symmetry. As a result, the single-ring oligomer and the oligomer homodimer have different polarization dependencies. For a single ring, the doubly degenerate nature of the E^0 mode implies that some component of its net electric dipole moment is always in the plane of the ring, and when this effect is combined with the spectral overlap between the M^0 and E^0 modes it becomes impossible to solely excite the M^0 mode. In contrast, the homodimer's high aspect-ratio geometry means that light polarized to have its magnetic field perpendicular to the oligomer plane and its electric field aligned with the dimer's long axis can selectively excite the NN mode (as is plotted in solid blue in Figure 5.4b). When this condition is met, the scattering cross-section of the NN mode is larger than the NS mode. Moreover, even though the NN and NS modes can be accessed from a single polarization, the NN mode only appears as a small shoulder on the low energy side of the NS peak (Figure 5.4c, upper). This gives the homodimer optical properties that have no analogue in the single-ring oligomer: an effective polarization-dependent magnetic response. Specifically, with the magnetic field aligned normal to the oligomer plane, dark magnetic behavior is accessed via electric field polarization along the homodimer's short axis and bright magnetic behavior is accessed via electric field polarization along its long axis.

To date, the only evidence showing the existence of magnetic mode hybridization in plasmon oligomers is in optical scattering experiments[56, 42, 63, 140, 99, 100]. This, however,

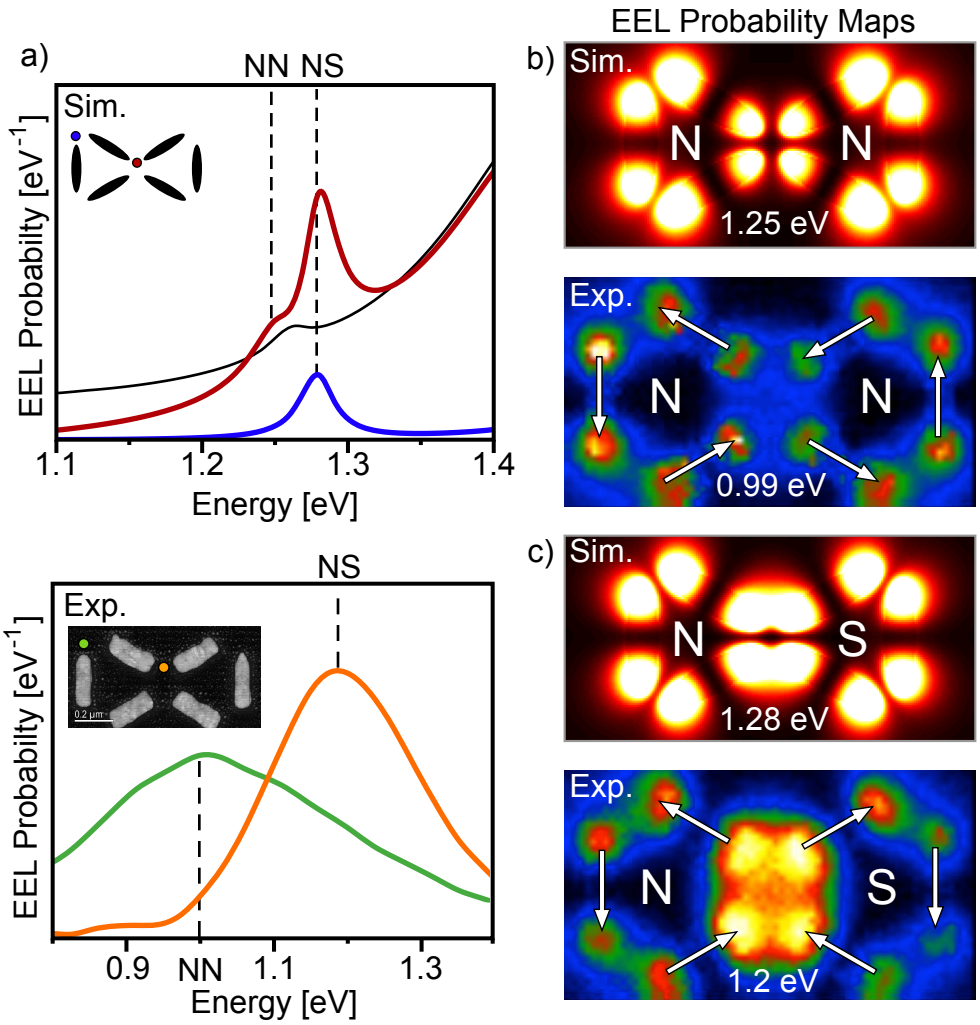

Figure 5.5: EELS of the magnetic homodimer. (a) Simulated (upper panel, blue, red) and experimental (lower panel, green, orange) EEL spectra. Electron beam positions for the simulated spectra are indicated schematically in the inset. The experimental beam positions are indicated on the HAADF image in the lower panel. Also shown for comparison is the EEL spectrum of the equilateral single-ring oligomer (upper, black). The 1.25 eV shoulder in the simulated spectrum is excited at the same beam position that gives an experimental peak at 0.99 eV. The simulated peak at 1.28 eV is correlated to the experimental peak located at 1.2 eV. (b) Simulated (upper, 1.25 eV) and experimental (lower, 0.99 eV) EEL probability maps of the NN mode. (c) Simulated (upper, 1.28 eV) and experimental (lower, 1.2 eV) EEL probability maps of the NS mode.

is not conclusive as it relies on simulation to correlate the spectral signature of oligomer hybridization with the structure of the near-field. To address this, we perform STEM/EELS experiments on the magnetic homodimer displayed in the HAADF image in Figure 5.5a (lower panel), allowing us to directly image magnetic mode hybridization with nanometer-scale resolution. Figure 5.5a shows the simulated (upper panel) and experimental (lower panel) EEL spectra for the indicated electron beam positions. For reference, the simulated EEL spectrum of the equilateral single-ring oligomer is also presented (upper panel, black). For the purposes of simulation, the homodimer is assumed to have dimensions of L = 225 nm, w = 70 nm, d = 50 nm, and h = 15 nm. For these parameters, the simulated spectrum shows resonances at 1.25 and 1.28 eV. The experimental spectrum exhibits a peak at 0.99 eV when the electron beam is placed at the tip of the outermost nanodisk and a peak at 1.2 eV when placing the beam in between the two center nanodisks. The simulated and experimental EEL probability maps (Figures 5.5b and c) show close agreement and support the mode assignments described above. Most telling is the structure of the mode maps in the junction between the nanodisks at 1.25 eV in the simulation and 0.99 eV in the experiment, which indicates that all of the dipoles are oriented in the head-to-tail configuration expected of the NN mode. The difference in energies between the simulated and experimental results are most likely due to the fact that the experiments are performed on a 30 nm SiN_4 substrate, while the simulations are performed without one. Substrates are known to red-shift and detune modes and close inspection of the EEL probability maps show that they are consistent with magnetic plasmon hybridization theory[29] and simulation.

To experimentally verify the existence of the NS mode, Figure 5.5c compares the simulated EEL mode map at 1.28 eV to the one obtained experimentally at 1.2 eV. Here, in both simulation and experiment, the nodal structure of the EEL map in the junction between nanodisks indicates that while the dipoles in each ring are oriented in a head-to-tail configuration, they are 90 degrees out-of-phase with respect to those of the other ring, thereby identifying the experimental peak at 1.2 eV as the NS mode. Differences in the mode energy between simulation and experiment are again likely due to the presence of the SiN_4 substrate, substrate

impurities, and the intrinsic imperfections and asymmetries of the individual nanodisks. This definitive assignment of the NN and NS magnetic modes in EELS proves that the identical single-ring oligomers composing the homodimer are indeed hybridized.

As the NS mode is magnetically dark, the applicability of the design is limited to situations that only require a single bright magnetic mode. We now show that by introducing asymmetry to the design, the (BM, DE) M^0 mode of the left ring mixes with the corresponding M^0 mode of the right ring, giving rise to left- and right-ring localized magnetic modes and creating a multi-color magnetically bright oligomer system. This is accomplished by changing the particle lengths L_1 and L_2 of each respective ring. Figure 5.6a shows an eigenvector plot of the heterodimer's magnetic normal modes predicted by Eq. 5.1. The lowest in energy is localized to the left ring and is denoted as the north (N) mode. The second lowest energy mode is localized to the right ring and is denoted as the south (S) mode. This is akin to the plasmon localization exhibited in nanoparticle heterodimers, with the magnetic mode's differently sized rings playing the role of a pair of nanospheres each with a different radius[27].

Figure 5.6b shows the simulated optical scattering cross-sections for heterodimers of varying asymmetry excited using two polarizations. The panels are divided by the polarization of the light used to excite the system and include spectra for $L_2 = 215$ (black solid), 200 (black dotted), and 185 nm (plotted in the same color as the corresponding inset). The upper panel of Figure 5.6b shows the cross-sections simulated with incident magnetic fields polarized to be perpendicular to the oligomer plane. The spectrum for $L_2 = 215$ nm is initially dominated by the NS mode, but as the right ring becomes smaller, the spectrum evolves to show two peaks. For $L_2 = 185$ nm the spectrum has peaks at 1.33 and 1.49 eV. For incident light with an electric field aligned along the dimer's short axis, The lower panel of Figure 5.6b shows a pair of spectra initially dominated by the NN mode but otherwise following a similar evolution. Note the characteristic asymmetric line shapes that appear for $L_2 = 200$ nm, caused by the Fano interference of the left- and right-ring-localized magnetic plasmons. The electric and magnetic near-fields for the $L_2 = 185$ nm heterodimer are compared in Figures 5.6c and d. Here, we see the complementary effect of left- and right-ring plasmon localization induced

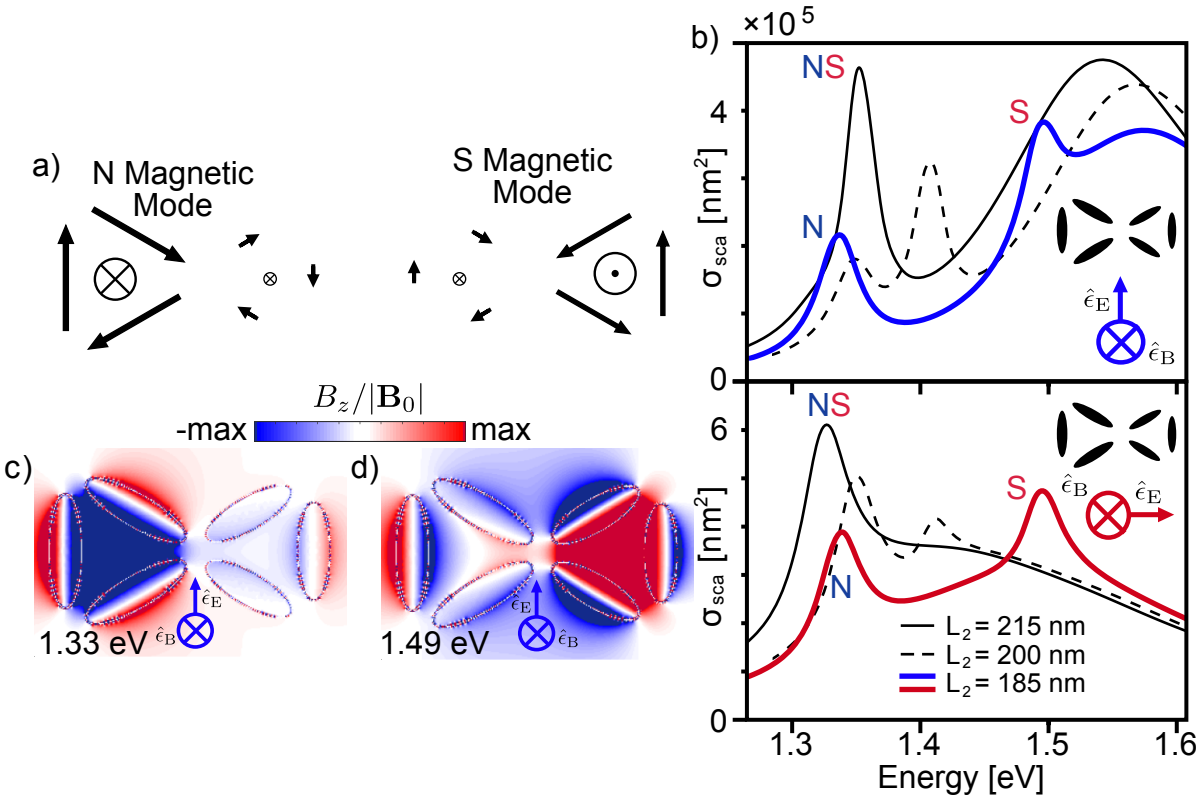

Figure 5.6: Simulated optical scattering properties of the magnetic heterodimer. (a) Eigenvector plots of the two lowest energy normal modes. The lowest energy mode is an asymmetric superposition of two in-phase single-ring magnetic modes and is labeled the north (N) mode. The second lowest energy mode is an out-of-phase superposition of single-ring magnetic modes. Localized to the right ring and 90 degrees out-of-phase with the N mode, it is labeled the south (S) mode. (b) Optical scattering cross-sections for magnetic dimers with $L_1 = 215$ nm and $L_2 = 215$, 200, and 185 nm. Otherwise all particles have dimensions of w = 60 nm, h = 20 nm, and d = 35 nm. The systems are simulated for two incident polarizations, marked schematically in each panel. (c,d) Comparison of the magnetic near-fields of the N and S modes, showing the complementary structure of the two fields.

by the hybridization of asymmetric single-ring oligomers. Notice the residual electric dipole moment of the left ring of the S mode caused by the spectral overlap of the S mode with one of the non-magnetic electric modes. The N mode has a relative magnetic field strength $|B_z|/|\mathbf{B}_0| = 15$ near the nanoparticle surfaces of the left-ring nanoparticles and $|B_z|/|\mathbf{B}_0| = 10$ at the center of the left ring. The S mode, in contrast, has $|B_z|/|\mathbf{B}_0| = 22$ at the nanoparticle surfaces of the right ring and $|B_z|/|\mathbf{B}_0| = 12$ at the center of the right ring, the largest of any of the systems presented. The heterodimer has the smallest relative electric field strength of any of the systems considered, with $|\mathbf{E}|/|\mathbf{E}_0| = 10$ for both modes.

Figure 5.7a shows simulated and experimental EEL spectra for the electron beam positions shown schematically in the top right corner of each panel; an HAADF image of the experimental heterodimer appears in the lower panel. For the purposes of simulation, the left ring of the heterodimer is modeled to have dimensions equal to the left ring of the homodimer shown in Figure 5.5, while the right ring is composed of similar nanoparticles with the exception that they now have a length of $L_2 = 190$ nm. When the beam is placed near the long axis of the outer most nanodisk of the left ring (blue dot in simulation, green dot in experiment), the simulated spectrum shows a peak at 1.26 eV and its experimental counterpart exhibits a peak at 1.1 eV. Comparing the simulated and experimental mode maps in Figure 5.7b shows the left ring localization expected of the N mode. When the beam is placed to excite the right ring instead, the simulated and experimental spectra exhibit peaks at 1.43 and 1.32 eV, respectively. Comparing their mode maps (Figure 5.7c) allows us to correlate these features with the S mode. Differences between the simulated and experimental results are again attributed to the presence of a 30 nm SiN_4 substrate, substrate impurities, and the intrinsic imperfections and asymmetries of the individual nanodisks.

To better understand the relationship between plasmon localization in the EEL maps and the degree of plasmon hybridization in symmetry-broken plasmon oligomers, we compare the simulated optical scattering cross-sections and EEL probability maps of three dimer systems with varying amounts of asymmetry. Figure 5.8a shows the scattering cross-sections for all three systems for incident light with an electric field polarized along the long axis

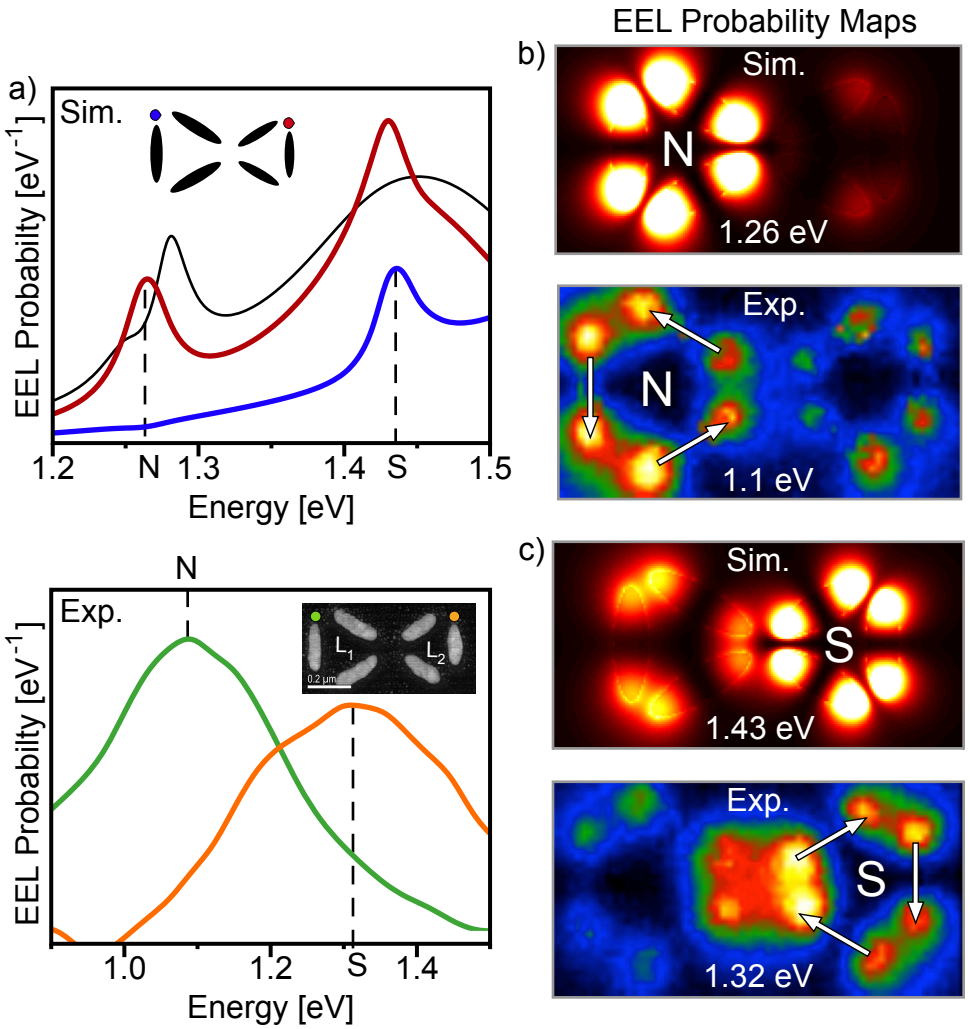

Figure 5.7: EELS of the magnetic heterodimer. (a) Simulated (upper panel, blue, red) and experimental (lower panel, green, orange) EEL spectra of the magnetic heterodimer for electron beam positions indicated schematically in the insets. The nanoparticles in the left and right rings have the dimensions w = 70 nm, h = 15 nm, and d = 50 nm. The left ring nanoparticles have a length L_1 = 225 nm and the right ring nanoparticles have a length L_2 = 190 nm. Also shown for comparison is the EEL spectrum of the homodimer (black). The 1.26 eV peak in the simulated spectra is excited at the same beam position that produces the experimental peak at 1.1 eV. The simulated peak at 1.43 eV is correlated to the experimental peak at 1.32 eV. (b) Simulated (upper, 1.26 eV) and experimental (lower, 1.1 eV) EEL probability maps of the left localized N mode. (c) Simulated (upper, 1.43 eV) and experimental (lower, 1.32 eV) EEL probability maps of the right ring localized S mode.

of the oligomer dimer and a magnetic field polarized normal to the oligomer plane. This is contrasted against the EEL probability maps of the two lowest energy modes of each system in Figure 5.8b. For $L_2 = 215$ nm, the homodimer spectrum exhibits a single NN peak. The corresponding EEL probability maps of the NN and NS (Figure 5.8b, upper) modes shows the expected mirror symmetry of the homodimer. When the nanoparticles of the second ring are reduced in size to $L_2 = 200$ nm, the homodimer's single peak splits into two (Figure 5.8a, middle) and the corresponding EEL probability maps (Figure 5.8b, middle) show some degree of plasmon localization. When $L_2 = 185$ nm, the scattering cross-section fully splits and exhibits two distinct peaks (Figure 5.8a, lower), while the corresponding mode maps (Figure 5.8b, lower) now show the same degree of spatial localization found in experiment (Figures 5.7b and c, lower). This evolution of the oligomer dimer's magnetic plasmon localization as a function of symmetry breaking, is a complementary signature of the Fano interference predicted in the optical scattering simulations presented above. Non-magnetic Fano and Fano-like interferences in nanoprods and plasmon-mode localization in nanocubes due to subtrate-induced symmetry breaking have been discussed in the context of EELS in the past; see, e.g., Refs. [91, 32, 17]

In conclusion, we theoretically predict and experimentally verify that properly designed cyclic assemblies of high-aspect ratio nanoparticles exhibit both bright and dark magnetic properties, presenting the first near-field mapping of magnetic plasmon hybridization in oligomer metamolecules. We further show how the global symmetry of these systems can be manipulated to create symmetry-broken oligomer dimers that exhibit all-magnetic Fano resonances, leading to nanostructures with multiple plane-wave-accessible bright magnetic modes. This work provides researchers with a new paradigm with which to design magnetically-active plasmon metamolecules with higher-order magnetic properties, laying the groundwork for future optical metamaterials with even richer functionality.

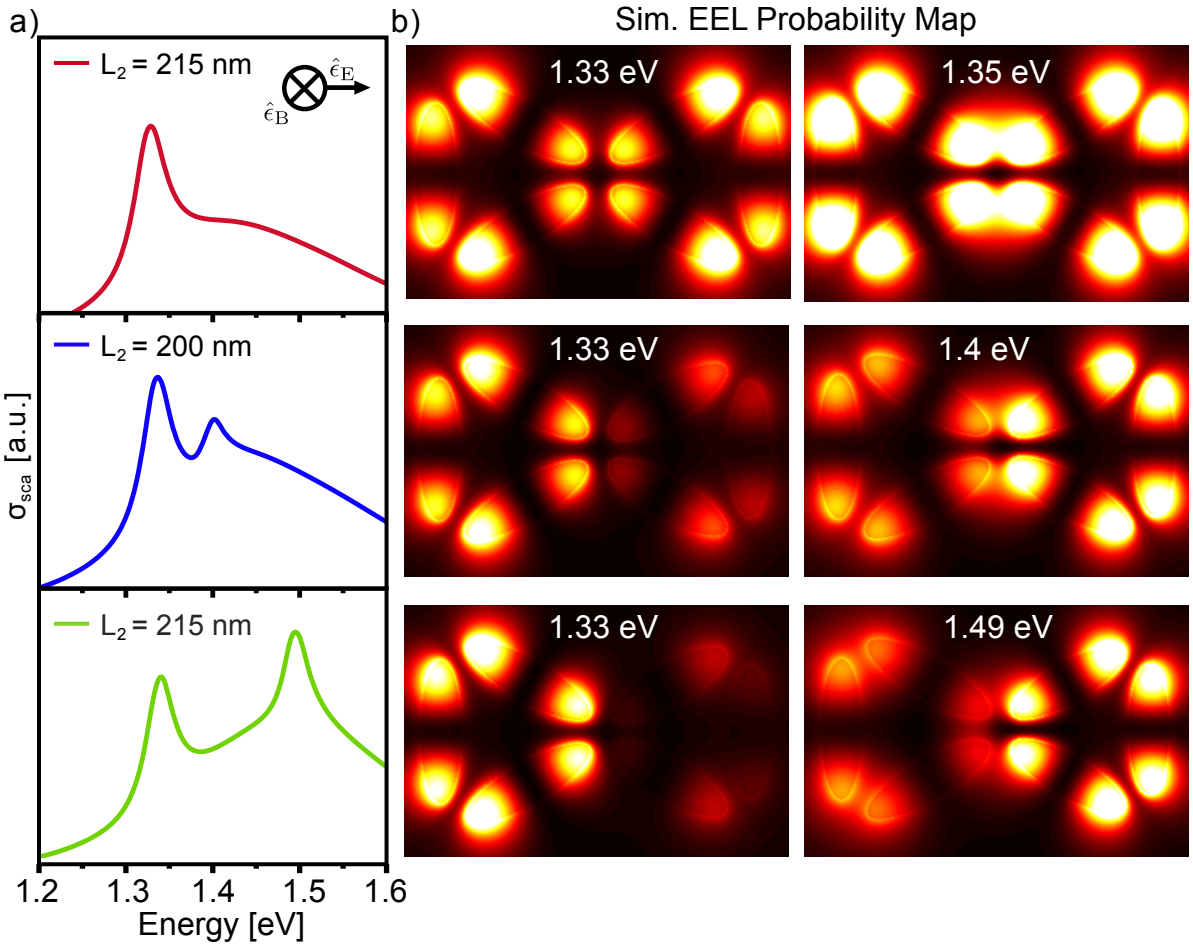

Figure 5.8: Signatures of symmetry-breaking in the EELS and optical scattering of magnetic dimers. (a) Simulated scattering cross-sections for $L_1 = 215$ nm and $L_2 = 215$, 200, and 185 nm for the incident light polarization shown schematically in upper panel. (b) Corresponding to each spectrum, the EEL probability maps are presented for the two lowest energy modes for all three values of L_2, showing the progression of the magnetic plasmon's localization as the degree of symmetry-breaking is increased.

5.3 Methods

All nanostructures are fabricated *via* focused-ion-beam milling (FIB) of a 20 nm thick, RF magnetron sputter deposited Ag thin film. A 4 × 4.8 μm area is raster scanned in a single ion beam pass with a 1 pA current and a 1.3 ms dwell time with a 30 keV Ga^+ beam from an FEI Nova 600 dual-beam system. The low current and a single beam pass facilitate the milling of fine structures and inhibit dewetting of the thin Ag film during the FIB milling process. Scattered small particles below a few nanometers can be observed in the TEM imaging due to redeposition during FIB milling.

All EELS experiments are carried out in a monochromated Carl Zeiss LIBRA 200MC (S)TEM operated at 200 kV. Acquisitions of the EELS spectrum image are performed with a convergence semi-angle of 9 mrad, a collection semi-angle of 12 mrad, a dispersion of 29 meV per channel, and a dwell time of 0.1 s. For the single-ring oligomer, the spectrum image consists of 31 × 24 pixels (1 pixel ≈ 13 nm × 13 nm) and for the homo- and heterodimers, it consists of 68 × 38 of pixels (1 pixel ≈ 15 nm × 15 nm). The measured energy resolution (defined as the full width at half-maximum of the zero-loss peak) is 200 meV. The experimental EEL spectra (Figure 5.3, 5.5, 5.7) are normalized to the zero-loss peak and the background signal of the substrate has been subtracted. The background spectra are taken by placing the beam at a position far away from the particles. To account for variation in the background signal due to substrate thickness, roughness, and particle-surface scattering, we amplify the background for a clean subtraction. To generate the EEL probability maps, the zero-loss peaks of all pixel spectra are removed through the reflected-tail model routine using the Gatan Digital Micrograph software, normalized pixel by pixel by the zero-loss peak intensity. Finally, by plotting the spectral intensities in designated energy slices, the plasmon maps are generated.

The enhanced darkfield hyperspectral images were provided by CytoViva, Inc. (Auburn, AL USA). This integrated system utilizes a research grade optical microscope equipped with an enhanced darkfield illumination condenser system and a 100× oil objective with

variable NA iris. The source illumination is an aluminum quartz halogen lamp. The hyperspectral imaging components utilize a diffraction grating hyperspectral imager and integrated CCD. Hyperspectral image capture is conducted using a line scan or pushbroom system. Hyperspectral image analysis was conducted with a customized version of the ENVI hyperspectral image software, designed specifically for nanoscale hyperspectral analysis.

5.4 Acknowledgements

P.D.R. acknowledges support from NSF Grant CBET-1603780. The authors acknowledge that the nanofabrication was performed at the Center for Nanophase Materials Sciences, which is sponsored at Oak Ridge National Laboratory by the Scientific User Facilities Division, Office of Basic Energy Sciences, U.S. Department of Energy. This work was supported by the U.S. Department of Energy, Basic Energy Sciences, under award number DE-SC0010536 (J.P.C., G.L., Y.W.). G.L. also acknowledges support from a Notre Dame Energy postdoctoral fellowship. This work was supported by the National Science Foundation's CAREER program under award number CHE-1253775 (D.J.M.), NSF XSEDE resources under award number PHY-130045 (D.J.M.), and the NSF Graduate Research Fellowship Program under award number DGE-1256082 (N.T.). The authors gratefully acknowledge CytoVivo, Inc. for providing hyperspectral visible near infrared darkfield microscope of the single-ring oligomer.

Chapter 6

CAVITY MODES OF OXIDE NANOPARTICLES PROBED BY MONOCHROMATED ELECTRON ENERGY-LOSS SPECTROSCOPY

This work is currently under review:

Q. Liu, S.C. Quillin, D.J. Masiello, P.A. Crozier

6.1 Abstract

The excitation of resonant optical-frequency geometric modes in individual oxide nanoparticles is explored using monochromated electron energy-loss spectroscopy in a scanning transmission electron microscope. These geometric or cavity modes are found to produce a progression of resonance peaks within the bandgap regions of the electron energy-loss spectra in CeO_2, TiO_2, and MgO nanoparticles. Complementary simulations of the electron probe combined with analytic Mie analysis are performed to interpret the complex spectral features and to understand their underlying physical origins. The factors that influence the energies, shapes, and strengths of these modes are also investigated and their dependence upon nanoparticle size, geometry, refractive index, aggregation, impact parameter, and electron kinetic energy are elucidated. Taken together, this work demonstrates the unique ability of fast electron spectroscopy to determine the photonic density of states in individual and few-particle assemblies of dielectric nanoparticles.

6.2 Introduction

Controlling the nanolocalization of light through engineering optical responses in dielectric structures has drawn ever increasing interest, since it can be applied to enhance light

absorption in solar cells [112], detect unlabeled molecules [153, 134], and optimize cavity quantum electrodynamics (QED) systems [150, 105]. Such applications cannot be fully achieved without a fundamental understanding of the resonance effects and optical behaviors of dielectric materials confined to micro- to nanoscale dimension. It is precisely in these size regimes where highly localized measurements that correlate the detailed structures of the observed materials with their optical responses are needed.

Electron energy-loss spectroscopy (EELS) coupled to a scanning transmission electron microscope (STEM) provides a unique approach for probing a materials' optical properties with nanometer-scale spatial resolution. The fast electrons in a STEM can be viewed as an evanescent source of supercontinuum light that is spatially localized far below the diffraction limit. Under certain circumstances, a target material may exhibit resonances when interacting with this spatially localized, supercontinuum light source, causing a deceleration or kinetic energy loss in the uniform motion of the fast electrons. Such resonances may be due to intrinsic electronic or vibrational degrees of freedom of the target or even to geometric resonances in which the target's boundary surfaces confine a set of geometry-specific optical standing waves. Although EELS is traditionally used to measure a target specimen's intrinsic electronic or vibrational excitations, it can also be a suitable tool to probe geometric resonance phenomena. As the STEM electron beam is positioned at different locations surrounding and within the target, the excitation strength of certain resonance modes can be enhanced or diminished, allowing one to learn about both the spectral and spatial distribution of target resonances.

The high energy-loss region of the EEL spectrum (called core-loss EELS, $\geq$50 eV) is usually used for identifying elemental and bonding information, while the low-loss region ($\leq$50 eV) provides information on interband transitions, plasmons, states within the bandgap, vibrational modes and radiative losses [40]. In this low-loss region, the EEL spectral intensity can be described by dielectric response theory, and is thus linked to the optical properties of a material [66, 129, 155]. For example, low-loss signals can be used to derive a materials' complex dielectric function through Kramers-Kronig analysis in ideal cases [4, 160, 142, 46, 152]. Recent developments in monochromators has improved the energy resolution of EELS to 10

meV, contributing to a significantly reduced background from the tails of the elastic peak [83, 82]. The improved signal-to-background allows subtle features in the low-loss region of the spectrum to be observable, thus opening up new opportunities such as detecting local vibrational signals, plasmon peaks, bandgaps, and bandgap states [82, 85, 34, 35, 41, 24, 101]. For the purpose of our work here, monochromated EELS enables detection of local geometric resonance modes with energies in the infrared-visible range and peak widths on the order of one hundred meV.

Depending on the specific target material and geometric shape, different types of resonance phenomena have been realized and studied using fast electrons. For example, using cathodoluminescence (CL), intensity maxima were observed within the optical bandgap of ZnO wires and tapered ZnO nanoneedles with hexagonal shaped cross-section, and interpreted as whispering gallery modes (WGM)[113, 36]. Similar WGM resonances appeared in EELS of SiO_2 nanospheres at energies ranging from 6-9 eV [67]. Thickness dependent peaks were measured within the direct bandgap region of the spectrum of silicon nanocomposite materials and interpreted as waveguided Cherenkov modes [159]. Also, simulated dispersion maps were compared with the experimental EEL spectral peaks observed from GaN and Ge nanowires, and understood to be waveguide modes induced by transition radiation from the relativistic STEM electrons[7, 68].

This work is in part motivated by our desire to study the properties of oxide nanoparticles of importance in photocatalysis. Understanding how nanoparticle composition, shape, and size affect surface electronic structure and geometry-induced optical resonances is critical to functionality. The particular focus of this work is on investigating the behavior of the latter geometric resonant modes on catalytically relevant oxide nanoparticles such as TiO_2, Ta_2O_5, CeO_2, and MgO using monochromated STEM EELS. Because such resonances are nanoparticle geometry specific, we refer to them as "cavity modes" herein. To illustrate the character of cavity modes in the spectra of oxide nanoparticles, we focus on TiO_2 (anatase), CeO_2, and MgO (observations from Ta_2O_5 are very similar to those from TiO_2). The effects of experimental parameters such as probe position, crystal orientation, and electron velocity

on the cavity modes are also discussed. STEM EELS, which is the electron probe analog of optical extinction (absorption + scattering) with access to full spectrum of target excitations (i.e., both "bright" and "dark" excitations), is particularly sensitive to resonances in the bandgap region where intensity from electronic transitions are small (i.e., where absorption is minimal). To interpret the complicated spectral features detected, theoretical models and numerical simulations based on classical electrodynamics are performed. With the combination of theory and experiment, the underlying physics responsible for these cavity modes is elucidated, and the various factors that affect their behavior is examined in detail.

6.3 Results and Discussion

Fig. 6.1 shows a set of EEL spectra from a STEM linescan across the surface of a 100 nm anatase nanoparticle, showing a series of pronounced peaks in the bandgap region (bandgap of 3.2 eV). The anatase nanoparticle is part of a large aggregate of particles and the surface facet is edge on to the electron beam and roughly 80 nm in length, as shown in the high-angle annular dark-field (HAADF) image in Fig. 6.1. In this line scan, the beam begins 25 nm outside of the particle and is scanned to 15 nm inside of the particle. The corresponding spectra can be categorized as either aloof or transmission, depending on if the beam is located in the vacuum or is penetrating the particle. In the aloof beam geometry, the electron beam is positioned outside the sample and the EEL signal is due to delocalized electron-solid interactions [34]. The influences of the distance from the electron beam to the crystal surface, defined as the impact parameter b (b$>$0 for aloof and b$<$0 for transmission geometries), on the aloof spectral intensity has been discussed previously in the literature [101, 64].

At 25 nm outside the particle, the EEL spectrum shows a series of small-amplitude resonances in the energy range between 0.5-3.5 eV, while the bandgap onset is 3.2 eV. As the beam approaches the particle surface, the aloof spectral intensity rises, with the peaks in the bandgap becoming most intense when the electron beam is positioned on the surface. In a defect free crystal, electronic excitations of the valence electrons into the conduction band will generate spectral intensity only in the energy-loss range above the bandgap. In this case,

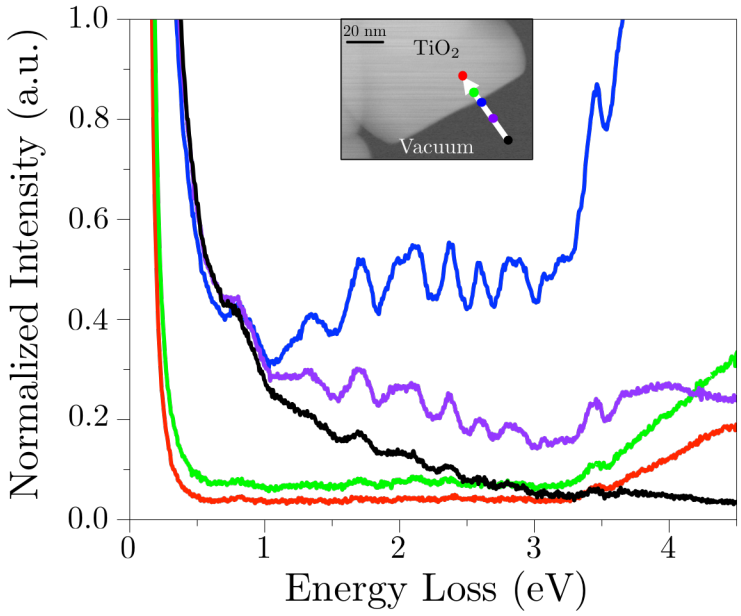

Figure 6.1: STEM EEL line scan of an anatase nanoparticle moving from vacuum to penetrating electron beam configurations as shown in the inset. The STEM acceleration voltage is 60 kV. The impact parameter corresponding to each spectrum is b=25 nm (black); b=12 nm (purple); b=0 (blue); b=-6 nm (green); b=-15 nm (red). A progression of resonances within the bandgap is clearly visible in the aloof trajectories.

numerical EELS simulation (discussed below) shows that the peaks observed in the bandgap region are characteristic of the optical cavity modes associated with the particle aggregate. This strong increase in the signal with decreasing impact parameter is expected for the aloof region of the scan [64], however, once the beam enters bulk TiO_2, a pronounced reduction in overall spectral intensity is observed. This overall intensity drop in the transmission spectra is mainly associated with elastic scattering of the incident electrons by the nanoparticle, making it difficult to directly compare the bandgap peak intensities with those in the aloof beam spectra (This comparison can be achieved in the simulations which do not include the effect of elastic scattering (Fig. 6.6) and will be discussed later). In practice, the aloof beam geometry with a rather small impact parameter seems to maximize the visibility of the spectral peaks in the bandgap region rather than the traditional transmission geometry. Therefore, for the following experiments, spot acquisitions are performed in the aloof beam configuration. Considering the cone-shape STEM electron probe and the average nanoparticle thickness (100-200 nm), the optimum impact parameter to observe the spectral signatures of cavity modes while avoiding elastic scattering contributions is 4-5 nm, although experimental measurement error and specimen drift will slightly alter the actual impact parameter used for each acquisition [101].

The behavior of the anatase nanoparticle's bandgap peaks as a function of crystal tilt and incident electron energy are shown in the experimental EEL spectra in Fig. 6.2. By tilting the nanoparticle target relative to the electron beam source, two aloof spectra are acquired with the same impact parameters near a 011 surface, when the crystal is tilted both onto and 14^o off the [100] zone axis (ZA), as shown in the Kikuchi patterns in Fig. 6.2a. Tilting the crystal onto the low order ZA ensures that the columns of atoms in the 011 surface facet are parallel to the beam trajectory, ignoring the small convergence angle. The two aloof spectra in Fig. 6.2a show no obvious difference in the peak energies, and only subtle differences in the strengths of the bandgap peaks. However, in contrast to crystal orientation, the velocity of the fast electron significantly affects the visibility of the bandgap peaks. Aloof beam spectra are displayed in Fig. 6.2b with a 4 nm impact parameter from the same anatase crystal

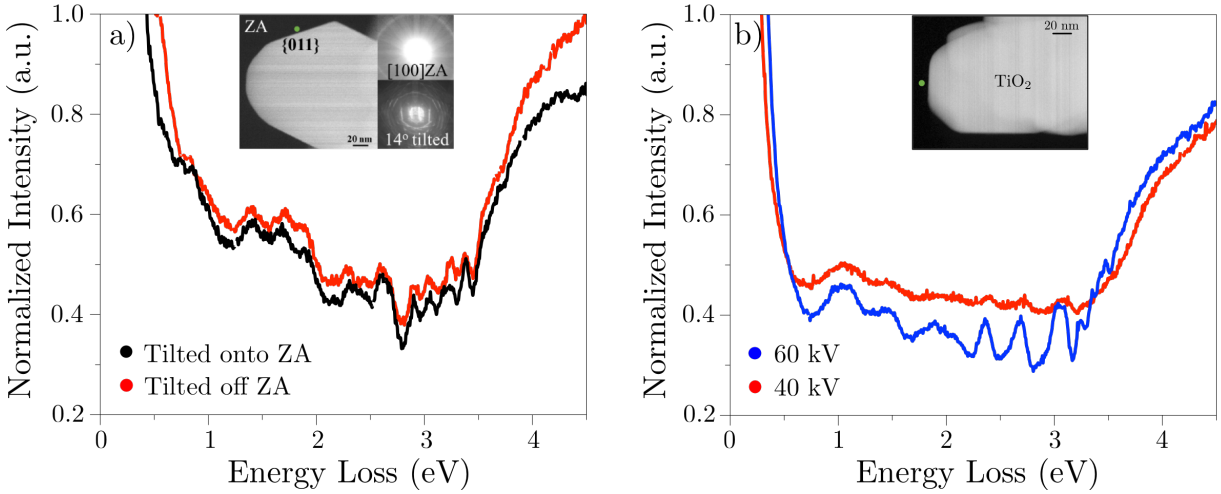

Figure 6.2: (a) Aloof EEL spectra of an anatase nanoparticle acquired at a 011 surface with the nanoparticle tilted onto (black) and 14^o off (red) the [100] ZA at 60 kV. The inset shows the HAADF image of this particle on ZA, and the two Kikuchi patterns show the particle both on and 14^o tilted from the ZA. (b) Aloof spectra of an anatase particle acquired at 40 kV (red) and 60 kV (blue). The green bullet in both insets indicate the position of the electron beam (approximately b=4 nm) used to acquire the associated spectra.

using accelerating voltages of 40 and 60 kV. The 40-kV spectrum is displayed so that the conduction band edge is well aligned with the 60-kV spectrum, facilitating comparison of the relative intensities of the bandgap peaks. Here it is evident that the visibility of the bandgap peaks is reduced at lower beam voltage (which corresponds to a 16% decrease in fast electron velocity). Also, the degree of suppression seems larger for the higher energy loss peaks.

Full-wave numerical electrodynamics simulations of the fast electron probe would aid in understanding the origin of these spectral peaks, but the commercial anatase nanoparticles studied here have complicated geometrical shapes and tend to aggregate into irregular clusters. This makes it challenging to determine their precise three-dimensional shape from the projected HAADF images, which is necessary to parametrize the calculation. However, hydrothermally synthesized CeO_2 nanoparticles exhibit a more well-defined near-cubic morphology (Fig. 6.3), with refractive indices similar to those of TiO_2 (Fig. 6.5b), and are amenable to detailed numerical simulation. Fig. 6.3 displays the aloof beam EEL spectrum of a 250 nm CeO_2 nanocube (experiment: red, simulation: black), showing peaks in the bandgap region similar

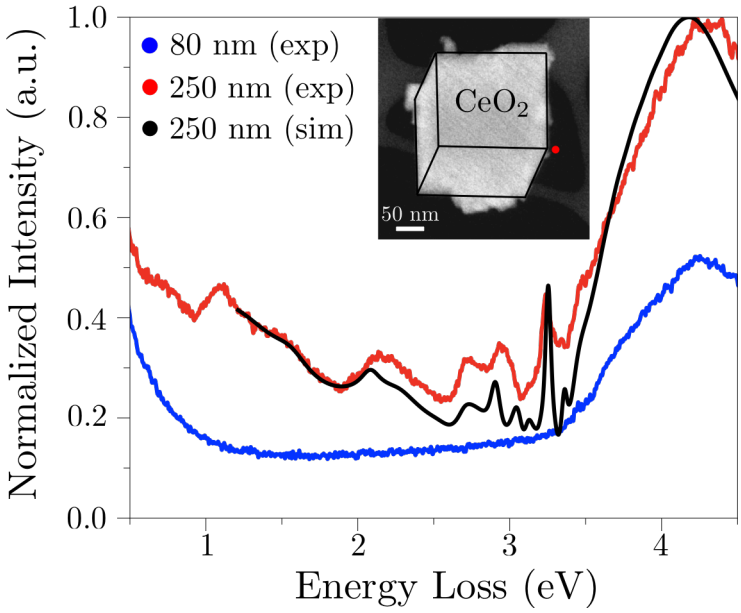

Figure 6.3: Experimental (red) and computed (black) aloof EEL spectra with the electron beam positioned 4 nm from the corner of a well-defined CeO_2 cube of 250 nm in size. The aloof beam EEL spectrum (blue) from an isolated 80 nm CeO_2 cube shows a featureless bandgap. The inset is the HAADF image of the 250 nm cube with beam position denoted by the red bullet.

to those observed in the TiO_2 particles. This particular nanocube was isolated from other large cubes, although several particles with much smaller sizes are attached to its surfaces. Due to their small sizes, these particles will not themselves generate spectral peaks in the bandgap as will be discussed, but may affect the appearance of the experimental spectrum as the overall effective shape of the specimen is altered. These complications to the overall particle shape can be approximately accounted for in simulations, using the electron-driven discrete dipole approximation (e-DDA) [18, 17], by adjusting the nanocube edge length and tilting. A simple power law background intensity is also added to the simulation to account for the tail of the zero-loss peak in the experimental spectrum, which is not included in e-DDA. This produces good agreement between experimental and the simulated aloof EEL spectra. The small discrepancies in the peak energies and strengths between simulation and experiment may be due to inaccuracies in the CeO_2 dielectric data from the literature and an incomplete description of the specimen's morphology. This result shows that the bandgap

peaks observed in the EEL spectra can also be studied numerically if the specimen geometry and dielectric are known.

To develop a deeper understanding of the physical origin of the bandgap peaks and to confirm that they are indeed induced by cavity mode resonances, we turn to Mie theory which provides an analytic framework that exactly describes the inelastic scattering of photons/electrons by a dielectric sphere. While idealized, the energy transfer or losses from light/electron to an oxide nanosphere are qualitatively similar to those of a correspondingly sized oxide nanocube of the same composition, meaning that analytic analysis on the nanosphere provides an understanding of the spectral features of the nanocube.

Recall that the familiar Mie cross section for light scattering by a dielectric sphere of radius r is [22]:

$$\sigma_{sca}(\omega) = \frac{2\pi c^2}{\omega^2} \sum_{\ell=1}^{\infty} (2\ell + 1) \left(|a_\ell|^2 + |b_\ell|^2 \right) \tag{6.1}$$

expressed in terms of the Mie coefficients

$$\begin{aligned} a_\ell =& \frac{n^2 j_\ell(nx)[x j_\ell(x)]' - j_\ell(x)[nx j_\ell(nx)]'}{n^2 j_\ell(nx)[x h_\ell^{(1)}(x)]' - h_\ell^{(1)}(x)[nx j_\ell(nx)]'} \\ b_\ell =& \frac{x j_\ell(nx) j_\ell'(x) - nx j_\ell(x) j_\ell'(nx)}{x j_\ell(nx) h_\ell^{(1)'}(x) - nx h_\ell^{(1)}(x) j_\ell'(nx)} \end{aligned} \tag{6.2}$$

where n is the refractive index and $x = kr = 2\pi r/\lambda = \omega r/c$. It is the denominators of a_ℓ and b_ℓ that encode the resonant frequencies ω of the target as zeros. Such poles are parametrically dependent upon both the target index of refraction and the ratio of nanosphere radius r to wavelength λ. In dispersive regions of the spectrum, e.g., for noble metals in the visible regime, it is these poles that encode the spectral locations of the surface plasmon resonances of the sphere. However, in the case of Ce, Ti, and Mg oxides, the dielectric function is real-valued and nearly constant below the bandgap. This means that absorption is negligible and scattering, if finite, is not due to either individual or collective electronic transitions. Analysis of the behavior of the spherical Bessel and Hankel functions j_l and h_l at

the roots of the Mie coefficient denominators demonstrates that the spectral peaks within the bandgap region correspond approximately to the situation where an integer multiple of half wavelengths "fit" within the nanosphere. This analytical observation justifies the physical picture of these scattering features as geometric cavity resonances.

However, our experimental observations do not involve elastic light scattering but rather inelastic electron scattering via EELS. Fortunately, Mie theory can be applied equally to both optical and electron beam sources [47], and in the case where the sphere's refractive index is real-valued there is a simple relationship between the two observables. Specifically, the EEL probability per unit of transferred energy is

$$\Gamma^{\mathrm{EELS}}(\omega) = \frac{e^2}{c\omega\hbar^2} \sum_{\ell=1}^{\infty} \sum_{m=-\ell}^{\ell} K_m^2 \left(\frac{\omega b}{v\gamma}\right) \left(C_{\ell m}^A \mathrm{Im}\{a_\ell^{\mathrm{EELS}}\} + C_{\ell m}^B \mathrm{Im}\{b_\ell^{\mathrm{EELS}}\}\right) \tag{6.3}$$

where K_m is a modified Bessel function of the second kind, γ is the relativistic Lorentz contraction factor, $C_{\ell m}^A$ and $C_{\ell m}^B$ are velocity dependent but frequency independent coefficients, and $a_\ell^{\mathrm{EELS}} = ia_\ell$ and $b_\ell^{\mathrm{EELS}} = ib_\ell$ are the EELS Mie coefficients, which are simply connected to those involved in light scattering. While not obvious, when the refractive index is real-valued, $\mathrm{Im}\{a_\ell^{\mathrm{EELS}}\} = |a_\ell|^2$ and $\mathrm{Im}\{b_\ell^{\mathrm{EELS}}\} = |b_\ell|^2$, meaning that both $\Gamma^{\mathrm{EELS}}(\omega)$ and $\sigma_{sca}(\omega)$ have the same pole structure. This makes explicit the fact that EELS is a local measure of extinction, with extinction being equivalent to scattering since absorption is zero in this case.

Fig. 6.4 shows the correlation between the induced electric field distribution (calculated using e-DDA) in a 160 nm CeO_2 particle and the bandgap peaks in the EEL and optical scattering spectra. The electric field distributions are consistent with standing electromagnetic waves of different wavelength within the nanoparticle. The low energy peak at 2.37 eV corresponds to a wavelength of roughly double the particle size and the 3.22 eV peak corresponds to a wavelength of roughly the same size as the particle. Taken together, this analysis shows that the EEL bandgap peaks are precisely those geometric cavity modes emerging in light scattering.

Fig. 6.5 displays a series of EELS simulations of oxide nanocubes showing the effects of

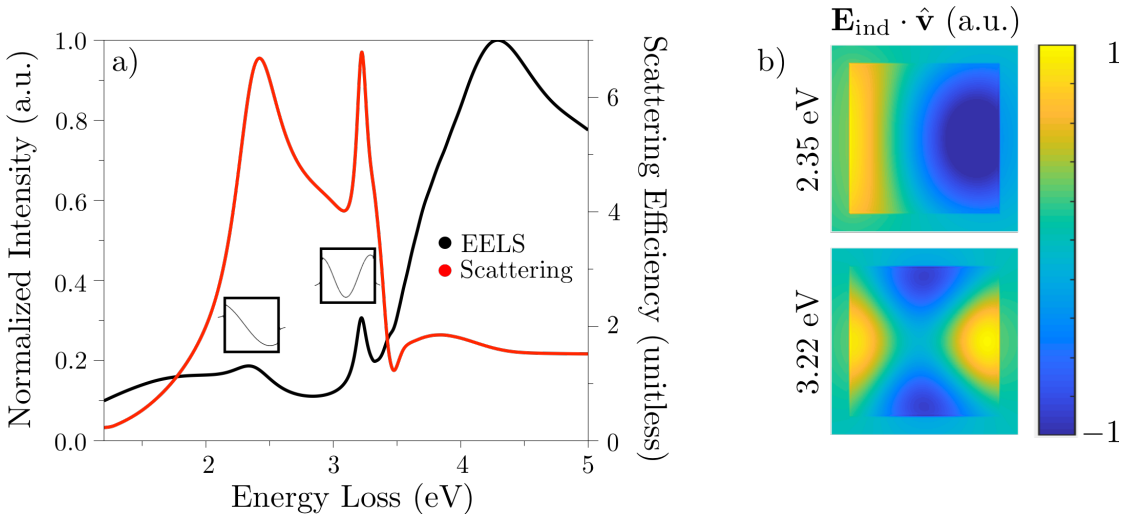

Figure 6.4: (a) Simulated aloof EEL (black) and optical scattering (red) spectra of a 160 nm CeO_2 nanocube. The 60 kV electron beam is parallel to the cube surface in the aloof beam geometry, and the polarized plane-wave light field is normal to the cube surface. The two insets display the electric field intensity profiles within the cube at the band-gap resonances. (b) The field maps show the electron-driven electric field distributions associated with the cavity modes at 2.37 eV (top) and 3.22 eV (bottom).

refractive index, beam position, electron velocity, particle size, and aggregation scheme on the formation of cavity modes. Fig. 6.5a compares the simulated EEL spectra of individual TiO_2 and CeO_2 nanocubes, both 160 nm in size (the smaller particle size simplifies the spectrum by reducing the number of peaks in the bandgap). In both spectra, the electron beam is positioned at a low symmetry point outside of the particle with a 4 nm impact parameter (indicated in Fig. 6.5a, inset). The simulated spectral features below 3.5 eV from TiO_2 and CeO_2 are quite similar, except for a small blue shift in the peak positions in the CeO_2 spectrum. The similarity of the spectra correlates with the similarity in the energy-dependent refractive indices of CeO_2 and TiO_2 (Fig. 6.5b). This implies that the optical responses in the bandgap region of these two materials will be very similar if their geometrical shapes are the same.

To further illustrate the effect of refractive index (Fig. 6.5b) on cavity modes in oxide nanoparticles, the aloof spectrum of a 160 nm MgO nanocube is also simulated in Fig. 6.5a, as

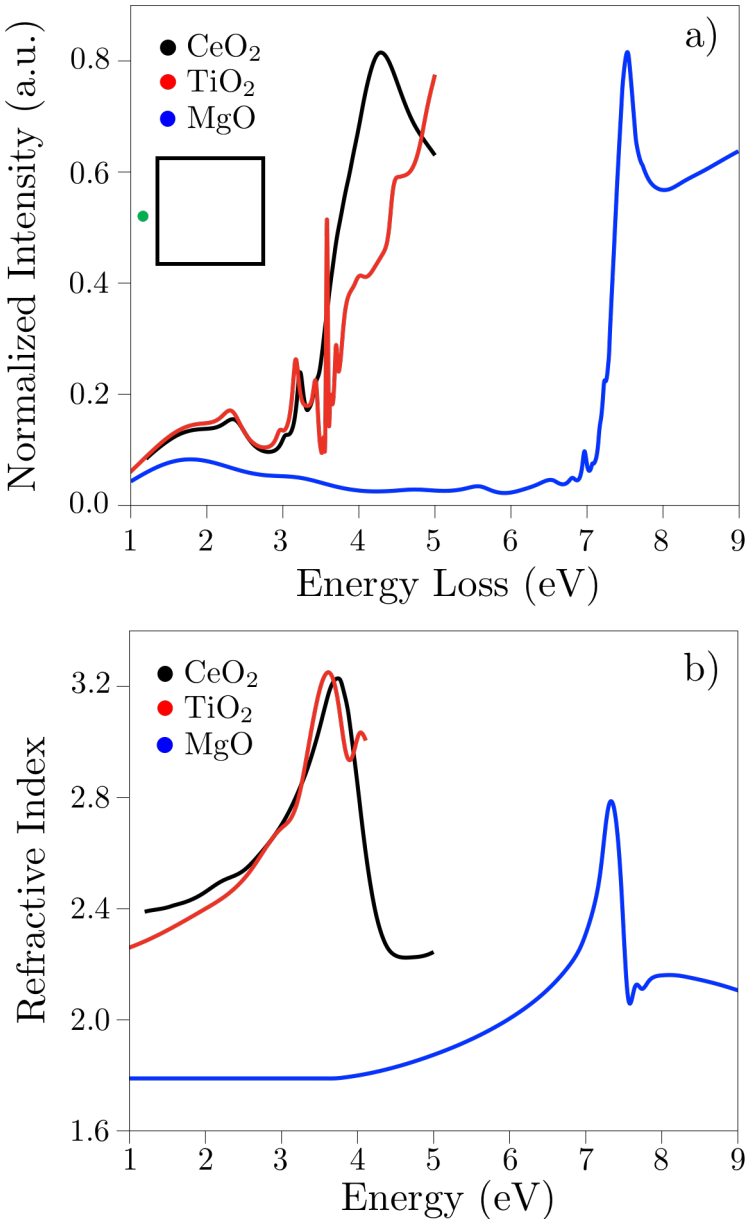

Figure 6.5: (a) Calculated aloof EEL spectra of TiO_2, CeO_2 and MgO cubes with the same edge length (160 nm). In each spectrum, the electron beam is positioned at b=4 nm outside of the nanoparticle surface at a low symmetry point denoted by the green dot shown in the inset. (b) The real-valued component of the energy dependent refractive indices of the three materials.

MgO represents a material with much smaller refractive index compared to ceria. All spectra are normalized so that the EEL intensities are approximately equal above the band gap. In the MgO spectrum, a gentler intensity variation in the bandgap region (< 7.3 eV) is displayed. This behavior is expected based on Mie analysis, where the geometric resonance conditions in similarly-sized nanoparticles composed of materials of low refractive index are only satisfied at EEL energies just below the band edge. This agrees with our experimental observation from MgO where sharp EELS peaks within the bandgap region are not observed[101].

In addition, Fig. 6.6 shows the simulated EEL spectrum of a 160 nm CeO_2 nanocube's cavity mode resonances as a function of electron beam position, demonstrating that cavity modes are best excited in the aloof beam configuration (b = +4 nm from the cube surface, black). Alternatively, excitation of CeO_2 electrons from valence to conduction band is most efficient when the electron beam is positioned to penetrate the nanocube as evidenced by the larger EEL intensities after the bandgap onset (b = -4 nm from the cube surface, red; b = -69 nm from the cube surface, blue). Variation of the CeO_2 nanocube size (l = 80 nm and 160 nm) and electron beam acceleration voltage is explored in Fig. 6.7, using electron voltages ranging from 20-100 kV, corresponding to electron velocities of (0.27-0.55)c, where c is the velocity of light in vacuum. Consistent with experiment (Fig. 6.3), the 80 nm nanocube does not support cavity mode resonances within the bandgap for any of the accelerating voltages considered while the 160 nm nanocube shows an increasing probability for excitation of cavity modes with increasing acceleration voltage (i.e., electron kinetic energy). In both cases the intensity of the electronic excitation of the valence electrons decreases with increasing electron velocity as the inelastic scattering probability is inversely related to electron velocity[40, 64].

The hybridization of geometric resonances in photonic crystals [103, 104] and chains of dielectric particles [19] is now well understood and has been measured using a variety of optical characterization techniques. Here we explore the effect of coupling between neighboring oxide nanoparticles in EEL spectroscopy using e-DDA. Fig. 6.8a compares the EEL spectrum of a CeO_2 nanocube dimer (red) to that of a monomer (black). A pronounced splitting of the monomer cavity resonance near 3.2 eV is observed in the dimer spectrum, indicative of

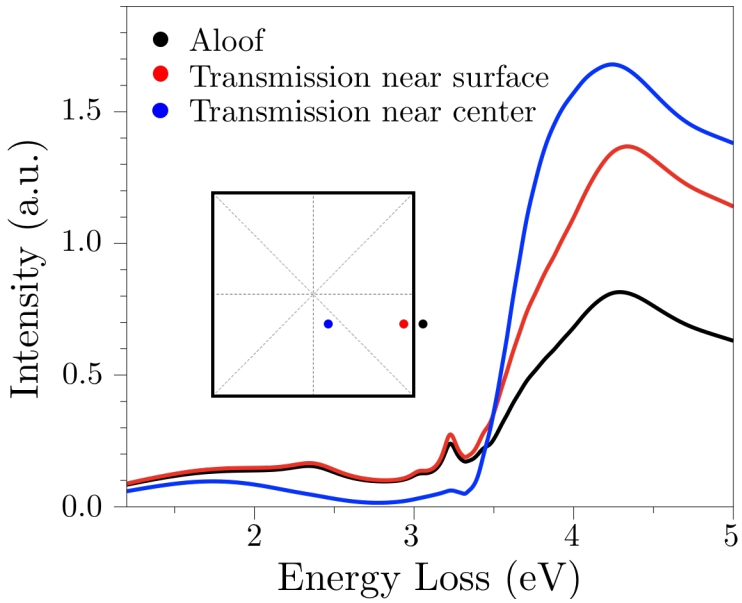

Figure 6.6: Calculated EEL spectra from three beam positions for a 160 nm CeO_2 cube with 60 kV incident electrons. The inset displays the 2D projection of cube with the three low symmetry beam positions (colored bullets) when looking down the beam direction. Dashed lines represent the mirror planes of the cube.

hybridization into symmetric and antisymmetric standing waves spanning the dimer cavity. The 1D and 2D spatial dependencies of the lower and higher energy cavity modes are illustrated in panels b) and c) of Fig. 6.8. In both cases the component of the induced electric cavity resonance along the electron beam trajectory ($\hat{\mathbf{v}}$) is plotted, clearly demonstrating cavity mode hybridization. Such understanding is useful in the interpretation of small nanoparticle aggregates such as in our original investigations of anatase nanoparticles, which will be revisited in a future publication.

Based on our Mie analysis and full-wave numerical electrodynamics simulations of the electron probe, excitation of cavity modes in a dielectric particle can be viewed as an inelastic scattering process where the fast electron's super-continuum evanescent field couples resonantly into the geometry- and refractive-index specific standing wave resonances of the particle. It is well known that electrons interacting with dielectric particles may lose energy via the generation of light. An electron in uniform motion generates electromagnetic field components

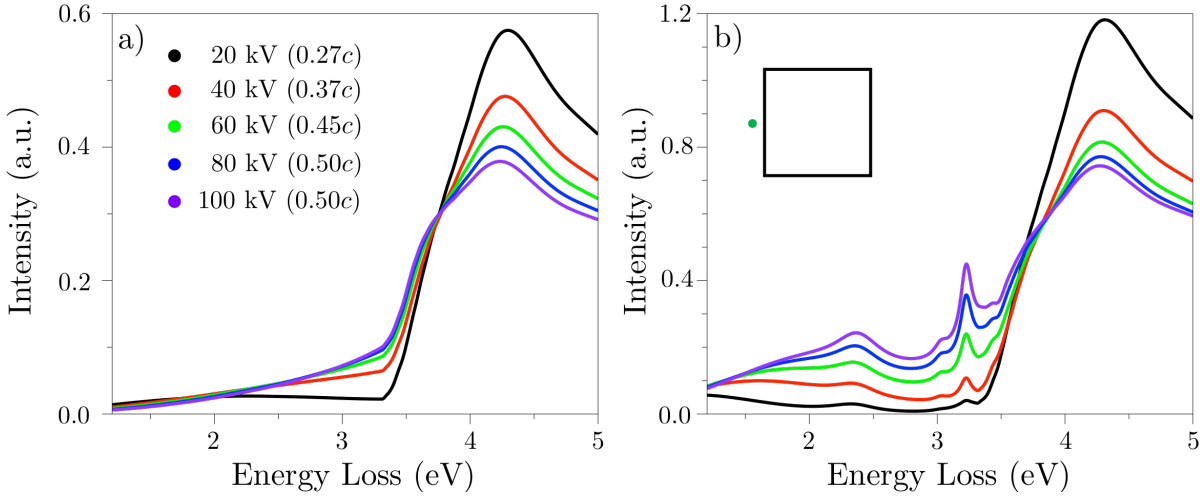

Figure 6.7: Calculated aloof EEL spectra from CeO_2 cubes of two different particle sizes, (a) 80 and (b) 160 nm, at 5 different electron beam acceleration voltages. In each spectrum, the electron beam is positioned at b=4 nm in the aloof configuration as shown by the green dot in the inset.

that are both parallel and perpendicular to the electron velocity with a broad frequency spectrum [161, 46]. These evanescent field components (often referred to as virtual photons) can be converted to propagating radiation fields through different energy loss mechanisms, with the two most common being transition radiation and Cherenkov radiation. Transition radiation, or transition scattering, occurs when a charge uniformly moves in or near an optically inhomogeneous medium in space [51]. Sometimes the situation where an electron passes a localized inhomogeneity in a medium is also called diffraction radiation [122]. Unlike Cherenkov radiation, this phenomenon is expected at any electron speed [121]. Diffraction radiation was observed from relatively large Al2O3 spheres, where inelastic signals were found in the bandgap region of this material. It was argued that the observed energy losses originated from the oscillating polarization charges in the material, induced by the passing electron [1, 46]. These transition radiation losses may always be present in the bandgap region of the spectrum even when peaks are not pronounced (see for example the spectra from smaller particles of CeO_2 in Fig 6.3 and Fig 6.7a). The resonant modes of the particle appear to modulate the transition radiation contribution to the energy-loss spectrum.

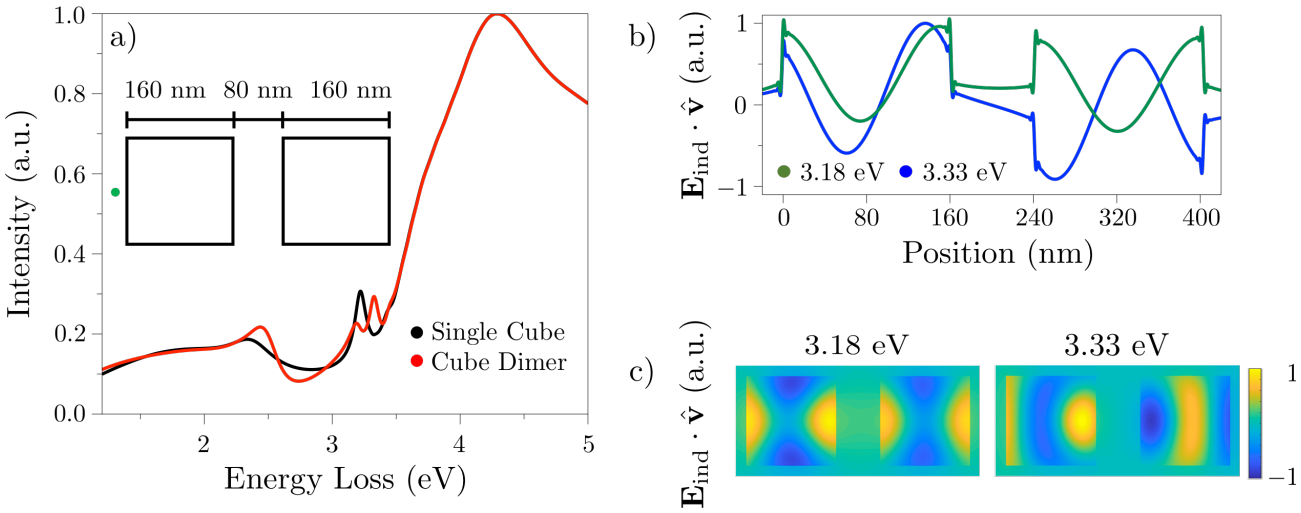

Figure 6.8: a) Calculated aloof EEL spectra of a CeO_2 nanocube dimer (red) and monomer (black) showing the signature of cavity mode hybridization in the splitting of resonance peaks around 3.2 eV. The edge length of each nanocube is 160 nm. Panels b),c) display the projected electric field profiles of the hybridized cavity modes observed in the spectrum in panel a). The lower and higher energy modes correspond to the in-phase and out-of-phase hybridized geometric resonances of the dimer.

It is less clear if Cherenkov radiation makes a significant contribution to the spectrum when the electron energy exceeds the Cherenkov threshold. Cherenkov radiation is the electromagnetic shock wave that may be produced when the electron passes through a material at a velocity greater than the speed of light in that material [46]. For semiconductors, it occurs mainly in the bandgap region of the spectrum where negligible absorption occurs, with the energy radiated increasing with increasing electron velocity and material refractive index [69]. In thin films, the strength of the Cherenkov loss in the EEL spectrum decreases with decreasing sample thickness due to damping [143]. Within the bandgap (i.e, below 3.4 eV), the refractive indices for CeO_2 and TiO_2 are in the range of 2.2-3.2, both satisfying the Cherenkov threshold of 2.24 for a 60 kV beam. For the aloof mode geometry, a Cherenkov effect would presumably be a result of the motion of a traveling image charge in the nanoparticle that is associated with the passage of the fast electron outside.

Certainly, the experimental spectra of Fig 6.2b show a pronounced increase in the visibility of the cavity modes when the Cherenkov threshold is exceeded. However, caution much be

exercised in the interpretation of this observation. Eqn 6.3 shows that the strength of the cavity mode loss depends on the square of the K_m. Bessel function. For constant impact parameter, the argument of the Bessel function, $(\omega b/v\gamma)$, increases when the electron velocity decreases. Since the Bessel function decays quickly with increasing argument, this will significantly attenuate the oscillations from the cavity modes. The calculation in Fig. 6.7b shows a steady increase in the cavity modes strength with no obvious turn-on effect when the electron energy exceeds the Cherenkov threshold. Both the experiment and the simulations suggest that Cherenkov effects may not be important at least for the oxide nanoparticle investigated here.

6.4 Conclusion

We have observed resonant photonic modes in individual and few-particle assemblies of MgO, TiO_2 and CeO_2 nanoparticles using the nanometer dimension electron beam in a monochromated STEM. The modes appear as a progression of spectral peaks within the bandgap region of EELS (where energy absorption is negligible) from relatively large nanoparticles. Full-wave electrodynamics simulations combined with analytic Mie analysis of the electron probe facilitate the interpretation and understanding of the physical origin of these spectral features. The peaks result from the excitations of geometric resonance modes, or cavity modes, in the dielectric particles and are most clearly visible when the fast electron beam is near the particle surface. This resonance behavior is found to be encoded in the scattering properties of the oxide particles when exposed to either electrons or light. The energies and shapes of the cavity modes are determined by the size, geometry, and complex-valued dielectric function of the oxide. Oxides with relatively small refractive index or small particle size ($<$ 100 nm) show no obvious cavity mode excitation. The strength of the coupling between the cavity mode and the fast electron beam is determined by the probe position. By varying the position of the electron beam, different modes may be selectively excited with the strength of the resonance showing a strong positive dependence upon the fast electron velocity. The emergence of hybridized cavity modes in oxide nanoparticle dimers is also predicted based

upon simulation. Taken together, our work demonstrates the unique ability of STEM EELS to resolve the photonic density of states in individual and ensembles of dielectric nanoparticles.

6.5 Materials and Methods

Commercial TiO_2 anatase particles (99.8%) were purchased from Sigma-Aldrich. CeO_2 nanocubes with predominantly {100} surfaces were hydrothermally synthesized following a recipe described elsewhere [157, 156]. The TiO_2 nanoparticles were dispersed onto TEM sample grids (holey carbon film) using a dry preparation method. For CeO_2 nanocubes, in order to maximize the possibility of finding isolated cubes, the powders were first ground and dispersed in de-ionized water then ultrasoniced for 15 min. Dispersion from the top layer of solution was drop cast onto a TEM grid to prepare a sample with isolated CeO_2 cubes.

An aberration-corrected NION UltraSTEM 100 microscope coupled with a monochromator and a Gatan Enfinium spectrometer was employed to acquire all the spectra. The microscope was operated at 60 and 40 kV with an energy dispersion of 5 meV per channel. Full width half maximum (FWHM) of the zero-loss peak was better than 25 meV. Convergence and collection semi-angles were 30 mrad and 15 mrad respectively with a 1 mm spectrometer entrance aperture. Gatan Digital Micrograph software was used to process the data. Both EELS line scans and spot acquisitions were performed, where 40 - 50 s acquisition time was used for each spectrum to improve signal-to-noise ratio.

Our numerical methods are based upon the coupled-dipole [124] or discrete dipole approximation (DDA) approach [39], which have been routinely used to model the response of plasmonic nanoparticles to plane wave radiation. As a generalization of these ideas, here we use our previously developed electron-driven discrete dipole approximation (e-DDA) [18, 17] to model the STEM electron beam and its interaction with the target specimen. The nanoparticles under study were modeled as perfect cubes, with an inter-dipole spacing chosen to ensure convergence. The dielectric data for each material was taken from the literature (TiO_2 from [86], CeO_2 from [70], MgO from [130])

Chapter 7

CONCLUSION

This body of work aims to expand the understanding of EELS and the wealth of information it can provide when applied to single nanoparticles and single aggregates of nanoparticles. A general theory describing the EELS experiment was provided for systems of MNPs in the quasistatic limit and for arbitrary nanoparticles when accounting for retardation effects. The nature of EELS differs from that of optical absorption due to the relativistic electron holding an evanescent electric field, allowing for selection rules to be imposed on a system by the selection of a beam position. The power of this attribute is explored in chapters 3-5 on MNP dimers and small aggregates, the plasmonic modes of which were rigorously mapped onto harmonic oscillators with generalized plasmonic coordinates.

It was originally believed that EELS was blind to Fano resonances [88]. The ability of EELS and CL to display interferences of this nature was shown through an analytic treatment of coupled MNP dimers. In the case of EELS, "bright" and "dark" modes do not hold their conventional meaning due to the highly localized character of the electron's electric field. This allows for modes near the electron to be considered "bright" for appropriate impact parameters and "dark" for impact parameters that are either far from the nanoparticle or positioned in a way that will not drive the mode. Contrary to optical absorption, Fano interferences were observed in EELS and CL for not only dipole-quadrupole interactions but dipole-dipole interactions as well. The theoretical framework describing EELS and CL results in the Fano factor of a MNP dimer holding the same form as observed in optical absorption [148].

The selection rules imposed by the electron can be extended outside of the individual mode picture, imposing selection rules on the normal modes of a system. The EELS expression for the

MNP dimer was transformed into normal mode coordinates, using a squeezing transformation and a rotation in succession. This allowed for two uncoupled oscillator equations to be used to described the in-phase and out-of-phase normal modes for the dimer. This treatment also transformed the force from acting on the individual nanoparticles to acting on the normal modes of the system. Analysis of this force and when the electron was unable to force normal modes allowed for imaging hybridized modes in EEL maps through the emergence of spatially dependent nodal structure. This treatment allowed for the determination of the relative phase of dipoles between two particles.

This analysis was extended beyond the case of a MNP dimer to that of a magnetic oligomer dimer. These so-called magnetic plasmons are the result of oscillating current loops, which were modelled and experimentally verified to exhibit the nodal structure in EEL maps as outlined in the case of the dimer. This system was explored further by breaking the symmetry of the two rings, allowing interferences to arise due to the superposition of magnetic modes. This localized the magnetic field to either the small ring or large ring depending on the energy of excitation. This was the first experimental observation of this Fano-like interference between two magnetic modes of magnetic oligomer systems.

The material from chapter 6 explored a different type of resonance than those normally associated with EELS. Typically in EELS peaks arise due to electronic excitations (excitons, plasmons, etc.), however resonances were observed in the band gap of semiconductor nanoparticles in EELS experiments. This behavior is not present when considering particles in the quasistatic limit and required a more rigorous treatment in which retardation effects were included. In the case of a real valued dielectric function, such as the properties in the band gap of semiconductors and insulators, the resonance structure in EELS observed in the EELS Mie coefficients is identical to the dependence in optical scattering. This lends credence to geometric cavity modes observed in EELS that are analogous to geometric scattering of nanoparticles. This property occurs for either larger particles, or small particles that hold a sufficiently large dielectric constant in the band gap. This result requires precautions to be taken when studying systems that introduce states in the band gap such as surface ligation.

Appendix A
GREEN'S FUNCTIONS

The Green's function is the fundamental solution for a inhomogenous partial differential equation

$$\begin{aligned} \hat{D}f(\mathbf{x}) =& h(\mathbf{x}) \\ \hat{D}G(\mathbf{x},\mathbf{x}') =& \delta(\mathbf{x}-\mathbf{x}') \end{aligned} \tag{A.1}$$

where $\hat{D}$ is a differential operator and $h(\mathbf{x})$ is a source for $f(\mathbf{x})$. In the context of electromagnetism the source may be a charge or current distribution to the potential of electric/magnetic field. The Green's function effectively eliminates the differential operator, allowing for the particular solution $f(\mathbf{x})$ to be determined by integrating the source over all space with the Green's function as a kernel

$$f(\mathbf{x}) = \int \mathrm{d}\mathbf{x}'\ G(\mathbf{x},\mathbf{x}')h(\mathbf{x}') \tag{A.2}$$

If one were to act the differential operator on both sides of this expression, we obtain

$$h(\mathbf{x}) = \int \mathrm{d}\mathbf{x}'\ \delta(\mathbf{x}-\mathbf{x}')h(\mathbf{x}') \tag{A.3}$$

A.1 Scalar Green's Functions

The treatment of nanoparticles and their interaction with electric fields can be approached in a variety of ways, one method utilizing a generalization of Gauss's law. Gauss's law provides a wealth of information regarding electric fields originating from a charge distribution. The most basic distribution is a single point charge, represented by a delta function in space. Any

arbitrary charge distribution can be built from a combination of these point charges, allowing for a general solution for Gauss's law. One drawback to this approach is it does not take into account finite times for information to propagate and therefore is an approximation known as the quasistatic approximation. Two cases will be considered in the approach: External and internal charge distributions.

A.1.1 External Charge Distribution

Gauss's law can be written for an external point charge where a spherical boundary is considered. The point particle is represented by a delta function in space and two equations can be written for the two regions of space

$$\begin{aligned} r > a: \quad & -\epsilon_b \nabla^2 G(\mathbf{r}, \mathbf{r}'; \omega) = 4\pi\delta(\mathbf{r} - \mathbf{r}') \\ r < a: & -\epsilon(\omega)\nabla^2 G(\mathbf{r}, \mathbf{r}'; \omega) = 0 \end{aligned} \tag{A.4}$$

where a is the radius of the sphere and $G(\mathbf{r}, \mathbf{r}'; \omega)$ is the Green's function in the Fourier domain which is related to the electric potential through integration with the external charge distribution. A few assumptions have been made regarding these equations: 1) The dielectric function is spatially uniform in each region. 2) The nanoparticle is charge neutral. The general approach to this problem starts with expanding the delta function in a basis well suited to describe the dielectric boundary. For a sphere, this is

$$\delta(\mathbf{r} - \mathbf{r}') = \frac{\delta(r - r')}{r^2} \sum_{\ell=0}^{\infty} \sum_{-\ell}^{\ell} Y_{\ell m}(\theta, \phi) Y^*_{\ell m}(\theta', \phi') \tag{A.5}$$

Further evaluation of this problem requires boundary conditions for the nanoparticle surface and the location of the point particle. The boundary conditions for the Green's function are:

At the surface ($r = a$)

1) G is continuous

2) $\left[-\epsilon_b \frac{\partial}{\partial r} G(\mathbf{r}, \mathbf{r}'; \omega)\right]_{r=a+} = \left[-\epsilon(\omega) \frac{\partial}{\partial r} G(\mathbf{r}, \mathbf{r}'; \omega)\right]_{r=a-}$

At the point charge ($r = r'$)

1) G is continuous

2) $\left[-\epsilon_b r^2 \frac{\partial}{\partial r} G(\mathbf{r}, \mathbf{r}'; \omega)\right]_{r=r'-}^{r=r'+} = 4\pi \sum_{\ell=0}^{\infty} \sum_{m=-\ell}^{\ell} Y_{\ell m}(\theta, \phi) Y_{\ell m}^*(\theta', \phi')$.

which are equivalent to the usual boundary conditions for macroscopic Maxwell's equations in which the potential is continuous everywhere and the normal component of the displacement field is continuous across a surface and discontinuous across unbound charge. The Green's function can now be solved for, yielding

$$
\begin{aligned}
r > a : G_{\text{ext}}(\mathbf{r}, \mathbf{r}'; \omega) =& \frac{1}{\epsilon_b \left|\mathbf{r} - \mathbf{r}'\right|} - \frac{1}{\epsilon_b} \sum_{\ell=0}^{\infty} \sum_{m=-\ell}^{\ell} \frac{4\pi}{2\ell + 1} \frac{\ell(\epsilon(\omega) - \epsilon_b)}{\ell(\epsilon(\omega) + \epsilon_b) \ + \epsilon_b} \frac{a^{2\ell+1}}{r^{\ell+1} r'^{\ell+1}} Y_{\ell m}(\theta, \phi) Y_{\ell m}^*(\theta', \phi') \\
r < a : G_{\text{int}}(\mathbf{r}, \mathbf{r}'; \omega) =& \frac{1}{\epsilon_b} \sum_{\ell=0}^{\infty} \sum_{m=-\ell}^{\ell} \frac{4\pi}{\ell(\epsilon(\omega) + \epsilon_b) \ + \epsilon_b} \frac{r^{\ell}}{r'^{\ell+1}} Y_{\ell m}(\theta, \phi) Y_{\ell m}^*(\theta', \phi').
\end{aligned}
\tag{A.6}
$$

The first term in the external Green's function corresponds to the potential for a charge in the absence of a dielectric boundary, while the second term in this expression corresponds to the induced potential due to the sphere polarized by the external charge. In this second term, the potential is expanded in an appropriate basis for the geometry under consideration and contains all of the resonance information due to the dielectric boundary. The dynamics and resonance information is completely contained in the surface response function of the dielectric body

$$
\tilde{g}_{\ell}(\omega) = \frac{1}{\epsilon_b} \frac{\ell(\epsilon(\omega) - \epsilon_b)}{\ell(\epsilon(\omega) + \epsilon_b) \ + \epsilon_b} \tag{A.7}
$$

and is trivially related to the polarizability of the dielectric object. The internal Green's function gives insight to the potential inside of the sphere but is of less importance when considering EELS.

A.1.2 Internal Charge Distribution

A similar approach is taken for the case of an internal charge distribution. The equations of interest are now

$$\begin{aligned} r > a: \quad -\epsilon_b \nabla^2 G(\mathbf{r}, \mathbf{r}'; \omega) &= 0 \\ r < a: -\epsilon(\omega) \nabla^2 G(\mathbf{r}, \mathbf{r}'; \omega) &= 4\pi \delta(\mathbf{r} - \mathbf{r}') \end{aligned} \tag{A.8}$$

These equations are solved yet again with the same boundary conditions

At the surface ($r = a$)

1) G is continuous

2) $\left[-\epsilon_b \frac{\partial}{\partial r} G(\mathbf{r}, \mathbf{r}'; \omega)\right]_{r=a+} = \left[-\epsilon(\omega) \frac{\partial}{\partial r} G(\mathbf{r}, \mathbf{r}'; \omega)\right]_{r=a-}$

At the point charge ($r = r'$)

1) G is continuous

2) $\left[-\epsilon_b r^2 \frac{\partial}{\partial r} G(\mathbf{r}, \mathbf{r}'; \omega)\right]_{r=r'-}^{r=r'+} = 4\pi \sum_{\ell=0}^{\infty} \sum_{m=-\ell}^{\ell} Y_{\ell m}(\theta, \phi) Y^*_{\ell m}(\theta', \phi')$.

$$\begin{aligned} r > a: G_{\text{ext}}(\mathbf{r}, \mathbf{r}'; \omega) &= \frac{1}{\epsilon_b |\mathbf{r} - \mathbf{r}'|} - \frac{1}{\epsilon_b} \sum_{\ell=0}^{\infty} \sum_{m=-\ell}^{\ell} \frac{4\pi}{2\ell + 1} \frac{\ell(\epsilon(\omega) - \epsilon_b)}{\ell(\epsilon(\omega) + \epsilon_b) \ + \epsilon_b} \frac{a^{2\ell+1}}{r^{\ell+1} r'^{\ell+1}} Y_{\ell m}(\theta, \phi) Y^*_{\ell m}(\theta', \phi') \\ r < a: G_{\text{int}}(\mathbf{r}, \mathbf{r}'; \omega) &= \frac{1}{\epsilon_b} \sum_{\ell=0}^{\infty} \sum_{m=-\ell}^{\ell} \frac{4\pi}{\ell(\epsilon(\omega) + \epsilon_b) \ + \epsilon_b} \frac{r^\ell}{r'^{\ell+1}} Y_{\ell m}(\theta, \phi) Y^*_{\ell m}(\theta', \phi'). \end{aligned} \tag{A.9}$$

A.2 Dyadic Green's Functions

Dyadic Green's functions were first used by Julian Schwinger in the 1940's to treat boundary value problems in electrodynamics. This elegant method is used for solving the vector wave/Helmholtz equation for electric and magnetic fields, allowing for a system to be solved for for any arbitrary source. For the purposes of this document the Dyadic Green's function is used to determine the resulting electric field due to current density attributed to a swift

electron. In this section, the details of solving for this are covered following methods outlined in [145].

The dyadic Green's function satisfies the following vector Helmholtz equation

$$\nabla \times \left(\nabla \times \overline{\mathbf{G}}(\mathbf{r}, \mathbf{r}', \omega)\right) - k^2 \overline{\mathbf{G}}(\mathbf{r}, \mathbf{r}', \omega) = \mathbb{1}\delta(\mathbf{r} - \mathbf{r}'). \tag{A.10}$$

This equation is rather general and has solutions that can represented in a multitude of ways. It is most useful to employ a basis well suited to the geometry of the problem and is a solution to the homogeneous vector Helmholtz equation. For our purpose, spherical basis vectors are used. We can expand the delta function in vector spherical harmonics

$$\begin{aligned} \mathbf{M}_{\substack{e\\o}\ell m} =& \nabla \times \hat{r}\psi_{\substack{e\\o}\ell m} \\ \mathbf{N}_{\substack{e\\o}\ell m} =& \frac{1}{k}\nabla \times \mathbf{M}_{\substack{e\\o}\ell m} \end{aligned} \tag{A.11}$$

where e and o stand for even and odd, in reference to the azimuthal parity, and ℓ and m are angular momentum orders. The scalar function $\psi_{\substack{e\\o}\ell m}$ is the solution to the homogeneous scalar Helmholtz equation

$$\begin{aligned} (\nabla^2 + k^2)\psi_{\substack{e\\o}\ell m} &= 0 \\ \Rightarrow \psi_{\substack{e\\o}\ell m} &= z_\ell(kr) P_\ell^m(\cos\theta)^{\cos}_{\sin} m\phi, \end{aligned} \tag{A.12}$$

where z_ℓ can either be spherical Bessel functions of the first kind, j_ℓ or spherical Hankel functions of the first kind, $h_\ell^{(1)}$, depending on boundary conditions. This allows us to expand the delta function in terms of vector spherical harmonics

$$\delta(\mathbf{r} - \mathbf{r}')\mathbb{1} = \int_0^\infty \mathrm{d}k \sum_{\ell=0}^{\infty} \sum_{m=0}^{\ell} \left[\mathbf{M}_{\substack{e\\o}\ell m}(k)\mathbf{A}_{\substack{e\\o}\ell m} + \mathbf{N}_{\substack{e\\o}\ell m}(k)\mathbf{B}_{\substack{e\\o}\ell m}\right] \tag{A.13}$$

where $\mathbf{A}_{\substack{e\\o}\ell m}$ and $\mathbf{B}_{\substack{e\\o}\ell m}$ are unknown expansion coefficients. These are readily solved for by taking the anterior scalar product with $\mathbf{M}_{\substack{e\\o}\ell' m'}(k')$ and integrating over all space and repeating

the same process with $\mathbf{N}_{\substack{e\\o}\ell' m'}(k')$. Due to the orthogonality of vector spherical harmonics, we can solver for these unknown coefficients, yielding

$$\begin{aligned}\mathbf{A}_{\substack{e\\o}\ell m} =& \frac{k^2(2-\delta_{m0})(2\ell+1)(\ell-m)!}{2\pi^2\ell(\ell+1)(\ell+m)!}\mathbf{M}'_{\substack{e\\o}\ell m}(k)\\ \mathbf{B}_{\substack{e\\o}\ell m} =& \frac{k^2(2-\delta_{m0})(2\ell+1)(\ell-m)!}{2\pi^2\ell(\ell+1)(\ell+m)!}\mathbf{N}'_{\substack{e\\o}\ell m}(k)\end{aligned} \tag{A.14}$$

where the primed coordinates (r', θ', ϕ') are represented by the prime on $\mathbf{M}'_{\substack{e\\o}\ell m}(k)$ and $\mathbf{N}'_{\substack{e\\o}\ell m}(k)$. The form of these expansion coefficients can be inserted into the expression for the delta function

$$\begin{aligned}\delta(\mathbf{r}-\mathbf{r}')\mathbb{1} =& \frac{1}{2\pi^2}\int_0^\infty \mathrm{d}k\ k^2 \sum_{\ell=0}^{\infty}\sum_{m=0}^{\ell} \frac{(2-\delta_{m0})(2\ell+1)(\ell-m)!}{\ell(\ell+1)(\ell+m)!}\left[\mathbf{M}_{\substack{e\\o}\ell m}(k)\mathbf{M}'_{\substack{e\\o}\ell m}(k) + \mathbf{N}_{\substack{e\\o}\ell m}(k)\mathbf{N}'_{\substack{e\\o}\ell m}(k)\right]\\ =& \frac{1}{2\pi^2}\int_0^\infty \mathrm{d}k\ k^2 \sum_{\ell=0}^{\infty}\sum_{m=0}^{\ell} \lambda_{\ell m}\left[\mathbf{M}_{\substack{e\\o}\ell m}(k)\mathbf{M}'_{\substack{e\\o}\ell m}(k) + \mathbf{N}_{\substack{e\\o}\ell m}(k)\mathbf{N}'_{\substack{e\\o}\ell m}(k)\right]\end{aligned} \tag{A.15}$$

where the ℓm dependent coefficient is wrapped up into $\lambda_{\ell m}$. We can now use this form to solve for the free-space Green's function, $\overline{\mathbf{G}}_0(\mathbf{r}, \mathbf{r}', k)$

$$\begin{aligned}&\nabla\times(\nabla\times\overline{\mathbf{G}}_0(\mathbf{r},\mathbf{r}'))-\kappa^2\overline{\mathbf{G}}_0(\mathbf{r},\mathbf{r}')\\ &\qquad =\frac{1}{2\pi^2}\int_0^\infty \mathrm{d}k\ k^2 \sum_{\ell=0}^{\infty}\sum_{m=\ell}^{n} \lambda_{\ell m}\left[\mathbf{M}_{\substack{e\\o}\ell m}(k)\mathbf{M}'_{\substack{e\\o}\ell m}(k) + \mathbf{N}_{\substack{e\\o}\ell m}(k)\mathbf{N}'_{\substack{e\\o}\ell m}(k)\right]\end{aligned} \tag{A.16}$$

leading to the form

$$\overline{\mathbf{G}}_0(\mathbf{r},\mathbf{r}') = \frac{1}{2\pi^2}\int_0^\infty \mathrm{d}k\ \frac{k^2}{k^2-\kappa^2}\sum_{\ell=0}^{\infty}\sum_{m=0}^{\ell} \lambda_{\ell m}\left[\mathbf{M}_{\substack{e\\o}\ell m}(k)\mathbf{M}'_{\substack{e\\o}\ell m}(k) + \mathbf{N}_{\substack{e\\o}\ell m}(k)\mathbf{N}'_{\substack{e\\o}\ell m}(k)\right]. \tag{A.17}$$

Now let us consider the integral over k. The only dependence on k appears in the $z_\ell(kr)$ portion of the vector spherical harmonics, so the integral of interest is actually

$$\int_0^\infty \mathrm{d}\kappa \; \frac{\kappa^2}{\kappa^2 - k^2} j_\ell(\kappa r) j_\ell(\kappa r') = \frac{i\pi k}{2} \begin{cases} h_\ell^{(1)}(kr) j_\ell(kr') & r>r' \\ j_\ell(kr) h_\ell^{(1)}(kr') & r<r' \end{cases}. \tag{A.18}$$

We will use a new notation of $\mathbf{N}_{\substack{e \\ o}\ell m}(k)$ for basis functions that are dependent on j_ℓ and $\mathbf{N}^{(1)}_{\substack{e \\ o}\ell m}(k)$ for basis functions that are dependent on $h_\ell^{(1)}$. The free-space Green's function now holds that form

$$\overline{\mathbf{G}}_0(\mathbf{r},\mathbf{r}') = \frac{ik}{4\pi} \sum_{\ell=0}^{\infty} \sum_{m=0}^{\ell} \lambda_{\ell m} \begin{bmatrix} \mathbf{M}^{(1)}_{\substack{e \\ o}\ell m}(k) \mathbf{M}'_{\substack{e \\ o}\ell m}(k) + \mathbf{N}^{(1)}_{\substack{e \\ o}\ell m}(k) \mathbf{N}'_{\substack{e \\ o}\ell m}(k) & r>r' \\ \mathbf{M}_{\substack{e \\ o}\ell m}(k) \mathbf{M}'^{(1)}_{\substack{e \\ o}\ell m}(k) + \mathbf{N}_{\substack{e \\ o}\ell m}(k) \mathbf{N}'^{(1)}_{\substack{e \\ o}\ell m}(k) & r<r' \end{bmatrix}. \tag{A.19}$$

This free-space Green's function will be used for solving for the scattered/induced Green's function when a dielectric body is present. However, the location of the current distribution will have a significant effect on the form of the expansion coefficients of the scattered fields.

A.2.1 External Current Distribution

The first case we will consider is the case of external/aloof current distributions. In this scenario, the total Green's function will have the form

$$\begin{aligned} \overline{\mathbf{G}}_{\mathrm{ext}}(\mathbf{r},\mathbf{r}') =& \overline{\mathbf{G}}_0(\mathbf{r},\mathbf{r}') + \overline{\mathbf{G}}^{\mathrm{ind}}_{\mathrm{ext}}(\mathbf{r},\mathbf{r}') \quad r \geq a \;\; k = k_1 \\ \overline{\mathbf{G}}_{\mathrm{int}}(\mathbf{r},\mathbf{r}') =& \overline{\mathbf{G}}^{\mathrm{ind}}_{\mathrm{int}}(\mathbf{r},\mathbf{r}') \qquad\qquad\quad r \leq a \;\; k = k_2 \end{aligned} \tag{A.20}$$

where the radius of a sphere is represented by the variable a. We can then expand the scattered Green's functions in terms of the same spherical basis functions as before

$$\begin{aligned} \overline{\mathbf{G}}^{\mathrm{ind}}_{\mathrm{ext}}(\mathbf{r},\mathbf{r}') =& \frac{k_1}{4\pi} \sum_{\ell=0}^{\infty} \sum_{m=0}^{\ell} \lambda_{\ell m} \left[A_\ell \mathbf{M}^{(1)}_{\substack{e \\ o}\ell m}(k) \mathbf{M}'^{(1)}_{\substack{e \\ o}\ell m}(k) + B_\ell \mathbf{N}^{(1)}_{\substack{e \\ o}\ell m}(k) \mathbf{N}'^{(1)}_{\substack{e \\ o}\ell m}(k) \right]. \\ \overline{\mathbf{G}}^{\mathrm{ind}}_{\mathrm{int}}(\mathbf{r},\mathbf{r}') =& \frac{k_1}{4\pi} \sum_{\ell=0}^{\infty} \sum_{m=0}^{\ell} \lambda_{\ell m} \left[C_\ell \mathbf{M}_{\substack{e \\ o}\ell m}(k) \mathbf{M}'^{(1)}_{\substack{e \\ o}\ell m}(k) + D_\ell \mathbf{N}_{\substack{e \\ o}\ell m}(k) \mathbf{N}'^{(1)}_{\substack{e \\ o}\ell m}(k) \right]. \end{aligned} \tag{A.21}$$

with expansion coefficients (A,B,C,D) that will be determined by solving for the boundary conditions of the Green's function at the surface of the dielectric body

$$\begin{aligned} &1) \quad \hat{r} \times \overline{\mathbf{G}}_{\text{int}}(\mathbf{r}, \mathbf{r}') = \hat{r} \times \overline{\mathbf{G}}_{\text{ext}}(\mathbf{r}, \mathbf{r}') \\ &2) \quad \hat{r} \times (\nabla \times \overline{\mathbf{G}}_{\text{int}}(\mathbf{r}, \mathbf{r}')) = \hat{r} \times (\nabla \times \overline{\mathbf{G}}_{\text{ext}}(\mathbf{r}, \mathbf{r}')) \end{aligned} \tag{A.22}$$

which yields

$$\begin{aligned} A_\ell =& - i \frac{j_\ell(\rho_1)[\rho_2 j_\ell(\rho_2)]' - j_\ell(\rho_2)[\rho_1 j_\ell(\rho_1)]'}{h_\ell^{(1)}(\rho_1)[\rho_2 j_\ell(\rho_2)]' - j_\ell(\rho_2)[\rho_1 h_\ell^{(1)}(\rho_1)]'} \\ B_\ell =& - i \frac{N^2 j_\ell(\rho_2)[\rho_1 j_\ell(\rho_1)]' - j_\ell(\rho_1)[\rho_2 j_\ell(\rho_2)]'}{N^2 j_\ell(\rho_2)[\rho_1 h_\ell^{(1)}(\rho_1)]' - h_\ell^{(1)}(\rho_1)[\rho_2 j_\ell(\rho_2)]'} \\ C_\ell =& i \frac{j_\ell(\rho_1)[\rho_1 h_\ell^{(1)}(\rho_1)]' - h_\ell^{(1)}(\rho_1)[\rho_1 j_\ell(\rho_1)]'}{j_\ell(\rho_2)[\rho_1 h_\ell^{(1)}(\rho_1)]' - h_\ell^{(1)}(\rho_1)[\rho_2 j_\ell(\rho_2)]'} \\ D_\ell =& i \frac{N j_\ell(\rho_1)[\rho_1 h_\ell^{(1)}(\rho_1)]' - N h_\ell^{(1)}(\rho_1)[\rho_1 j_\ell(\rho_1)]'}{N^2 j_\ell(\rho_2)[\rho_1 h_\ell^{(1)}(\rho_1)]' - h_\ell^{(1)}(\rho_1)[\rho_2 j_\ell(\rho_2)]'} \end{aligned} \tag{A.23}$$

where $\rho_1 = k_1 a$, $\rho_2 = k_2 a$, N is the complex index of refraction, and the prime notation represents differentiation with respect to the argument of the spherical Bessel/Hankel function. These are the forms of the coefficients that will go into the EELS expression shown earlier.

A.2.2 Internal Current Distribution

The case of an internal beam trajectory is more complicated than that of the external beam position, as the Green's function needs to be consider for the case of the current lying both external and internal to the dielectric body, as the current must travel through space, enter and then exit the body.

$$\begin{aligned} \overline{\mathbf{G}}_{\text{ext}}(\mathbf{r}, \mathbf{r}') =& \overline{\mathbf{G}}_{\text{ext}}^{\text{ind,p}}(\mathbf{r}, \mathbf{r}') && r \geq a \quad k = k_1 \\ \overline{\mathbf{G}}_{\text{int}}(\mathbf{r}, \mathbf{r}') =& \overline{\mathbf{G}}_0(\mathbf{r}, \mathbf{r}') + \overline{\mathbf{G}}_{\text{int}}^{\text{ind,p}}(\mathbf{r}, \mathbf{r}') && r \leq a \quad k = k_2 \end{aligned} \tag{A.24}$$

where the radius of a sphere is represented by the variable a. We can then expand the scattered Green's functions in terms of the same spherical basis functions as before

$$\begin{aligned}
\overline{\mathbf{G}}_{\text{ext}}^{\text{ind,p}}(\mathbf{r},\mathbf{r}') =& \frac{k_2}{4\pi}\sum_{\ell=0}^{\infty}\sum_{m=0}^{\ell}\lambda_{\ell m}\left[E_\ell \mathbf{M}^{(1)}_{\substack{e\\o}\ell m}(k_1)\mathbf{M}'_{\substack{e\\o}\ell m}(k_2)+F_\ell \mathbf{N}^{(1)}_{\substack{e\\o}\ell m}(k_1)\mathbf{N}'_{\substack{e\\o}\ell m}(k_2)\right].\\
\overline{\mathbf{G}}_{\text{int}}^{\text{ind,p}}(\mathbf{r},\mathbf{r}') =& \frac{k_2}{4\pi}\sum_{\ell=0}^{\infty}\sum_{m=0}^{\ell}\lambda_{nm}\left[G_\ell \mathbf{M}_{\substack{e\\o}\ell m}(k_2)\mathbf{M}'_{\substack{e\\o}\ell m}(k_2)+H_\ell \mathbf{N}_{\substack{e\\o}\ell m}(k_2)\mathbf{N}'_{\substack{e\\o}\ell m}(k_2)\right].
\end{aligned} \tag{A.25}$$

with expansion coefficients (E,F,G,H) that will be determined by solving for the boundary conditions of the Green's function at the surface of the dielectric body

$$\begin{aligned}
&1)\quad \hat{r}\times\overline{\mathbf{G}}_{\text{int}}(\mathbf{r},\mathbf{r}') = \hat{r}\times\overline{\mathbf{G}}_{\text{ext}}(\mathbf{r},\mathbf{r}')\\
&2)\quad \hat{r}\times(\nabla\times\overline{\mathbf{G}}_{\text{int}}(\mathbf{r},\mathbf{r}')) = \hat{r}\times(\nabla\times\overline{\mathbf{G}}_{\text{ext}}(\mathbf{r},\mathbf{r}'))
\end{aligned} \tag{A.26}$$

which yields

$$\begin{aligned}
E_\ell =& i\frac{h_\ell^{(1)}(\rho_2)[\rho_2 j_\ell(\rho_2)]' - j_\ell(\rho_2)[\rho_2 h_\ell^{(1)}(\rho_2)]'}{h_\ell^{(1)}(\rho_1)[\rho_2 j_\ell(\rho_2)]' - j_\ell(\rho_2)[\rho_1 h_\ell^{(1)}(\rho_1)]'}\\
F_\ell =& -i\frac{N h_\ell^{(1)}(\rho_2)[\rho_2 j_\ell(\rho_2)]' - N j_\ell(\rho_2)[\rho_2 h_\ell^{(1)}(\rho_2)]'}{N^2 j_\ell(\rho_2)[\rho_1 h_\ell^{(1)}(\rho_1)]' - h_\ell^{(1)}(\rho_1)[\rho_2 j_\ell(\rho_2)]'}\\
G_\ell =& -i\frac{h_\ell^{(1)}(\rho_1)[\rho_2 h_\ell^{(1)}(\rho_2)]' - h_\ell^{(1)}(\rho_2)[\rho_1 h_\ell^{(1)}(\rho_1)]'}{h_\ell^{(1)}(\rho_1)[\rho_2 j_\ell(\rho_2)]' - j_\ell(\rho_2)[\rho_1 h_\ell^{(1)}(\rho_1)]'}\\
H_\ell =& i\frac{h_\ell^{(1)}(\rho_1)[\rho_2 h_\ell^{(1)}(\rho_2)]' - N^2 h_\ell^{(1)}(\rho_2)[\rho_1 h_\ell^{(1)}(\rho_1)]'}{N^2 j_\ell(\rho_2)[\rho_1 h_\ell^{(1)}(\rho_1)]' - h_\ell^{(1)}(\rho_1)[\rho_2 j_\ell(\rho_2)]'}.
\end{aligned} \tag{A.27}$$

Appendix B

DIELECTRIC FUNCTIONS

B.1 Dielectric Model of Metals

The discovery of the electron by J.J Thomson in 1897 required a reworking of the theory of matter. Only three years later in 1900 P. Drude applied the kinetic theory of gases to an electron gas within a metal as an attempt to describe electrical and thermal conduction. Drude treated electrons as spheres moving against a background of heavy fixed ions and undergoing straight-line, continuous, random motion. Some additional assumptions made by Drude were: 1) Electrons were non-interacting. 2) Scattering events are instantaneous, altering the electron velocities and mainly occurred with the nuclear background. Scattering events occur on average even τ seconds. 3) Collisions are the only method of heat transfer and obtaining thermal equilibrium. [8]

While these assumptions are not an accurate description of the physical process occurring in the metal, the model was successful at describing the behavior of metals and in particular noble metals. The Drude model when applied to obtain a dielectric function ultimately has the form

$$\epsilon(\omega) = \epsilon_\infty - \frac{\omega_p^2}{\omega^2 + i\gamma\omega}. \tag{B.1}$$

The parameters in this model are material dependence each holding physical significance. The contribution of high-frequency core excitations are contained in the variable ϵ_∞. The scattering frequency of conduction band electrons are represented by $\gamma = 1/\tau$. The plasma frequency, ω_p, is related to the electron density and effective mass in the conduction band. Combined, these terms form the Drude model, allowing for the treatment of bulk metals.

B.2 Dielectric Functions for Non-Metals

The Drude model for metals considered the dynamics of the conduction band electrons within the material and all transitions for core electrons were wrapped up in an empirical coefficient. Unfortunately non-metals do not have the same luxury of focusing on the behavior of the conduction band, as the conduction band is unoccupied for non-metals. Electrons in semi-conductors and insulators have less freedom in their motion and interaction with electromagnetic fields results in no electronic transition in the material until the electrons are capable of exciting to the conduction band of the material. This gap in the density of states leaves spectral regions in which the material lacks optical activity, and the dielectric function is real valued (non-absorbing). As the nature of the electronic states in non-metals can be rather complicated, these materials are treated with empirical dielectric functions in this dissertation.

BIBLIOGRAPHY

[1] Hiroyuki Abe, Hiroki Kurata, and Kiichi Hojou. Spatially resolved electron energy-loss spectroscopy of the surface excitations on the insulating fine particle of aluminum oxide. *Journal of the Physical Society of Japan*, 69(5):1553–1557, 2000.

[2] Arash Ahmadivand, Nezih Pala, and Durdu Ö Güney. Enhancement of photothermal heat generation by metallodielectric nanoplasmonic clusters. *Opt. Express*, 23(11):A682–A691, 2015.

[3] M Grant Albrecht and J Alan Creighton. Anomalously intense raman spectra of pyridine at a silver electrode. *J. Am. Chem. Soc.*, 99(15):5215–5217, 1977.

[4] Duncan T. L. Alexander, Peter A. Crozier, and James R. Anderson. Brown carbon spheres in east asian outflow and their optical properties. *Science*, 321(5890):833–836, 2008.

[5] A. Alù, A. Salandrino, and N. Engheta. Negative effective permeability and left-handed materials at optical frequencies. *Opt. Express*, 14(4):1557–1567, 2006.

[6] Andrea Alù and Nader Engheta. Dynamical theory of artificial optical magnetism produced by rings of plasmonic nanoparticles. *Phys. Rev. B*, 78:085112, 2008.

[7] Ilke Arslan, Jerome K Hyun, Rolf Erni, Michael N Fairchild, Stephen D Hersee, and David A Muller. Using electrons as a high-resolution probe of optical modes in individual nanowires. *Nano letters*, 9(12):4073–4077, 2009.

[8] Neil W. Ashcroft and David N. Mermin. *Solid State Physics*. Brooks Cole, 1976.

[9] M Ausloos, P Clippe, and AA Lucas. Infrared active modes in large clusters of spheres. *Phys. Rev. B*, 18(12):7176, 1978.

[10] Guillaume Baffou and Romain Quidant. Thermo-plasmonics: using metallic nanostructures as nano-sources of heat. *Laser & Photonics Reviews*, 7(2):171–187, 2013.

[11] Guillaume Baffou, Romain Quidant, and F Javier García de Abajo. Nanoscale control of optical heating in complex plasmonic systems. *ACS nano*, 4(2):709–716, 2010.

[12] Christopher L Baldwin, Nicholas W Bigelow, and David J Masiello. Thermal signatures of plasmonic fano interferences: Toward the achievement of nanolocalized temperature manipulation. *J. Phys. Chem. Lett.*, 5(8):1347–1354, 2014.

[13] Yanjun Bao, Zhijian Hu, Ziwei Li, Xing Zhu, and Zheyu Fang. Magnetic plasmonic fano resonance at optical frequency. *Small*, 11(18):2177–2181, 2015.

[14] William L Barnes, Alain Dereux, and Thomas W Ebbesen. Surface plasmon subwavelength optics. *Nature*, 424(6950):824–830, 2003.

[15] Steven J Barrow, Sean M Collins, David Rossouw, Alison M Funston, Gianluigi A Botton, Paul A Midgley, and Paul Mulvaney. Electron energy loss spectroscopy investigation into symmetry in gold trimer and tetramer plasmonic nanoparticle structures. *ACS nano*, 10(9):8552–8563, 2016.

[16] EPLJS Betzig, PL Finn, and JS Weiner. Combined shear force and near-field scanning optical microscopy. *Appl. Phys. Lett.*, 60(20):2484–2486, 1992.

[17] Nicholas W. Bigelow, Alex Vaschillo, Jon P. Camden, and David J. Masiello. Signatures of fano interferences in the electron energy loss spectroscopy and cathodoluminescence of symmetry-broken nanorod dimers. *ACS Nano*, 7(5):4511–4519, 2013.

[18] Nicholas W. Bigelow, Alex Vaschillo, Vighter Iberi, Jon P. Camden, and David J. Masiello. Characterization of the electron- and photon-driven plasmonic excitations of metal nanorods. *ACS Nano*, 6(8):7497–7504, 2012.

[19] Gail S Blaustein, Michael I Gozman, Olga Samoylova, I Ya Polishchuk, and Alexander L Burin. Guiding optical modes in chains of dielectric particles. *Optics Express*, 15(25):17380–17391, 2007.

[20] David Bohm and David Pines. A collective description of electron interactions. I. magnetic interactions. *Phys. Rev.*, 82:625–634, 1951.

[21] David Bohm and David Pines. A collective description of electron interactions: III. coulomb interactions in a degenerate electron gas. *Phys. Rev.*, 92:609–625, 1953.

[22] Craig F. Bohren and Donald R. Huffman. *Absorption and Scattering of Light by Small Particles*. John Wiley & Sons, 2008.

[23] Adela C Bonoiu, Supriya D Mahajan, Hong Ding, Indrajit Roy, Ken-Tye Yong, Rajiv Kumar, Rui Hu, Earl J Bergey, Stanley A Schwartz, and Paras N Prasad. Nanotechnology approach for drug addiction therapy: gene silencing using delivery of gold

nanorod-sirna nanoplex in dopaminergic neurons. *Proceedings of the National Academy of Sciences*, 106(14):5546–5550, 2009.

[24] WJ Bowman, K March, CA Hernandez, and PA Crozier. Measuring bandgap states in individual non-stoichiometric oxide nanoparticles using monochromated stem eels: The praseodymium–ceria case. *Ultramicroscopy*, 167:5–10, 2016.

[25] Daniel W Brandl, Nikolay A Mirin, and Peter Nordlander. Plasmon modes of nanosphere trimers and quadrumers. *J. Phys. Chem. B*, 110(25):12302–12310, 2006.

[26] Mark L Brongersma, Naomi J Halas, and Peter Nordlander. Plasmon-induced hot carrier science and technology. *Nature nanotechnology*, 10(1):25–34, 2015.

[27] Lisa V Brown, Heidar Sobhani, J Britt Lassiter, Peter Nordlander, and Naomi J Halas. Heterodimers: plasmonic properties of mismatched nanoparticle pairs. *ACS Nano*, 4(2):819–832, 2010.

[28] Wenshan Cai, Uday K Chettiar, Hsiao-Kuan Yuan, Vashista C de Silva, Alexander V Kildishev, Vladimir P Drachev, and Vladimir M Shalaev. Metamagnetics with rainbow colors. *Opt. Express*, 15(6):3333–3341, 2007.

[29] Charles Cherqui, Nicholas W Bigelow, Alex Vaschillo, Harrison Goldwyn, and David J Masiello. Combined tight-binding and numerical electrodynamics understanding of the stem/eels magneto-optical responses of aromatic plasmon-supporting metal oligomers. *ACS Photonics*, 1(10):1013–1024, 2014.

[30] Charles Cherqui, Niket Thakkar, Guoliang Li, Jon P. Camden, and David J. Masiello. Characterizing localized surface plasmons using electron energy-loss spectroscopy. *Annu. Rev. Phys. Chem.*, 67(1):331–357, 2016.

[31] Charles Cherqui, Yueying Wu, Guoliang Li, Steven C Quillin, Jacob A Busche, Niket Thakkar, Claire A West, Nicholas P Montoni, Philip D Rack, Jon P Camden, et al. Stem/eels imaging of magnetic hybridization in symmetric and symmetry-broken plasmon oligomer dimers and all-magnetic fano interference. *Nano letters*, 16(10):6668–6676, 2016.

[32] Sean M Collins, Olivia Nicoletti, David Rossouw, Tomas Ostasevicius, and Paul A Midgley. Excitation dependent fano-like interference effects in plasmonic silver nanorods. *Phys. Rev. B*, 90(15):155419, 2014.

[33] Philippe Colomban, Aurelie Tournie, and Paola Ricciardi. Raman spectroscopy of copper nanoparticle-containing glass matrices: Ancient red stained-glass windows. *Journal of Raman Spectroscopy*, 40(12):1949–1955, 2009.

[34] Peter A Crozier. Vibrational and valence aloof beam eels: A potential tool for nondestructive characterization of nanoparticle surfaces. *Ultramicroscopy*, 2017.

[35] Peter A Crozier, Toshihiro Aoki, and Qianlang Liu. Detection of water and its derivatives on individual nanoparticles using vibrational electron energy-loss spectroscopy. *Ultramicroscopy*, 169:30–36, 2016.

[36] Christian Czekalla, Thomas Nobis, Andreas Rahm, Bingqiang Cao, Jesús Zúñiga Pérez, Chris Sturm, Rüdiger Schmidt-Grund, Michael Lorenz, and Marius Grundmann. Whispering gallery modes in zinc oxide micro-and nanowires. *physica status solidi (b)*, 247(6):1282–1293, 2010.

[37] Ilivier Darrigol. *A History of Optics*. Oxford University Press, 2012.

[38] Howard DeVoe. Optical properties of molecular aggregates. i. classical model of electronic absorption and refraction. *The Journal of Chemical Physics*, 41(2):393–400, 1964.

[39] Bruce T Draine and Piotr J Flatau. Discrete-dipole approximation for scattering calculations. *JOSA A*, 11(4):1491–1499, 1994.

[40] Ray F Egerton. *Electron energy-loss spectroscopy in the electron microscope*. Springer Science & Business Media, 2011.

[41] Rolf Erni and Nigel D Browning. The impact of surface and retardation losses on valence electron energy-loss spectroscopy. *Ultramicroscopy*, 108(2):84–99, 2008.

[42] Jonathan A Fan, Chihhui Wu, Kui Bao, Jiming Bao, Rizia Bardhan, Naomi J Halas, Vinothan N Manoharan, Peter Nordlander, Gennady Shvets, and Federico Capasso. Self-assembled plasmonic nanoparticle clusters. *Science*, 328(5982):1135–1138, 2010.

[43] Ugo Fano. Effects of configuration interaction on intensities and phase shifts. *Physical Review*, 124(6):1866, 1961.

[44] Martin Fleischmann, Patrick J Hendra, and AJ McQuillan. Raman spectra of pyridine adsorbed at a silver electrode. *Chem. Phys. Lett.*, 26(2):163–166, 1974.

[45] R Fuchs. Theory of the optical properties of ionic crystal cubes. *Physical Review B*, 11(4):1732, 1975.

[46] F. J. García de Abajo. Optical excitations in electron microscopy. *Rev. Mod. Phys.*, 82(1):209, 2010.

[47] F.J. García de Abajo. Relativistic energy loss and induced photon emission in the interaction of a dielectric sphere with an external electron beam. *Physical Review B*, 59(4):3095, 1999.

[48] F.J. García de Abajo and A Howie. Retarded field calculation of electron energy loss in inhomogeneous dielectrics. *Physical Review B*, 65(11):115418, 2002.

[49] Vincenzo Giannini, Antonio I Fernández-Domínguez, Yannick Sonnefraud, Tyler Roschuk, Roberto Fernández-García, and Stefan A Maier. Controlling light localization and light–matter interactions with nanoplasmonics. *Small*, 6(22):2498–2507, 2010.

[50] Juan J Giner-Casares, Malou Henriksen-Lacey, Isabel García, and Luis M Liz-Marzán. Plasmonic surfaces for cell growth and retrieval triggered by near-infrared light. *Angewandte Chemie*, 128(3):986–990, 2016.

[51] VL Ginzburg. Radiation from uniformly moving sources (vavilov-cherenkov effect, transition radiation, and some other phenomena). *Acoustical Physics*, 51(1):11–23, 2005.

[52] Alexander O Govorov and Hugh H Richardson. Generating heat with metal nanoparticles. *Nano today*, 2(1):30–38, 2007.

[53] Beth S. Guiton, Vighter Iberi, Shuzhou Li, Donovan N. Leonard, Chad M. Parish, Paul G. Kotula, Maria Varela, George C. Schatz, Stephen J. Pennycook, and Jon P. Camden. Correlated optical measurements and plasmon mapping of silver nanorods. *Nano Letters*, 11(8):3482–3488, 2011.

[54] Feng Hao, Yannick Sonnefraud, Pol Van Dorpe, Stefan A. Maier, Naomi J. Halas, and Peter Nordlander. Symmetry breaking in plasmonic nanocavities: Subradiant lspr sensing and a tunable fano resonance. *Nano Letters*, 8(11):3983–3988, 2008.

[55] Achim Hartschuh. Tip-enhanced near-field optical microscopy. *Angew. Chem. Int. Edit.*, 47(43):8178–8191, 2008.

[56] Mario Hentschel, Daniel Dregely, Ralf Vogelgesang, Harald Giessen, and Na Liu. Plasmonic oligomers: The role of individual particles in collective behavior. *ACS Nano*, 5(3):2042–2050, 2011.

[57] Mario Hentschel, Michael Saliba, Ralf Vogelgesang, Harald Giessen, A Paul Alivisatos, and Na Liu. Transition from isolated to collective modes in plasmonic oligomers. *Nano Lett.*, 10(7):2721–2726, 2010.

[58] A Hessel and AA Oliner. A new theory of woodâĂŹs anomalies on optical gratings. *Applied Optics*, 4(10):1275–1297, 1965.

[59] Kevin D Heylman, Niket Thakkar, Erik H Horak, Steven C Quillin, Charles Cherqui, Kassandra A Knapper, David J Masiello, and Randall H Goldsmith. Optical microresonators as single-particle absorption spectrometers. *Nature Photonics*, 10(12):788–795, 2016.

[60] James Hillier and RF Baker. Microanalysis by means of electrons. *Journal of Applied Physics*, 15(9):663–675, 1944.

[61] Ulrich Hohenester and Andreas Trügler. Mnpbem–a matlab toolbox for the simulation of plasmonic nanoparticles. *Comput. Phys. Commun.*, 183(2):370–381, 2012.

[62] Ben Hopkins, Dmitry S Filonov, Stanislav B Glybovski, and Andrey E Miroshnichenko. Hybridization and the origin of fano resonances in symmetric nanoparticle trimers. *Phys. Rev. B*, 92(4):045433, 2015.

[63] Ben Hopkins, Dmitry S Filonov, Andrey E Miroshnichenko, Francesco Monticone, Andrea Alú, and Yuri S Kivshar. Interplay of magnetic responses in all-dielectric oligomers to realize magnetic fano resonances. *ACS Photonics*, 2(6):724–729, 2015.

[64] A Howie and RH Milne. Excitations at interfaces and small particles. *Ultramicroscopy*, 18(1-4):427–433, 1985.

[65] Xiaohua Huang, Prashant K Jain, Ivan H El-Sayed, and Mostafa A El-Sayed. Plasmonic photothermal therapy (pptt) using gold nanoparticles. *Lasers in medical science*, 23(3):217, 2008.

[66] J Hubbard. The dielectric theory of electronic interactions in solids. *Proceedings of the Physical Society. Section A*, 68(11):976, 1955.

[67] JK Hyun, M Couillard, P Rajendran, CM Liddell, and DA Muller. Measuring far-ultraviolet whispering gallery modes with high energy electrons. *Applied Physics Letters*, 93(24):243106, 2008.

[68] JK Hyun, MP Levendorf, M Blood-Forsythe, J Park, and DA Muller. Relativistic electron energy loss spectroscopy of solid and core-shell nanowires. *Physical Review B*, 81(16):165403, 2010.

[69] John D. Jackson. *Classical Electrodynamics*. Wiley New York, 1962.

[70] K Järrendahl and H Arwin. Multiple sample analysis of spectroscopic ellipsometry data of semi-transparent films. *Thin Solid Films*, 313:114–118, 1998.

[71] David L Jeanmaire and Richard P Van Duyne. Surface raman spectroelectrochemistry: Part i. heterocyclic, aromatic, and aliphatic amines adsorbed on the anodized silver electrode. *J. Electroanal. Chem.*, 84(1):1–20, 1977.

[72] AC Johnson, Charles M Marcus, MP Hanson, and AC Gossard. Coulomb-modified fano resonance in a one-lead quantum dot. *Physical Review Letters*, 93(10):106803, 2004.

[73] P. B. Johnson and R. W. Christy. Optical constants of the noble metals. *Phys. Rev. B*, 6:4370–4379, 1972.

[74] Sinan Karaveli and Rashid Zia. Strong enhancement of magnetic dipole emission in a multilevel electronic system. *Opt. Lett.*, 35(20):3318–3320, 2010.

[75] Sinan Karaveli and Rashid Zia. Spectral tuning by selective enhancement of electric and magnetic dipole emission. *Phys. Rev. Lett.*, 106(19):193004, 2011.

[76] Mark Kasperczyk, Steven Person, Duarte Ananias, Luis D Carlos, and Lukas Novotny. Excitation of magnetic dipole transitions at optical frequencies. *Phys. Rev. Lett.*, 114(16):163903, 2015.

[77] Paul Kent and Allan Chapman. *Robert Hooke and the English Renaissance*. Gracewing, 2005.

[78] Katrin Kneipp, Yang Wang, Harald Kneipp, Lev T Perelman, Irving Itzkan, Ramachandra R Dasari, and Michael S Feld. Single molecule detection using surface-enhanced raman scattering (sers). *Phys. Rev. Lett.*, 78(9):1667, 1997.

[79] Kensuke Kobayashi, Hisashi Aikawa, Akira Sano, Shingo Katsumoto, and Yasuhiro Iye. Fano resonance in a quantum wire with a side-coupled quantum dot. *Physical Review B*, 70(3):035319, 2004.

[80] U Kreibig and L Genzel. Optical absorption of small metallic particles. *Surf. Sci.*, 156:678–700, 1985.

[81] E. Kretschmann and H. Raether. Radiative decay of non radiative surface plasmons excited by light. *Zeitschrift für Naturforschung A*, 23:2135–2136, 1968.

[82] Ondrej L Krivanek, Tracy C Lovejoy, Niklas Dellby, Toshihiro Aoki, RW Carpenter, Peter Rez, Emmanuel Soignard, Jiangtao Zhu, Philip E Batson, Maureen J Lagos, et al. Vibrational spectroscopy in the electron microscope. *Nature*, 514(7521):209–212, 2014.

[83] Ondrej L Krivanek, Tracy C Lovejoy, Niklas Dellby, and RW Carpenter. Monochromated stem with a 30 mev-wide, atom-sized electron probe. *Microscopy*, 62(1):3–21, 2013.

[84] Uluç Kutluay, Gregory C. Kujoth, and Mustafa K. Başkaya. Operating microscopes: past, present, and future. *Neurosurgical Focus*, 27(3):E4, 2009.

[85] Maureen J Lagos, Andreas Trügler, Ulrich Hohenester, and Philip E Batson. Mapping vibrational surface and bulk modes in a single nanocube. *Nature*, 543(7646):529–532, 2017.

[86] M Landmann, E Rauls, and WG Schmidt. The electronic structure and optical response of rutile, anatase and brookite tio2. *Journal of physics: condensed matter*, 24(19):195503, 2012.

[87] W. Lang. Geschwindigkeitsverluste mittelschneller elektronen beim durchgang durch dünne metalfolien. *Optik*, 3(3):233–246, 1948.

[88] J Britt Lassiter, Heidar Sobhani, Mark W Knight, Witold S Mielczarek, Peter Nordlander, and Naomi J Halas. Designing and deconstructing the fano lineshape in plasmonic nanoclusters. *Nano Letters*, 12(2):1058–1062, 2012.

[89] Ho-Tong Lee and Andrew W Poon. Fano resonances in prism-coupled square micropillars. *Optics letters*, 29(1):5–7, 2004.

[90] MB Lee, QY Yang, and ST Ceyer. Dynamics of the activated dissociative chemisorption of ch4 and implication for the pressure gap in catalysis: a molecular beam–high resolution electron energy loss study. *J. Chem. Phys.*, 87(5):2724–2741, 1987.

[91] Guoliang Li, Charles Cherqui, Nicholas W. Bigelow, Gerd Duscher, Patrick J. Straney, Jill E. Millstone, David J. Masiello, and Jon P. Camden. Spatially mapping energy transfer from single plasmonic particles to semiconductor substrates via stem/eels. *Nano Lett.*, 15(5):3465–3471, 2015.

[92] Na Li, Andreas Tittl, Song Yue, Harald Giessen, Chen Song, Baoquan Ding, and Na Liu. Dna-assembled bimetallic plasmonic nanosensors. *Light Sci. Appl.*, 3(12):e226, 2014.

[93] David C. Lindberg. *Theories of Vision from Al-Kindi to Kepler*. University of Chicago Press, 1976.

[94] Suljo Linic, Phillip Christopher, and David B Ingram. Plasmonic-metal nanostructures for efficient conversion of solar to chemical energy. *Nat. Mater.*, 10(12):911–921, 2011.

[95] Stephen G. Lipson, Henry Lipson, and David S. Tannhauser. *Optical Physics*. Cambridge University Press, 1998.

[96] H Liu, DA Genov, DM Wu, YM Liu, ZW Liu, C Sun, SN Zhu, and X Zhang. Magnetic plasmon hybridization and optical activity at optical frequencies in metallic nanostructures. *Phys. Rev. B*, 76(7):073101, 2007.

[97] H Liu, DA Genov, DM Wu, YM Liu, JM Steele, C Sun, SN Zhu, and X Zhang. Magnetic plasmon propagation along a chain of connected subwavelength resonators at infrared frequencies. *Phys. Rev. Lett.*, 97(24):243902, 2006.

[98] Na Liu, Lutz Langguth, Thomas Weiss, Jürgen Kästel, Michael Fleischhauer, Tilman Pfau, and Harald Giessen. Plasmonic analogue of electromagnetically induced transparency at the drude damping limit. *Nature Materials*, 8(9):758–762, 2009.

[99] Na Liu, Shaunak Mukherjee, Kui Bao, Lisa V Brown, Jens Dorfmüller, Peter Nordlander, and Naomi J Halas. Magnetic plasmon formation and propagation in artificial aromatic molecules. *Nano Lett.*, 12(1):364–369, 2011.

[100] Na Liu, Shaunak Mukherjee, Kui Bao, Yang Li, Lisa V Brown, Peter Nordlander, and Naomi J Halas. Manipulating magnetic plasmon propagation in metallic nanocluster networks. *ACS Nano*, 6(6):5482–5488, 2012.

[101] Qianlang Liu, Katia March, and Peter A Crozier. Nanoscale probing of bandgap states on oxide particles using electron energy-loss spectroscopy. *Ultramicroscopy*, 178:2–11, 2017.

[102] Boris Luk'yanchuk, Nikolay I Zheludev, Stefan A Maier, Naomi J Halas, Peter Nordlander, Harald Giessen, and Chong Tow Chong. The fano resonance in plasmonic nanostructures and metamaterials. *Nature Materials*, 9(9):707–715, 2010.

[103] Arka Majumdar, Armand Rundquist, Michal Bajcsy, Vaishno D Dasika, Seth R Bank, and Jelena Vučković. Design and analysis of photonic crystal coupled cavity arrays for quantum simulation. *Physical Review B*, 86(19):195312, 2012.

[104] Arka Majumdar, Armand Rundquist, Michal Bajcsy, and Jelena Vučković. Cavity quantum electrodynamics with a single quantum dot coupled to a photonic molecule. *Physical Review B*, 86(4):045315, 2012.

[105] R Miller, TE Northup, KM Birnbaum, ADBA Boca, AD Boozer, and HJ Kimble. Trapped atoms in cavity qed: coupling quantized light and matter. *Journal of Physics B: Atomic, Molecular and Optical Physics*, 38(9):S551, 2005.

[106] Nikolay A Mirin, Kui Bao, and Peter Nordlander. Fano resonances in plasmonic nanoparticle aggregates. *The Journal of Physical Chemistry A*, 113(16):4028–4034, 2009.

[107] Andrey E Miroshnichenko, Sergej Flach, Andrey V Gorbach, Boris S Luk'yanchuk, Yuri S Kivshar, and Michael I Tribelsky. Fano resonances: A discovery that was not made 100 years ago. *Optics and Photonics News*, 19(12):48–48, 2008.

[108] Shaunak Mukherjee, Florian Libisch, Nicolas Large, Oara Neumann, Lisa V Brown, Jin Cheng, J Britt Lassiter, Emily A Carter, Peter Nordlander, and Naomi J Halas. Hot electrons do the impossible: Plasmon-induced dissociation of h2 on au. *Nano Lett.*, 13(1):240–247, 2012.

[109] Douglas B. Murphy and Michael W. Davidson. *Fundamentals of Light Microscopy and Electronic Imaging*. Oxford: Wiley-Blackwell, 2011.

[110] Olivia Nicoletti, Martijn Wubs, N. Asger Mortensen, Wilfried Sigle, Peter A. van Aken, and Paul A. Midgley. Surface plasmon modes of a single silver nanorod: an electron energy loss study. *Opt. Express*, 19(16):15371–15379, 2011.

[111] Shuming Nie and Steven R Emory. Probing single molecules and single nanoparticles by surface-enhanced raman scattering. *Science*, 275(5303):1102–1106, 1997.

[112] Suzushi Nishimura, Neal Abrams, Bradley A Lewis, Lara I Halaoui, Thomas E Mallouk, Kurt D Benkstein, Jao van de Lagemaat, and Arthur J Frank. Standing wave enhancement of red absorbance and photocurrent in dye-sensitized titanium dioxide photoelectrodes coupled to photonic crystals. *Journal of the American Chemical Society*, 125(20):6306–6310, 2003.

[113] Thomas Nobis, Evgeni M Kaidashev, Andreas Rahm, Michael Lorenz, and Marius Grundmann. Whispering gallery modes in nanosized dielectric resonators with hexagonal cross section. *Physical review letters*, 93(10):103903, 2004.

[114] N Noginova, G Zhu, M Mavy, and MA Noginov. Magnetic dipole based systems for probing optical magnetism. *J. Appl. Phys.*, 103(7):07E901, 2008.

[115] Peter Nordlander. Plasmonics: the dark side of the ring. *Nat. Nanotechnol.*, 8(2):76–77, 2013.

[116] Andreas Otto. Excitation of nonradiative surface plasma waves in silver by the method of frustrated total reflection. *Zeitschrift für Physik A Hadrons and nuclei*, 216(4):398–410, 1968.

[117] Rupert F Oulton, Volker J Sorger, DA Genov, DFP Pile, and X Zhang. A hybrid plasmonic waveguide for subwavelength confinement and long-range propagation. *Nature Photonics*, 2(8):496–500, 2008.

[118] Taejong Paik, Benjamin T Diroll, Cherie R Kagan, and Christopher B Murray. Binary and ternary superlattices self-assembled from colloidal nanodisks and nanorods. *J. Am. Chem. So.*, 137(20):6662–6669, 2015.

[119] S. Panaro, F. De Angelis, and A. Toma. Dark and bright mode hybridization: From electric to magnetic fano resonances. *Opt. Lasers Eng.*, 76:64 – 69, 2016.

[120] David Pines and David Bohm. A collective description of electron interactions: II. collective vs individual particle aspects of the interactions. *Phys. Rev.*, 85:338–353, 1952.

[121] R Pogorzelski and C Yeh. Diffraction radiation from a charged particle moving through a penetrable sphere. *Physical Review A*, 8(1):137, 1973.

[122] Alexander Petrovich Potylitsyn. Transition radiation and diffraction radiation. similarities and differences. *Nuclear Instruments and Methods in Physics Research Section B: Beam Interactions with Materials and Atoms*, 145(1):169–179, 1998.

[123] C. J. Powell and J. B. Swan. Origin of the characteristic electron energy losses in aluminum. *Phys. Rev.*, 115:869–875, 1959.

[124] Edward M Purcell and Carlton R Pennypacker. Scattering and absorption of light by nonspherical dielectric grains. *The Astrophysical Journal*, 186:705–714, 1973.

[125] Zhaoxia Qian, Simon P Hastings, Chen Li, Brian Edward, Christine K McGinn, Nader Engheta, Zahra Fakhraai, and So-Jung Park. Raspberry-like metamolecules exhibiting strong magnetic resonances. *ACS Nano*, 9(2):1263–1270, 2015.

[126] Steven C Quillin, Charles Cherqui, Nicholas P Montoni, Guoliang Li, Jon P Camden, and David J Masiello. Imaging plasmon hybridization in metal nanoparticle aggregates with electron energy-loss spectroscopy. *The Journal of Physical Chemistry C*, 120(37):20852–20859, 2016.

[127] Roshdi Rashed. A pioneer in anaclastics: Ibn sahl on burning mirrors and lenses. *Isis*, 81(3):464–491, 1990.

[128] Gunter Reiss, Andreas Hutten, and Klaus D. Sattler. *Handbook of Nanophysics: Nanoparticles and Quantum Dots*. CRC Press, 2010.

[129] RH Ritchie. Plasma losses by fast electrons in thin films. *Physical Review*, 106(5):874, 1957.

[130] DM Roessler and WC Walker. Electronic spectrum and ultraviolet optical properties of crystalline mgo. *Physical Review*, 159(3):733, 1967.

[131] Eva-Maria Roller, Larousse Khosravi Khorashad, Michael Fedoruk, Robert Schreiber, Alexander O Govorov, and Tim Liedl. Dna-assembled nanoparticle rings exhibit electric and magnetic resonances at visible frequencies. *Nano Lett.*, 15(2):1368–1373, 2015.

[132] Ernst Ruska. *The Early Development of Electron Lenses and Electron Microscopy*. S. Hirzel Verlag, 1980.

[133] Gerhard Ruthemann. Diskrete energieverluste mittelschneller elektronen beim durchgang durch dünne folien. *Annalen der Physik*, 437(3-4):113–134, 1948.

[134] Miguel A Santiago-Cordoba, Svetlana V Boriskina, Frank Vollmer, and Melik C Demirel. Nanoparticle-based protein detection by optical shift of a resonant microcavity. *Applied Physics Letters*, 99(7):073701, 2011.

[135] Michaël Sarrazin, Jean-Pol Vigneron, and Jean-Marie Vigoureux. Role of wood anomalies in optical properties of thin metallic films with a bidimensional array of subwavelength holes. *Physical Review B*, 67(8):085415, 2003.

[136] Jonathan A Scholl, Aitzol Garcia-Etxarri, Garikoitz Aguirregabiria, Ruben Esteban, Tarun C Narayan, Ai Leen Koh, Javier Aizpurua, and Jennifer A Dionne. Evolution of plasmonic metamolecule modes in the quantum tunneling regime. *ACS Nano*, 2015.

[137] Julian Schwinger, Lester L. DeRaad, Kimball A. Milton, and Wu-yang Tsai. *Classical Electrodynamics*. Westview Press, 1998.

[138] Farbod Shafiei, Francesco Monticone, Khai Q Le, Xing-Xiang Liu, Thomas Hartsfield, Andrea Alù, and Xiaoqin Li. A subwavelength plasmonic metamolecule exhibiting magnetic-based optical fano resonance. *Nat. Nanotechnol.*, 8(2):95–99, 2013.

[139] Vladimir M Shalaev. Optical negative-index metamaterials. *Nat. Photonics*, 1(1):41–48, 2007.

[140] Sassan N Sheikholeslami, Aitzol García-Etxarri, and Jennifer A Dionne. Controlling the interplay of electric and magnetic modes via fano-like plasmon resonances. *Nano Lett.*, 11(9):3927–3934, 2011.

[141] Matthew T Sheldon, Jorik Van de Groep, Ana M Brown, Albert Polman, and Harry A Atwater. Plasmoelectric potentials in metal nanostructures. *Science*, 346(6211):828–831, 2014.

[142] Michael Stöger-Pollach. Optical properties and bandgaps from low loss eels: Pitfalls and solutions. *Micron*, 39(8):1092–1110, 2008.

[143] Michael Stöger-Pollach, H Franco, Peter Schattschneider, S Lazar, B Schaffer, W Grogger, and HW Zandbergen. Čerenkov losses: A limit for bandgap determination and kramers–kronig analysis. *Micron*, 37(5):396–402, 2006.

[144] Liuyang Sun, Tzuhsuan Ma, Seung-Cheol Yang, Dong-Kwan Kim, Gaehang Lee, Jinwei Shi, Irving Martinez, Gi-Ra Yi, Gennady Shvets, and Xiaoqin Li. The interplay between optical bianisotropy and magnetism in plasmonic metamolecules. *Nano Lett.*, 16(7):4322–4328, 2016.

[145] Chen-to Tai. *Dyadic Green Functions in Electromagnetic Theory*. The Book Service Ltd, 1972.

[146] Shu Fen Tan, Lin Wu, Joel KW Yang, Ping Bai, Michel Bosman, and Christian A Nijhuis. Quantum plasmon resonances controlled by molecular tunnel junctions. *Science*, 343(6178):1496–1499, 2014.

[147] Niket Thakkar, Charles Cherqui, and David J Masiello. Quantum beats from entangled localized surface plasmons. *ACS Photonics*, 2(1):157–164, 2015.

[148] Niket H Thakkar, Morgan T Rea, Kevin C Smith, Kevin D Heylman, Steven C Quillin, Kassandra Ann Knapper, Erik H Horak, David Masiello, and Randall H Goldsmith. Sculpting fano resonances to control photonic-plasmonic hybridization. *Nano Letters*, 2017.

[149] Michael I Tribelsky, Sergej Flach, Andrey E Miroshnichenko, Andrey V Gorbach, and Yuri S Kivshar. Light scattering by a finite obstacle and fano resonances. *Physical Review Letters*, 100(4):043903, 2008.

[150] Kerry J Vahala. Optical microcavities. *Nature*, 424(6950):839–846, 2003.

[151] Andrea Vallecchi, Matteo Albani, and Filippo Capolino. Collective electric and magnetic plasmonic resonances in spherical nanoclusters. *Opt. Express*, 19(3):2754–2772, 2011.

[152] K Van Benthem, C Elsässer, and RH French. Bulk electronic structure of srtio 3: experiment and theory. *Journal of Applied Physics*, 90(12):6156–6164, 2001.

[153] Fea Vollmer, D Braun, A Libchaber, M Khoshsima, I Teraoka, and S Arnold. Protein detection by optical shift of a resonant microcavity. *Applied Physics Letters*, 80(21):4057–4059, 2002.

[154] Bo Wang and Yan Zhang. Enhancement of optical magnetic modes by controlling the handedness of symmetry breaking in fano metamolecules. *IEEE J. Quantum Elect.*, 51(6):1–8, 2015.

[155] ZL Wang. Valence electron excitations and plasmon oscillations in thin films, surfaces, interfaces and small particles. *Micron*, 27(3-4):265–299, 1996.

[156] Zhijie Yang, Yanzhao Yang, Hui Liang, and Ling Liu. Hydrothermal synthesis of monodisperse ceo 2 nanocubes. *Materials Letters*, 63(21):1774–1777, 2009.

[157] Zhiqiang Yang, Kebin Zhou, Xiangwen Liu, Qun Tian, Deyi Lu, and Sen Yang. Single-crystalline ceria nanocubes: size-controlled synthesis, characterization and redox property. *Nanotechnology*, 18(18):185606, 2007.

[158] Takashi Yatsui, Toshiki Tsuboi, Maiku Yamaguchi, Katsuyuki Nobusada, Satoshi Tojo, Fabrice Stehlin, Olivier Soppera, and Daniel Bloch. Optically controlled magnetic-field etching on the nano-scale. *Light Sci. Appl.*, 5(3):e16054, 2016.

[159] Aycan Yurtsever, Martin Couillard, and David A Muller. Formation of guided cherenkov radiation in silicon-based nanocomposites. *Physical review letters*, 100(21):217402, 2008.

[160] Jiangtao Zhu, Peter A Crozier, Peter Ercius, and James R Anderson. Derivation of optical properties of carbonaceous aerosols by monochromated electron energy-loss spectroscopy. *Microscopy and Microanalysis*, 20(3):748–759, 2014.

[161] Max S Zolotorev and Kirk T McDonald. Classical radiation processes in the weizsacker-williams approximation. *arXiv preprint physics/0003096*, 2000.